Design Algorithms for Parallel Transmission in Magnetic Resonance Imaging

by

Kawin Setsompop

M.Eng, Engineering Science

Oxford University, 2003

Submitted to the Department of Electrical Engineering and Computer Science

in Partial Fulfillment of the Requirements for the Degree of

Doctor of Philosophy

at the Massachusetts Institute of Technology

June 2008

Author . . . . . .

Department of Electrical Engineering and Computer Science

May 2, 2008

Certified by. . . . . .

Elfar Adalsteinsson

Robert J. Shillman Assistant Professor of Electrical Engineering and Computer Science; Harvard-MIT Division of Health Science and Technology

Thesis Supervisor

Accepted by . . . . . .

Terry P. Orlando

Chairman, Department Committee on Graduate Students

Design Algorithms for Parallel Transmission in Magnetic Resonance Imaging

by

Kawin Setsompop

Submitted to the Department of Electrical Engineering
and Computer Science
on May 2, 2008, in Partial Fulfillment of the
Requirements for the Degree of
Doctor of Philosophy

Abstract

The focus of this dissertation is on the algorithm design, implementation, and validation of parallel transmission technology in Magnetic Resonance Imaging (MRI). Novel algorithms are proposed which yield excellent excitation control, low RF power requirements, methods that extend to non-linear large-flip-angle excitation, as well as a new algorithm for simultaneous spectral and spatial excitation critical to quantification of low-SNR brain metabolites in MR spectroscopic imaging. For testing and validation, these methods were implemented on a newly developed parallel transmission platform on both 3 T and 7 T MRI scanners to demonstrate the ability of these methods for high-fidelity B_1^+ mitigation, first by excitation of phantoms and then by human imaging. Further, spatially tailored RF pulses were demonstrated beyond conventional slice- or slab-selective excitation.

Thesis Supervisor: Elfar Adalsteinsson
Title: Robert J. Shillman Assistant Professor of Electrical Engineering and Computer Science; Harvard-MIT Division of Health Science and Technology

Acknowledgements

This work would have not been possible without the help and support of many individuals.

First, most importantly, I would like to thank my advisor, Prof. Elfar Adalsteinsson, who has been instrumental to this work. It has been a pleasure working with him. I am grateful for his inputs, enthusiasm, support, and guidance. I have learned so much from our discussions, not just on MRI, but on the general approach towards ones work.

I am fortunate to have the opportunity to work with Prof. Larry Wald. He has helped me tremendously. I thank him for his input and his reasoned advice which has significantly improved the work in this thesis.

I thank Prof. Dennis Freeman, who kindly gave his time to serve on my thesis committee.

I am grateful to my main collaborator and friend, Vijay Alagappan, who has played an integral role in the research effort of this thesis. He built all the RF coil array hardware used in this work and has helped with the setup of all the experiments. There were countless weekends that we have shared together at the scanner, willing or not, tinkering with equipments, trying to make things work. Thanks for your patience and for putting up with me.

It has been a pleasure interacting and working with the students in the Magnetic Resonance Imaging Group. In particular, I would like to thank Borjan Gagoski, who has been there with me from the start. I thank him for his friendship, help, and technical collaboration. I would also like to thank Div Bolar, Padraig Cantillon-Murphy, Joonsung Lee, Trina Kok, and Adam Zelinski.

I would like to express my appreciation to Arlene Wint who has made things run very smoothly for me and for the people in the lab.

I appreciate the help given to me by the students, and staff in the HST A. A. Martinos Center for Biomedical Imaging at MGH. In particular, I would like to thank Thomas Witzel, Dr. Jonathan Polimeni, and Dr. Graham Wiggins.

Siemens Medical Solution has provided both equipment and support that was essential for all the experiments in this thesis. The effort of Dr. Franz Schmitt, Ulrich

Fontius, Dr. Franz Hebrank, Dr. Andreas Potthast, and Dr. Juergen Nistler are especially appreciated.

I would like to acknowledge the financial support provided by the National Institutes of Health, NIBIB grants R01EB006847, R01EB007942, R01EB000790, and NCRR grant P41RR14075, Siemens Medical Solutions, R.J. Shillman Career Development Award, and the MIND Institute.

I wish to express my deepest appreciation for Chanikarn Wongviriyawong who has been such an integral part of my MIT experience. I thank her for her love, cheerful support, and encouragement that have kept me going for the last three years. I could not have found a truer companion through it all.

Finally, I would like to thank my parents, Wirote and Wandee, for their unconditional love and support. Without whom none of this would have been possible.

Massachusetts Institute of Technology Kawin Setsompop

April 25, 2008

Contents

Acknowledgements 5
Contents 7
List of Figures 9
Introduction 15
Chapter 1 Background: RF Excitation in MRI 21
1.1 Magnetic Resonance Imaging 21
1.2. RF Excitation Pulse Design 24
1.2.1 Single Channel transmission Theory 25
1.2.2 Parallel Transmission Theory 30
1.3 Imaging Schemes for Contrast Generation 41
Chapter 2 Parallel RF Transmission at 3 Tesla 49
2.1 Phantom experiments 49
2.1.1 Introduction 49
2.1.2 Methods 50
2.1.3 Results 57
2.1.4 Discussion 63
2.1.5 Conclusion 64
2.2 In Vivo Experiments 66
2.2.1 Introduction 66
2.2.2 Theory & Method 66
2.2.3 Results 68
2.2.4 Discussion and Conclusion 70
Chapter 3 Rapid Quantitative B1 mapping 71
3.1 Introduction 71
3.2 Theory 72
3.2.1 Saturated Double-Angle method 72
3.2.2 Rapid Quantitative B_1^+ Mapping via Receive profile estimation 76
3.2.3 Experimental B_1^+ mapping 80
Chapter 4 Magnitude Least Square Optimization 83
4.1 Introduction 83
4.2 Theory 84
4.3 Methods 87

4.4 Results 91
4.5 Discussion 98
Chapter 5 In-vivo Parallel Excitation at 7 Tesla 101
5.1 Introduction 101
5.2 Methods 101
5.3 Results 107
5.4 Discussion 118
5.5 Conclusion 119
Chapter 6 Spectral-Spatial Parallel Excitation 121
6.1 Introduction 121
6.2 Theory 122
6.3 Method 123
6.4 Results 126
6.5 Discussion and Conclusions 132
Chapter 7 High-Flip-Angle Parallel Excitation 135
7.1 Introduction 135
7.2 Theory 136
7.3 Methods 142
7.4 Results 144
7.5 Discussion and Conclusions 148
Chapter 8 Summary and Recommendations 149
8.1 Summary 149
8.2 Recommendations 151
Bibliography 153

List of Figures

FIGURE1: RF EXCITATION AND SIGNAL GENERATION 23
FIGURE 2: EMPLOYING GRADIENT FIELD FOR SIGNAL ACQUISITION 24
FIGURE 3: SLICE-SELECTIVE EXCITATION; LEFT: TARGET EXCITATION AND ITS FOURIER TRANSFORM, RIGHT: CORRESPONDING GRADIENT AND RF PULSES. 27
FIGURE 4: MIT LOGO TARGET EXCITATION PROFILE AND ITS TRANSFORM 28
FIGURE 5: 2D EXCITATION DESIGN; TOP: TARGET'S FOURIER TRANSFORM AND SPIRAL K-SPACE TRAJECTORY, BOTTOM: CORRESPONDING RF AND GRADIENT PULSES, AND THE RESULTING EXCITATION PROFILE. ... 28
FIGURE 6: SPOKES (LEFT) AND STACK OF SPIRAL (RIGHT) TRAJECTORIES. 29
FIGURE 7: CYLINDRICAL TARGET EXCITATION AND THE RESULTS OF SINGLE-CHANNEL ECHO PLANER EXCITATION WITH 2X ACCELERATION LEADING TO ALIASING/WRAP-AROUND EFFECT 32
FIGURE 8: CYLINDRICAL EXCITATION (2X) VIA PARALLEL TRANSMISSION OF TWO ORTHOGONAL RF COILS RESULTING IN NO ALIASING/WRAP-AROUND EFFECT 33
FIGURE 9: RF COIL ARRAYS EMPLOYED IN THIS WORK: (A) EIGHT-CHANNEL LOOP COIL ARRAY AT 3T, (B) EIGHT-CHANNEL STRIPLINE ARRAY AT 7T, (C) SIXTEEN-CHANNEL STRIPLINE ARRAY AT 7T..... 35
FIGURE 10: DIAGRAM OF THE BUTLER MATRIX WITH N/2 INPUTS FROM THE RF AMPLIFIERS AND N OUTPUTS TO THE TRANSMISSION COIL ELEMENTS. THE POWER TRANSMITTED BY THE K^{TH} AMPLIFIER IS SPLIT INTO EQUAL PARTS AND FEED TO THE OUTPUT WITH APPROPRIATE PHASE SHIFTS TO GENERATE THE K^{TH} BIRDCAGE MODE. 37
FIGURE 11: SLICE-SELECTIVE B1+ MITIGATED EXCITATION VIA SINGLE CHANNEL RF, **A)** STANDARD SLICE-SELECTIVE SINC EXCITATION WITH NO IN-PLANE MODULATION, RESULTING IN LARGE VARIATION IN THE EXCITED PROFILE. B) SPOKE EXCITATION WITH SUFFICIENT IN-PLANE MODULATION TO CORRECT FOR SEVERE B1+ INHOMOGENEITY. 39
FIGURE 12: ACCELERATION OF SPOKE TRAJECTORY VIA PARALLEL EXCITATION RESULTING IN A SIGNIFICANTLY REDUCTION IN THE NUMBER OF REQUIRED SPOKES, AND HENCE EXCITATION DURATION. 41
FIGURE 13: (A) BASIC SATURATION-RECOVERY SEQUENCE: A STRING OF 90° EXCITATION PULSES SEPARATED BY REPETITION TIME TR, ALONG WITH DATA ACQUISITION (REPRESENTED BY THE BLACK BLOCKS) AFTER EACH EXCITATION AT THE GRADIENT ECHO TIME TE. (B) TIME COURSE OF MZ: VALUE OF MZ PRIOR TO THE 90° PULSE DETERMINES THE RESULTANT SIGNAL GENERATED. FIGURE ADAPTED FROM (18). 42
FIGURE 14: SPIN ECHO GENERATION: AFTER THE 90° EXCITATION (A)-(B), DUE TO LOCAL FIELD VARIATION THE TRANSVERSE MAGNETIZATION OF THE DIPOLE MOMENTS ROTATE AT SLIGHTLY DIFFERENT FREQUENCY RESULTING IN PHASE DISPERSION (C). THE PHASE DISPERSION IS NEGATED WITH A 180° PULSE APPLIED ALONG THE X-AXIS (D), CAUSING THE DIPOLE MOMENTS TO REPHRASE AFTER TIME τ . FIGURE ADAPTED FROM (18)..... 45
FIGURE 15: SATURATION-RECOVERY SEQUENCE WITH SPIN ECHOES. FIGURE ADAPTED FROM (18). 45
FIGURE 16: A) SIEMENS 3T PARALLEL TRANSMISSION SCANNER. B) EIGHT-CHANNEL COIL ARRAY. EACH COIL HAS 17 CM DIAMETER, AND PLACED IN AN OVERLAPPING PATTERN ON AN ACRYLIC CYLINDER WITH A 28 CM DIAMETER. CENTERED IN THE COIL IS A 17-CM DIAMETER OIL-FILLED SPHERICAL PHANTOM THAT WAS USED FOR EVALUATION OF THE PARALLEL RF EXCITATION DESIGNS. 51
FIGURE 17: DURATION OF RF PULSE DESIGN FOR THE HIGH-RESOLUTION IN-PLANE EXCITATION DESIGN AS A FUNCTION OF ACCELERATION FACTOR. 52
FIGURE 18: K-SPACE TRAJECTORY FOR THE 4 SPOKES DESIGN (LEFT) AND FOR THE 7 SPOKES DESIGN (RIGHT) 53

FIGURE 19: MAGNITUDE (TOP) AND PHASE (BOTTOM) OF THE COIL PROFILES. COIL 1 IS ON THE LEFT, COIL 2 IS AT 45° CLOCKWISE TO COIL 1, AND SO ON FOR EACH OF THE 8 COILS..... 57
FIGURE 20: A) MAGNITUDE OF 2D EXCITATION WITH 1X THROUGH 8X ACCELERATION. EXPERIMENTAL DATA ARE SHOWN ON THE LEFT, AND SIMULATIONS ON THE RIGHT BASED ON THE MEASURED B_1^+ MAPS. B) PLOT OF CORRELATION COEFFICIENTS AMONG ACQUIRED, SIMULATION, AND TARGET PROFILE AS A FUNCTION OF ACCELERATION FACTOR FOR THE 2D EXCITATION. 58
FIGURE 21: PHASE OF 2D EXCITATION DESIGN FOR 4X ACCELERATION, ACQUIRED DATA ON THE LEFT, SIMULATION ON THE RIGHT. 59
FIGURE 22: EXPERIMENTAL RESULTS, FOR THE 2D EXCITATION AT 4X ACCELERATION WITH MISSING CHANNEL(S) ARE SHOWN ON THE LEFT. EVEN WITH ONE CHANNEL MISSING SEVERE ARTIFACTS ARE APPARENT. ALSO DEPICT ARE THE SIMULATION OF THE PROFILES THAT WOULD HAVE BEEN CREATED BY EACH COIL IN THIS EXPERIMENT. 60
FIGURE 23: INCREASED EXCITATION VOLTAGE FOR A 4X ACCELERATION DESIGN WITH 2D EXCITATION DEMONSTRATES THE INCREASED SNR WITH HIGHER VOLTAGE, BUT AT THE SAME TIME, INCREASED THE CANCELLATION ARTIFACTS IN THE BACKGROUND OF THE SPHERICAL PHANTOM DUE TO VIOLATION OF THE SMALL TIP ANGLE APPROXIMATION..... 60
FIGURE 24: SHOWS THE RESULTS AND SIMULATION DATA FOR THE 4 SPOKES (LEFT) AND THE 7 SPOKES (RIGHT) DESIGNS. IN EACH OF THE TWO SUB-FIGURES, THE TOP LEFT AND RIGHT ARE THE IN-PLANE AND SLICE SELECTION PROFILES OF RESULTS. THE BOTTOM LEFT IS THE Y-SLICES IN-PLANE PROFILES OF RESULT, AND THE BOTTOM RIGHT IS IN-PLANE DATA FROM THE SIMULATION. 62
FIGURE 25: SIMULATION OF STANDARD SLICE-SELECTIVE (TOP) AND RF SHIMMING (BOTTOM) EXCITATIONS. IN EACH OF THE TWO SUBFIGURES THE LEFT PANEL DISPLAYS THE OVERALL IN-PLANE PROFILE, AND THE RIGHT PANEL SHOWS A SERIES OF IN-PLANE PROFILES. 62
FIGURE 26: B1+ MAP ESTIMATION: 3-RD ORDER POLYNOMIAL IS USED TO REMOVED THE ANATOMY AND SMOOTH THE MAGNITUDE PROFILE (TOP), B0 MAP IS USED TO REWIND THE PHASE OF THE PHASE PROFILE (BOTTOM) 67
FIGURE 27: A) AN 8-CHANNEL EXCITATION BODY ARRAY SYSTEM, B) AN 8-CHANNEL EXCITATION HEAD ARRAY SYSTEM. 68
FIGURE 28: A) BODY-ARRAY EXCITATION: B_0 MAP (TOP-LEFT) SHOWS LARGE INHOMOGENEITY IN THE FRONTAL SINUS AREA, SLICE-SELECTIVE EXCITATION WITHOUT (TOP-RIGHT) AND WITH (BOTTOM-LEFT) B_0 CORRECTION. SLICE PROFILE IS ALSO SHOWN (BOTTOM-RIGHT). B) HEAD-ARRAY EXCITATION: 2X ACCELERATION "TIM TX" EXCITATION WITHOUT (RIGHT) AND WITH (CENTER) B_0 CORRECTION. 4X ACCELERATION "HALF BRAIN" EXCITATION WITHOUT B_0 CORRECTION (LEFT). 69
FIGURE 29: THE RESET PULSE SEQUENCE USED IN *SATURATED* DOUBLE-ANGLE METHOD. SEQUENCE DIAGRAM IN (A) SHOWS THE SATURATION PULSE (M_Z RESET) BEING APPLIED AFTER EACH DATA ACQUISITION TO SATURATE MZ PRIOR TO THE NEXT EXCITATION. THE M_z TIME COURSE OF THIS SEQUENCE IS SHOWN IN (B). 74
FIGURE 30: FLOWCHART OUTLINING THE RAPID QUANTITATIVE B1+ MAPPING TECHNIQUE, WHERE FIRST RECEIVE PROFILE OF THE RECEPTION COIL IS ESTIMATED IN STEP 1-5, AFTER WHICH B1+ MAPS OF THE TRANSMIT COILS (OR MODES) CAN THEN BE OBTAIN VIA STEP 6-7. 79
FIGURE 31: A) EIGHT-CHANNEL TRANSMIT/RECEIVE STRIPLINE COIL ARRAY FOR 7T. THE INSERT ON THE RIGHT PANEL OF A) SHOWS THE ESTIMATED TRANSMIT (TX) AND RECEIVE (RX) PROFILES AND THE TRANSMIT-RECEIVE IMAGE (TX-RX) OF THE CP MODE OF THE ARRAY FOR A WATER-FILLED SPHERICAL PHANTOM PLACED INSIDE A LOADING RING. B) THE UPPER PANEL SHOWS ESTIMATED MAGNITUDE (INTENSITY SCALE NORMALIZED TO A MAXIMUM VALUE OF 1), AND THE LOWER PANEL SHOWS PHASE (DEGREES) OF THE INDIVIDUAL EXCITATION COIL PROFILES. 81
FIGURE 32: A) SIXTEEN-CHANNEL TRANSMIT/RECEIVE STRIPLINE COIL ARRAY FOR 7T, AND THE BUTLER MATRIX HARDWARE THAT WAS USED FOR THE EXPERIMENTS IN THIS WORK. THE INSERT ON THE RIGHT PANEL OF A) SHOWS THE ESTIMATED TRANSMIT (TX) AND RECEIVE (RX) PROFILES AND THE TRANSMIT-RECEIVED IMAGE (TX-RX) OF THE CP MODE OF THE ARRAY FOR A WATER-FILLED SPHERICAL PHANTOM. B) THE UPPER PANEL SHOWS THE ESTIMATED MAGNITUDE PROFILE (INTENSITY SCALE NORMALIZED TO A MAXIMUM VALUE OF 1), AND THE LOWER PANEL SHOWS THE PHASE PROFILE (IN DEGREES) OF THE EIGHT ORTHOGONAL BIRDCAGE TRANSMISSION MODES USED. 81
FIGURE 33: FLOW DIAGRAM OF THE MODIFIED LOCAL-VARIABLE EXCHANGE METHOD FOR MAGNITUDE LEAST SQUARE OPTIMIZATION. DURING THE ITERATIVE OPTIMIZATION PROCESS, A SMOOTHED VERSION OF THE EXCITATION PHASE FROM THE PREVIOUS ITERATION IS USED AS THE TARGET

EXCITATION PHASE FOR THE CURRENT ITERATION. THE SMOOTHING OF THE EXCITATION PHASE PROFILE IS PERFORMED USING A DESIGNER-SPECIFIED GAUSSIAN FILTER, ENABLING THE DESIGNER TO SYSTEMATICALLY TRADE OFF THE ALLOWED SPATIAL PHASE VARIATION FOR AN IMPROVEMENT IN THE MAGNITUDE PROFILE AND REDUCTION IN RF POWER. 87
FIGURE 34: EIGHT-CHANNEL TRANSMIT/RECEIVE STRIPLINE COIL ARRAY FOR 7T THAT WAS USED FOR ALL EXPERIMENTS IN THIS CHAPTER. THE INSERT ON THE RIGHT PANEL OF A) SHOWS THE ESTIMATED TRANSMIT (TX) AND RECEIVE (RX) PROFILES AND THE TRANSMIT-RECEIVED IMAGE (TX-RX) OF THE BIRDCAGE MODE OF THE ARRAY FOR A WATER-FILLED SPHERICAL PHANTOM PLACED INSIDE A LOADING RING. ALSO SHOWN IS AN EXAMPLE OF THE TRANSMIT-RECEIVED IMAGE (TX-RX) OF THE BIRDCAGE MODE OF THE ARRAY FOR AN AXIAL BRAIN SECTION THAT DEMONSTRATES COMPARABLE INHOMOGENEITY TO THE TRANSMIT-RECEIVED IMAGE OF THE PHANTOM. 89
FIGURE 35: **A)** EXPERIMENTAL SQUARE-TARGET EXCITATION, IMAGED IN A CENTRAL AXIAL SECTION OF A 3D-ENCODED READOUT. THE FIGURE ILLUSTRATES THE EXCITATION MAGNITUDE PROFILE IMPROVEMENT WITH THE MAGNITUDE LEAST SQUARES DESIGN WHEN COMPARED TO THE CONVENTIONAL LEAST SQUARES DESIGN FOR THE TIKHONOV REGULARIZATION PARAMETER VALUE OF 1.5. THE TOP ROW COMPARES THE OVERALL EXCITATION. THE WINDOW AND LEVEL PARAMETERS FOR THE SECOND ROW ARE SET TO BRING OUT THE BACKGROUND NOISE, AND THE THIRD ROW IS WINDOWED TO BEST COMPARE THE INTENSITY VARIATION WITHIN THE SQUARE TARGET EXCITATION. **B)** PLOT OF NORMALIZED RMMSE VS. RF VOLTAGE NORM ACROSS ALL 8 CHANNELS ($\|b\|_2$), FOR FOUR DIFFERENT SETTINGS OF THE TIKHONOV REGULARIZATION PARAMETER (L-CURVE). 93
FIGURE 36: EXPERIMENTAL SQUARE-TARGET EXCITATION FOR A FIXED VALUE OF TIKHONOV REGULARIZATION PARAMETER ($\beta = 1.5$), MAGNITUDE (LEFT) AND PHASE (RIGHT) BY, **A)** CONVENTIONAL LEAST-SQUARES OPTIMIZATION, AND **B)** BY MAGNITUDE LEAST SQUARES. LARGER VARIATION OF SPATIAL PHASE PROFILE IS OBSERVED FOR THE MAGNITUDE LEAST SQUARES DESIGN AS EXPECTED. ADDITIONALLY, THE MLS DESIGN YIELDS BETTER TARGET EXCITATION AND BACKGROUND SUPPRESSION WITHIN THE PHANTOM OUTSIDE THE TARGET SQUARE. PANEL **C)** SHOWS A ZOOMED REGION OF THE PHASE PROFILE FROM THE MLS DESIGN, AND SHOWS THE HIGH DEGREE OF SIMILARITY BETWEEN EXPERIMENTAL (LEFT) AND SIMULATION RESULTS (RIGHT). 94
FIGURE 37**: A) & B)** ACQUIRED DATA AND SIMULATION RESULTS FOR A 4-SPOKE EXCITATION BY CONVENTIONAL LEAST-SQUARES (A), AND MAGNITUDE LEAST SQUARES (B), FOR THE TIKHONOV REGULARIZATION PARAMETER PAIR THAT RESULTED IN THE LOWEST EXPERIMENTAL RMMSE. IN EACH PANEL, THE TOP ROW SHOWS THE EXPERIMENTAL IN-PLANE AND THROUGH-SLICE PROFILES, WHILE THE LOWER RIGHT IMAGE SHOWS THE PREDICTED PROFILE BASED ON A BLOCH-EQUATION SIMULATION OF THE RF WAVEFORMS. THE BOTTOM LEFT FIGURE IN EACH PANEL SHOWS SEVERAL SECTIONS THROUGH THE IN-PLANE PROFILE. **C)** L-CURVE PLOT OF THE NORMALIZED RMMSE VS. RF VOLTAGE NORM ACROSS ALL 8 CHANNELS ($\|b\|_2$), FOR SIX DIFFERENT SETTINGS OF THE TIKHONOV REGULARIZATION PARAMETER. 96
FIGURE 38: EXPERIMENTAL MAGNITUDE (LEFT) AND PHASE (RIGHT) RESULTS FOR A 4-SPOKES EXCITATION BY CONVENTIONAL LEAST-SQUARES (A), AND MAGNITUDE LEAST SQUARES (B), FOR THE TIKHONOV REGULARIZATION PARAMETER PAIR THAT RESULTED IN THE LOWEST EXPERIMENTAL RMMSE. LARGER VARIATION OF SPATIAL PHASE PROFILE IS OBSERVED FOR THE MAGNITUDE LEAST SQUARES DESIGN AS EXPECTED. ADDITIONALLY, THE MLS DESIGN YIELDS A MUCH MORE UNIFORM MAGNITUDE PROFILE. PANEL **C)** SHOWS A ZOOMED PHASE SCALING VERSION OF THE PHASE PROFILE FROM THE MLS DESIGN, AND SHOWS THE HIGH DEGREE OF SIMILARITY BETWEEN EXPERIMENTAL (LEFT) AND SIMULATION RESULTS (RIGHT). 97
FIGURE 39: A) PROFILES FOR COMBINED TX-RX, ALONG WITH ESTIMATES OF THE SEPARATE TX AND RX OF THE MODE-1 BIRDCAGE OF THE COIL FOR A HEAD SHAPED PHANTOM, AND B) HUMAN BRAIN (SUBJECT 1). 102
FIGURE 40: MAGNITUDE (TOP) AND PHASE (BOTTOM) B_1^+ MAPS OF THE 8 OPTIMAL MODES FOR A) THE HEAD-SHAPED PHANTOM, AND B) AN AXIAL SECTION IN HUMAN BRAIN (SUBJECT 1). 104
FIGURE 41: THE OPTIMIZED THREE (A) AND TWO-SPOKE (B) K-SPACE TRAJECTORIES FOR THE PULSE DESIGN IN THE HEAD-SHAPED PHANTOM AND HUMAN EXCITATION EXPERIMENT RESPECTIVELY. THE OPTIMIZED TWO-SPOKE PLACEMENTS IN (K_X,K_Y) FOR THE IN THE IN VIVO EXPERIMENTS VARIED SLIGHTLY FROM SUBJECT TO SUBJECT, BUT IN ALL CASES WERE TWO-SPOKE DESIGNS. 105

FIGURE 42: HEAD-SHAPED WATER PHANTOM B_1^+ MITIGATION. FLIP-ANGLE MAPS AND LINE PROFILES FOR: A) BIRDCAGE MODE WITH CONVENTIONAL 1-MS LONG SINC SLICE-SELECTIVE EXCITATION, DEMONSTRATING A 1:6.8 MAGNITUDE VARIATION WITHIN THE FIELD-OF-EXCITATION (FOX); B) RF SHIMMING, 1 MS-LONG PULSE, DEMONSTRATING A SUBSTANTIAL RESIDUAL FLIP-ANGLE INHOMOGENEITY AS MEASURED BY THE RESIDUAL STANDARD DEVIATION AND THRESHOLD METRICS; AND, C) THREE-SPOKE MLS, SLICE-SELECTIVE 2.4-MS LONG PULSE, DEMONSTRATING EXCELLENT MITIGATION OF THE B_1^+ INHOMOGENEITY. 109
FIGURE 43: COMPARISON OF B_1^+ MITIGATION BY A) A LEAST-SQUARES, AND B) A MAGNITUDE-LEAST-SQUARES 3-SPOKE RF DESIGN WITH THE SAME K-SPACE TRAJECTORY (2.4 MS) AND PULSE SHAPE (SINC, TIME-BANDWIDTH PRODUCT=4) AS DEMONSTRATED ON A HEAD-SHAPED WATER PHANTOM WITH SUBSTANTIAL TX INHOMOGENEITY. ON THE LEFT IS A BLOCH SIMULATION OF THE MAGNITUDE AND PHASE PROFILES, ON THE RIGHT ARE EXPERIMENTAL RESULTS WITH LINE PROFILES THROUGH THE MAGNITUDE IMAGE. ALSO SHOWN, BOTTOM RIGHT, IS THE EXCITATION PHASE PROFILE. 110
FIGURE 44: COMPARISON OF PHASE DUE TO THE EXCITATION ONLY (LEFT) AND PHASE MEASURED IN A GRADIENT ECHO AT TE=5MS, WHICH ALSO INCLUDES THE ACCRUAL OF PHASE DUE TO B_0 INHOMOGENEITY (CENTER). THE $B_0(X,Y)$ TERM IS ACCORDING TO A SEPARATELY ESTIMATED B_0 FIELDMAP (RIGHT). CLEARLY, THE EXCITATION PHASE VARIATION RESULTING FROM THE MLS DESIGN IS VERY SMALL COMPARED TO THE ACCRUED PHASE DUE TO B_0 INHOMOGENEITY AT TE=5MS, AND IS SLOWLY VARYING OVER THE FOX, AND THUS DOES NOT INTRODUCE ANY INTRA-VOXEL DEPHASING. 111
FIGURE 45: B_1^+ MITIGATION COMPARISON FOR SUBJECT 1. THE COMPARISON INCLUDES SLICE SELECTION BASED ON MODE-1 BIRDCAGE (TOP ROW), RF SHIMMING (CENTER ROW), AND TWO-SPOKE (BOTTOM ROW) EXCITATION PULSES. ON THE LEFT OF EACH ROW IS THE IN-PLANE IMAGE OF THE EXCITED SLICE AFTER THE REMOVAL OF THE RECEIVE PROFILE. ON THE RIGHT IS THE FLIP-ANGLE MAP ESTIMATE, ALONG WITH THE LINE PROFILE PLOTS. 113
FIGURE 46: B_1^+ MITIGATION COMPARISON FOR SUBJECT 5, WHO HAS THE MOST SEVERE B_1^+ VARIATION (IN THE MODE-1 BIRDCAGE EXCITATION) OUT OF ALL THE SIX SUBJECTS. 114
FIGURE 47: TWO-SPOKE EXCITATION FOR SUBJECT 4 WITH A 3D READOUT. A) SLICE PROFILE PLOT, WHERE THE SOLID LINE REPRESENTS THE PREDICTED PROFILE AND THE CIRCLES REPRESENT THE EXPERIMENTAL DATA. EACH DATA POINT ALONG THE SLICE PROFILE REPRESENTS THE AVERAGE IN-PLANE INTENSITY AT THAT PARTICULAR Z-LOCATION. B) IN-PLANE IMAGES (A)-(J), AT 1-MM SEPARATION ALONG Z, OVER A 1-CM RANGE AROUND THE 0.5-CM EXCITED SLICE. 117
FIGURE 48: K-SPACE TRAJECTORY FOR THE 4-SPOKES EXCITATION IS SHOWN ON THE LEFT. ON THE RIGHT ARE THE RF WAVEFORM FOR ONE OF THE EIGHT TRANSMISSION MODES (MODE 1), AND THE GRADIENT WAVEFORMS THAT WERE USED FOR THE EXCITATION. 124
FIGURE 49: IN-PLANE EXCITATION PROFILES AT CENTER FREQUENCY FOR RF SHIMMING, CONVENTIONAL SPOKE, AND SPECTRAL-SPATIAL SPOKE EXCITATIONS RESPECTIVELY. 127
FIGURE 50: STANDARD DEVIATION PLOTS COMPARING **A)** THE SIMULATED PERFORMANCE OF THE THREE TYPES OF EXCITATION DESIGNS, AND **B)** THE SIMULATED AND EXPERIMENTAL PERFORMANCE OF THE SPECTRAL-SPATIAL SPOKE EXCITATION DESIGN OVER A ±500 HZ FREQUENCY RANGE. 128
FIGURE 51: EXCITATION PERFORMANCE ACHIEVED BY THE SPECTRAL-SPATIAL PULSE AT 300 HZ OFF-RESONANCE WITH THE THROUGH-SLICE PROFILE (TOP), THE IN-PLANE PROFILES AT 3 DIFFERENT THOUGH PLANE POSITIONS ALONG THE EXCITED SLAB (CENTER), AND THE CORRESPONDING 1-D PROFILES AT SEVERAL CUTS THROUGH THE IN-PLANE PROFILES (BOTTOM). EXCELLENT SLICE SELECTION AND GOOD IN-PLANE PROFILES CAN BE OBSERVED. 130
FIGURE 52: SUMMARIZES THE EXCITATION PERFORMANCE ACHIEVED BY THE SPECTRAL-SPATIAL PULSE AT 0 HZ OFF-RESONANCE. EXCELLENT SLICE SELECTION AND GOOD IN-PLANE PROFILES CAN BE OBSERVED. 130
FIGURE 53: SUMMARIZES THE EXCITATION PERFORMANCE ACHIEVED BY THE SPECTRAL-SPATIAL PULSE AT -300 HZ OFF-RESONANCE. EXCELLENT SLICE SELECTION AND GOOD IN-PLANE PROFILES CAN BE OBSERVED. 131
FIGURE 54: FROM LEFT TO RIGHT: THE MAGNITUDE AND PHASE PROFILES FOR THE CENTER SLICE OF THE EXCITED SLAB AT -200, 0, AND +200 HZ RESPECTIVELY. THE MAGNITUDE PROFILE EXHIBITS GOOD UNIFORMITY AT ALL THREE FREQUENCIES WHILE, AS EXPECTED FROM THE MLS OPTIMIZATION, THE PHASE PROFILE VARIES SMOOTHLY BOTH SPATIALLY AND SPECTRALLY. 131

FIGURE 55: EXCITATION PROFILES FROM THE 3-SPOKE 90° EXCITATION, **LEFT:** THE IN-PLANE AND THE SLICE SELECTION PROFILES, **RIGHT:** THE 1-D THROUGH-PLANE PROFILES ALONG SEVERAL CUTS THROUGH THE IN-PLANE PROFILE. 145
FIGURE 56: SIMULATION AND EXPERIMENTAL DATA PLOTS OF THE NORMALIZED AVERAGE IN-PLANE INTENSITY AS A FUNCTION OF PEAK RF VOLTAGE FOR THE 3-SPOKES 90° EXCITATION. GOOD AGREEMENT BETWEEN THE SIMULATION AND EXPERIMENTAL DATA CAN BE OBSERVED. 145
FIGURE 57: Z-GRADIENT (G_z) AND RF WAVEFORMS FROM ONE OF THE EXCITATION COIL (COIL 1) FOR THE VERSED SPIN-ECHO SEQUENCE CONSISTING OF A 3-SPOKE 90° AND180° SPIN-ECHO EXCITATIONS (TE = 20 MS). ALSO SHOWN ARE THE G_z CRUSHER GRADIENTS SURROUNDING THE SPIN-ECHO RF. 146
FIGURE 58: SPIN-ECHO EXCITATION PROFILES, **LEFT:** THE IN-PLANE AND THE SLICE SELECTION PROFILES, **RIGHT:** THE 1-D THOUGH-PLANE PROFILES ALONG SEVERAL CUTS THROUGH THE IN-PLANE PROFILE. 147
FIGURE 59: **TOP:** THE PHASE IMAGES OBTAINED FROM THE STANDARD (LEFT) AND THE MODIFIED (RIGHT) SPIN-ECHO SEQUENCES. **BOTTOM:** THE RELATIVE PHASE DIFFERENCE IMAGE, WITH OBSERVED PHASE DIFFERENCE OF -90° AS PREDICTED. 147

Introduction

Magnetic resonance imaging (MRI) is an important and widespread medical imaging modality used in visualizing the structure and function of the human body. It provides great soft-tissue contrast, making it the preferred imaging method for diagnosing many soft-tissue disorders, especially those found in the brain, spinal cord, and pelvis (for review see (1-4)).

Magnetic resonance imaging can be thought of as a two-phase experiment. The first phase is termed the excitation phase and involves the creation of MR signal in the subject via the use of a Radio Frequency (RF) magnetic pulse. The second phase is termed the acquisition phase and involves the manipulation and collection of the generated signal. Generally, these two phases are repeated pair-wise many times to acquire enough data to create an image. This thesis is concerned mainly with the excitation phase of MRI, in particular in the RF magnetic pulse design algorithms for high magnetic field MRI.

In general, during the excitation phase, the signal generation (via RF excitation) is tailored to be localized to a specific region within the subject such as to a 3D slab or a relatively thin 2D slice. The subsequent acquisition phase encodes a 3D slab in all three dimensions, while slice selection of a thin slice is resolved only in-plane by the acquisition phase. This localization stage of the RF excitation provides the relevant signal manipulation to produce a clinical image with the desired contrast, resolution, and field of view. To create localized excitations, tailored RF pulses are required. For typical commercial MRI scanners operating at a main magnetic field strength, B_0, of 1.5 Tesla (T) or lower, single-slice or slab-selective excitations are relatively simple to

design, and are routinely employed with great success in clinical and diagnostic imaging.

In recent years there has been a push towards higher magnetic field strength scanners to achieve dramatic improvements in image signal-to-noise ratio (SNR) and contrast. However, conventional lower-field RF design assumptions are no longer valid, and to realize the benefits of high-field imaging for human studies, new RF excitation pulse designs are needed. At present, the most critical and pressing problem in brain imaging at 7 T is what is commonly referred to as 'center brightening' (5-7), a dramatic spatial variation in the magnitude of the RF excitation magnetic field, B_1^+, leading to very unfavorable spatial non-uniformity in the excitation across the region of interest, and greatly limiting many conventional excitations. Solving this B_1^+ inhomogeneity problem is essential in bringing very high-field human MRI to clinical use.

RF pulses with spatially tailored excitation pattern can be used to mitigate B_1^+ inhomogeneity by exciting a spatial inverse of the inhomogeneity. While theoretically feasible with conventional RF excitation systems, the primary limitation of such pulses is in their long duration, which makes them impractical for clinical imaging. The goal of this work is to mitigate the B_1^+ excitation problem at high field while satisfying the constraint of sufficiently short RF pulses. To achieve this goal, parallel transmission is employed, whereby multiple RF excitation coils are used simultaneously instead of the single RF coil used on conventional scanners. With this technique, RF pulse duration can be dramatically shortened, but at the cost of more RF excitation channels, complicated excitation arrays, numerous (expensive) power amplifiers, and substantially more complicated RF pulse design. A second goal of this thesis is the extension of traditional slice-selective RF pulses, which shape the excited area in 1 dimension, to generalized 2D and 3D shapes. This has previously not been practical due to the lengthy RF pulse required, but becomes possible with parallel transmit designs.

Prior work in parallel transmission includes the theoretical formulation of linear approximation design algorithms for multi-channel RF design (8-11), which emerged in

2002, but because of expensive hardware implementation for demonstration, experimental verification was limited. In 2005, at the initiation of the research effort described in this thesis, experimental verification had only been carried out by emulation on a single-coil RF transmission system (8,9), and one report of phantom experiments using a 3-channel human, and 4-channel animal scanners at 3T and 4.7T respectively was published in the very early phase of this work (12).

The focus of this dissertation is on the algorithm design, implementation, and validation of parallel transmission technology, ultimately with applications in human imaging. Novel algorithms are proposed which resulted in excellent excitation control, low RF power requirements, and methods that extend to non-linear large-flip-angle excitation, as well as a new algorithm for simultaneous spectral and spatial excitation critical to quantification of brain metabolites. For testing and validation, these methods were implemented on a newly developed parallel transmission platform on both 3T and 7T MRI scanners with 8-channel transmission to demonstrate the ability of these methods for high-fidelity B_1^+ mitigation. Further, spatially tailored RF pulses were demonstrated beyond conventional slice- or slab-selective excitation. The novel methods presented in this work will be essential to robust clinical applications in future high-field human imaging.

The structure of the dissertation is as follows:

Chapter 1 presents a brief introduction to MRI along with the background for single-channel and multi-channel RF excitation designs. In addition, to motivate subsequent chapters, explanation of image contrast generation and the detrimental effect of B_1^+ inhomogeneity on contrast are given.

Chapter 2 describes the implementation of parallel transmission design on a prototype 8-channels RF system at 3 T for both a phantom and human subjects, successfully demonstrating the capability of the technique in creating short RF excitation pulses for mitigating B_1^+ inhomogeneity, and for providing excitation of arbitrarily shaped volumes. This work was published as references (13-15).

Chapter 3 describes a technique to rapidly obtain spatial B_1^+ profiles of RF coils at ultra high-field strength. The spatial B_1^+ profiles of RF transmission coils are crucial inputs for parallel transmission designs. In Chapter 2 at 3T, due to relatively low filed strength, a simple technique could be used to obtain a good estimation of these profiles. However, at 7T, this technique fails.

Chapter 4 presents a magnitude-least-squares (MLS) optimization technique for parallel RF transmission design. The method trades off unimportant slowly-varying in-plane excitation phase variation for substantial and very valuable improvement in excitation magnitude profile and reduced power. The technique was validated on a water phantom at 7 T using an 8-channel transmit system. This work has been published as reference (16).

Chapter 5 presents results from in vivo experiments at 7T where parallel transmission was used to both mitigate severe B_1^+ inhomogeneity (~3:1 peak-to-trough magnitude variation of B1+) and to create excitation of arbitrarily shaped volume in the human brain. A comparison of B_1^+ mitigation performance by parallel transmission and currently available techniques is also presented, demonstrating the superior performance achieved by parallel transmission. This work has been submitted for publication in *MRM.*

Chapter 6 describes a new design algorithm for spectral-spatial excitations. Apart from being selective in the spatial domain, spectral-spatial excitations are also selective in the spectral domain, allowing for e.g. selective excitation of certain metabolites that reside within a specific spectral band. To improve the capability of these excitations, parallel spectral-spatial excitation design method is formulated. The method was validated via the design and phantom implementation of an excitation pulse that simultaneously mitigates spatial B_1^+ inhomogeneity and provides uniform excitation over a 600 Hz spectral Bandwidth at 7T. This work has been submitted for publication in *MRM.*

Chapter 7 covers the design algorithm, implementation for efficient computation, and phantom demonstration at 7T of RF pulses in the large-tip-angle regime. Note, parallel

transmission algorithms described in prior chapters all rely on a linear approximation to the highly non-linear Bloch equation, and can not be use to design excitations in this large-tip-angle regime. This work has been submitted for publication in *JMR*.

Chapter 8 summarizes the major results for the thesis with direction for future work outlined.

This thesis is organized progressively with background and basic results presented in chapter 1 and 2. Chapter 3 presents the work on a B_1^+ mapping technique which is crucial to high-field parallel transmission implementation. Nonetheless, knowledge of B_1^+ mapping technique is not required for understanding the subsequence chapters. Chapters 5-7 rely on the work from Chapter 4 but are not themselves inter-related and hence could be read independently

Chapter 1

Background: RF Excitation in MRI

The aim of this chapter is to provide the reader with the relevant background for understanding the work carried out in this thesis. First a brief description of MRI is presented follow by an outline of the theory for single and multi-channel RF excitations. In addition, to motivate subsequent chapters, explanation of image contrast generation and the detrimental effect of B_1^+ inhomogeneity on contrast are given. The focus of this chapter will be mainly on the excitation phase of MRI. For more details on the acquisition phase and the general descriptions of MRI please refer to (17-19).

1.1 Magnetic Resonance Imaging

Signal Origin

Atoms with an odd number of protons or neutrons possess a nuclear spin angular momentum. Qualitatively, these nuclei can be visualized as spinning, charged spheres that give rise to a small magnetic moment. In the human body, which consists largely of water, hydrogen nuclei possess this spin behavior, and are the signal source for conventional MR imaging. In different parts of the body, hydrogen concentration and the local water environment differ, for example, the white and gray matter in the brain, giving rise to tremendously valuable soft-tissue contrast for clinical MR imaging.

Signal Generation and Detection

MR imaging is a two-phase experiment. The excitation phase which involves exciting magnetic moments away from their minimum energy state, and thereby producing a detectable signal. During the subsequent acquisition phase, the signal is detected via induction, encoded, and collected as the spins relax back to the minimum energy state.

Three magnetic fields are used in MR imaging.

1) Main Field (B_0)

In MRI, a constant main field, B_0, applied along the positive z-direction, is always present. In the absence of an external magnetic field, magnetic moments in the body are randomly orientated. Applying a strong, static magnetic field will have two notable effects. First, a small fraction of the magnetic moments will align with the applied field. Second, once excited the magnetic moments will precess at the Larmor frequency. This frequency, w, is linearly related to the strength of the applied field, i.e. $w = \gamma B$, where γ is the gyromagnetic ratio, which is a constant for a given nucleus.

2) Radiofrequency Field (B_1)

During the excitation phase, a radiofrequency (RF) magnetic pulse B_1, tuned to the resonant frequency of the magnetic moment, is applied in the x-y (transverse) plane using RF transmission coil(s). This pulse will create a torque that rotates the magnetic moments away from their minimum energy state (parallel to B_0). If the excitation is calibrated to produce a 90° tip angle, then after turning the excitation off, the magnetic moments would have rotated from the z direction into the x-y plane. With the B_0 field present, the magnetic moments, which are now oriented in the x-y plane, spin at the Larmor frequency (Figure1). During the acquisition phase, due to the spinning of the magnetic moments in x-y plane, Faraday's law of induction predicts the generation of an electromotive force (EMF) in properly oriented RF receiver coil(s). Thus it is only the x-y component of the magnetization which contributes to the signal. Note, in many cases the same set of coils are employed for both RF pulse transmission and data reception.

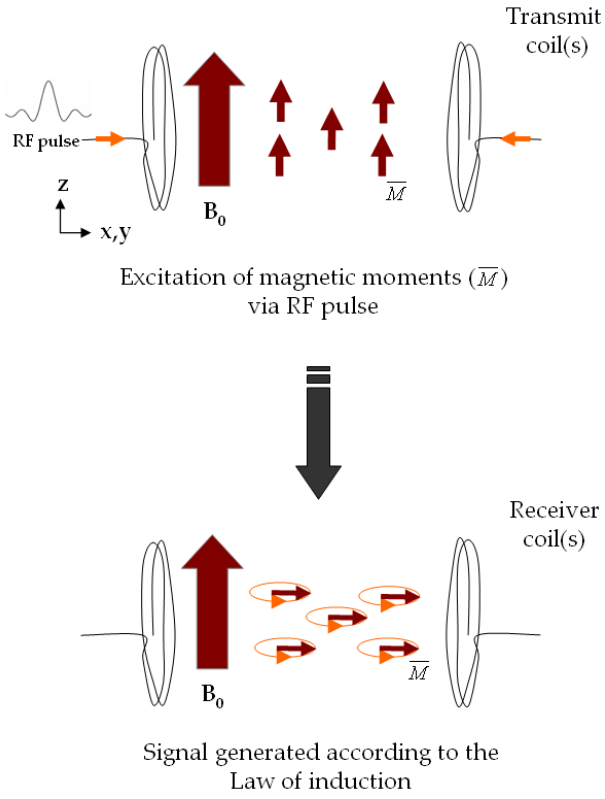

Figure1: RF excitation and signal generation

3) Linear Gradient Fields (G)

The gradient field, G, is a z-direction magnetic field whose strength varies linearly with spatial position ($\bar{r}$) over the imaging region. When a gradient field is applied, the net magnetic field at a particular point in space is given by $B(\bar{r}) = B_0 + \bar{G} \cdot \bar{r}$. Consequently, the spin frequency, $w(\bar{r})$, also varies according to $w(\bar{r}) = \gamma(B_0 + \bar{G} \cdot \bar{r})$.

The gradient field plays an important role both in the excitation and the acquisition phase of MR imaging. During the excitation phase, the gradient field can be used to selectively excite, or tip, the magnetic moments in a particular region of interest. If the gradient field is applied during excitation, the spin frequency of the magnetic moments at different spatial locations will differ. Therefore, the RF field, which is tuned to the central Larmor frequency ($w = \gamma B_0$), will have different effects on magnetic

moments at different spatial locations. The exact relationship governing this effect will be presented in the next section.

To be able to create an image during the acquisition phase, it is of particular importance to be able to differentiate between signals from various spatial locations. In the presence of gradient fields, the magnetic moments at different locations spin at different frequencies. Therefore, the resultant frequencies detected during the acquisition phase vary. This phenomenon is illustrated in Figure 2.

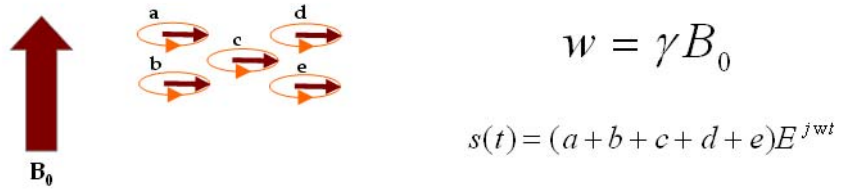

Gradient field OFF: no signal modulation

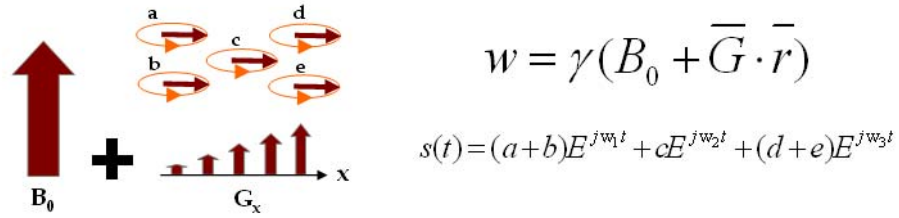

Gradient field ON: signal modulation as a function of position

Figure 2: employing gradient field for signal acquisition

1.2. RF Excitation Pulse Design

This thesis is focused mainly on the excitation phase of MRI, in particular on the RF and gradient pulse design methods with the goal of controlling excitation of magnetization in various regions of interest. Generally, during the excitation phase, the excitation is tailored to be localized to a specific region within the subject such as to a 3D slab or a 2D slice in the axial plane. To create localized excitations; tailored RF and gradient pulses are required. In this section, basic theory and prior work on single-channel and multi-

channel excitation designs are presented, and the ability of the multi-channel design to shortening RF and gradient pulse duration is explained.

1.2.1 Single Channel transmission Theory

The rotations of the magnetic moments ($\overline{M}$) caused by the applied magnetic field ($\overline{B}$) can be described by the so-called Bloch equation, a governing equation that describes the behavior of nuclear magnetization in the presence of externally applied fields (20).

Equation 1

$$\frac{d\overline{M}}{dt} = \overline{M} \times \gamma \overline{B} - \frac{M_x \hat{i} + M_y \hat{j}}{T_2} - \frac{(M_z - m_0)\hat{k}}{T_1}$$

where γ is the gyromagnetic ratio, T_1 and T_2 are the longitudinal and transverse relaxation time constants, and m_0 is the equilibrium sample magnetization due to B_0 (referring to the magnetic moments that has been aligned to the positive z-axis by the B_0 field). Equation 1 is non-linear and in general hard to use in the design of the RF excitation pulses (B_1). However, for the regime of small tip angles and a short excitation pulses (where relaxation effects (T_1 &T_2) can be ignored), the so-called small tip angle approximation (21), yields the following linear equation that can be used to describe the transverse (x-y) magnetization (m_{xy}) as a function spatial position ($\bar{r}$) due to an RF pulse envelope, $B_1(t)$.

Equation 2

$$m_{xy}(\bar{r}) = i\gamma m_0 \int_0^T B_1(t) e^{i\bar{r}\cdot\bar{k}(t)} dt$$

where

Equation 3

$$\bar{k}(t) = -\gamma \int_t^T \overline{G}(s) ds$$

The key observations relating to this equation are

- The RF excitation pulse (B_1) and the Gradient field ($\overline{G}$) can be used to control the transverse magnetization (i.e. the amount of excitation) at various locations of the image.
- Equation 2 can be viewed as a Fourier relation between the RF pulse envelope (B_1) and the transverse magnetization (m_{xy}). This provides the designer with an appealing and powerful description of RF excitation where the gradient field ($\overline{G}$ (t)) is used to traverse a path in Fourier space ("excitation $\overline{k}$-space"), while B_1(t) describes the weighting (deposition of RF energy) of the excitation k-space along this path.

Note: Even though the small tip angle approximation was used in deriving this design method, in most cases the resulting RF and gradient pulses will create good excitation profile up to a relatively large tip angle, even up to 90° in some cases (21). Thus, a large class of clinically useful RF pulses can be adequately designed with simply a linear approximation of the Bloch equations that yields the intuitive Fourier relationship.

Fourier Relationship

Equation 2 can be viewed as a Fourier relation between the RF pulse (B_1) and the transverse magnetization (m_{xy}), with the gradient field ($\overline{G}$) used in moving around in the Fourier space ($\overline{k}$). To illustrate this relation we turn our attention to the slice selective excitation, where the aim is to selectively excite only a thin slice in the z direction.

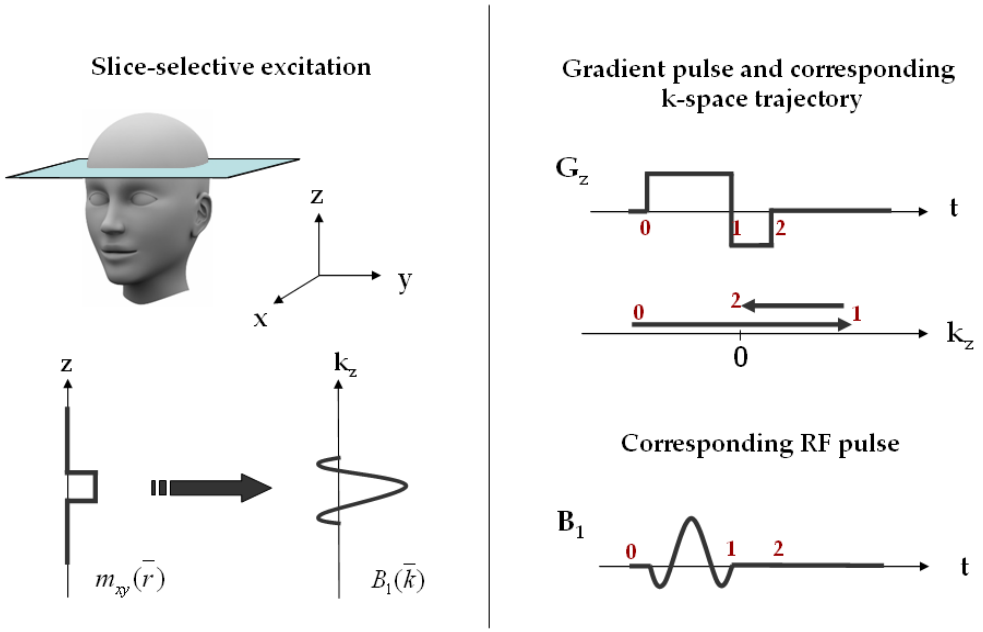

Figure 3: Slice-selective excitation; left: target excitation and its Fourier transform, right: corresponding gradient and RF pulses.

According to the Fourier relation, to excite a slice we will need to create a sinc like RF pulse in k-space (Figure 3, LHS). If we used the gradient pulse as specified on the top right of Figure 3, then the resulting k-space can be found using Equation 3. This is also shown in Figure 3. During the time period 0 to 1, the k-space trajectory travels from a negative to a positive value passing though the origin. If we play out a sinc pulse during this period then we would get the desired RF deposition in k-space.

A more involved example would be the excitation of a two dimensional target profile in the x-y plane (no variation in the z-direction). For illustrative purposes the MIT logo is used as the target profile. Figure 4 shows the logo along with its Fourier transform. Note, in this excitation, the amount of excitation on the main part of "i" will be twice that of the other parts of the logo.

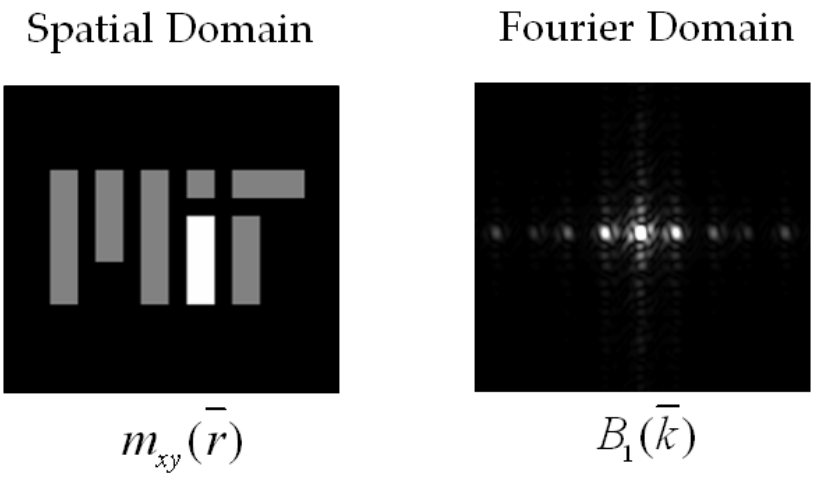

Figure 4: MIT logo target excitation profile and its transform

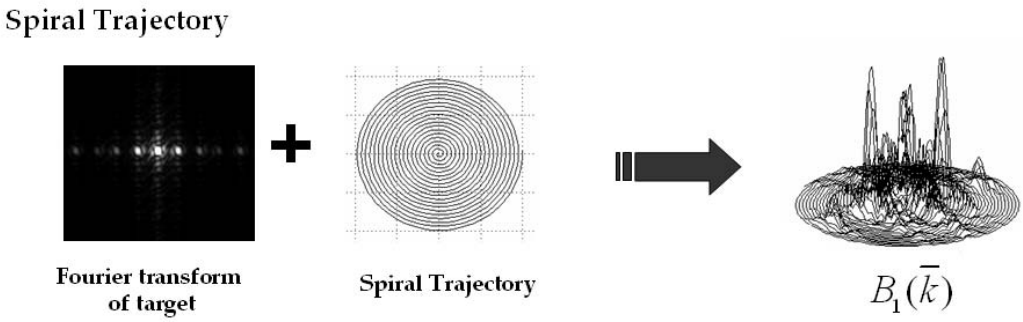

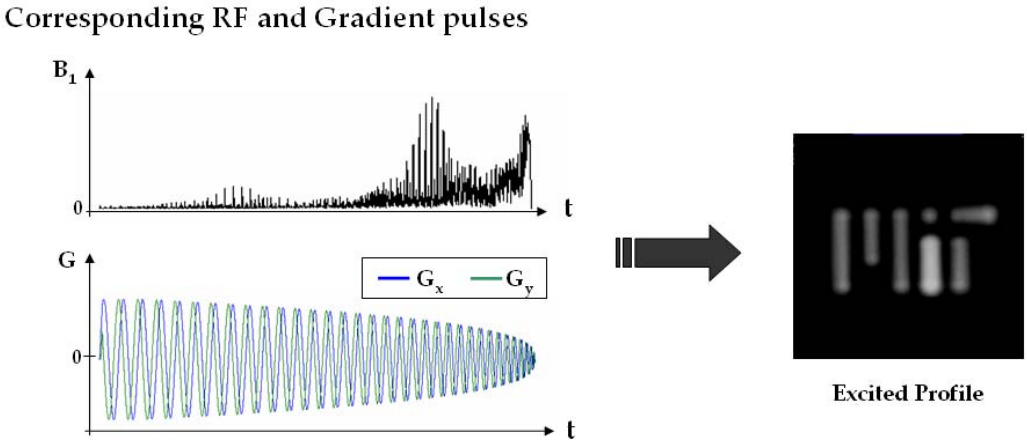

Figure 5: 2D excitation design; top: target's Fourier transform and spiral k-space trajectory, bottom: corresponding RF and gradient pulses, and the resulting excitation profile.

For the excitation design to work well, a suitable k-space trajectory must be chosen such that it will cover the two dimensional k-space sufficiently without under-sampling (i.e. taking account of aliasing). To achieve a short excitation period, the duration of the trajectory must be kept to a minimum. Hardware limitation on the maximum achievable gradient amplitude $\overline{G}$, and slew rate ($d\overline{G}/dt$), translates to limitation on the velocity and acceleration of the k-space trajectory (via Equation 3). Taking these constraints into account, a "spiral" k-space trajectory is one choice for two dimensional excitations. Figure 5 shows the spiral trajectory and, the resulting RF and gradients waveforms. Also shown is the excitation profile produced by this design in a water phantom experiment using a Siemens 3T MRI system (22).

The main intuition in designing k-space trajectories is in trying to come up with a fast trajectory path that will sufficiently cover the high energy region and not cause aliasing, while still satisfying the slew and amplitude limitations of the gradient amplifiers. Since the overall shape of the high energy region depends on the target excitation pattern, a particular trajectory will not always be suitable for every excitation pattern. Figure 6 shows, two of the many possible three dimensional k-space trajectories (22).

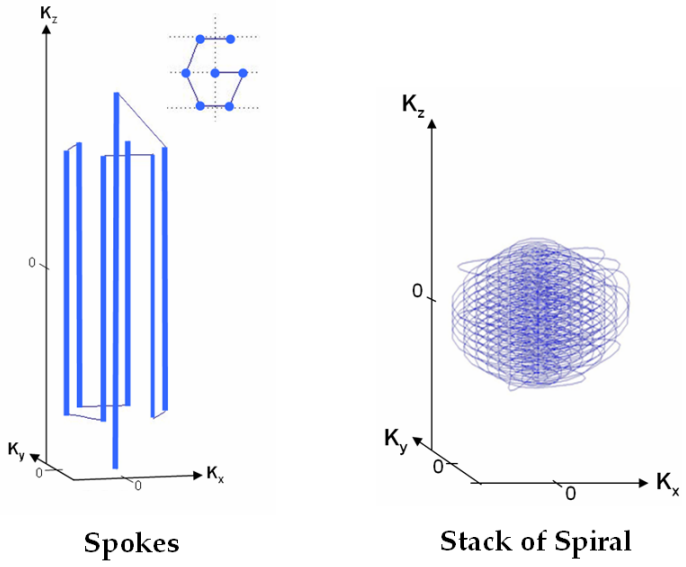

Figure 6: Spokes (left) and Stack of spiral (right) trajectories.

In this thesis, the spokes trajectory (22-25) shown in Figure 6 will be used extensively for B_1^+ inhomogeneity mitigation. The aim of this design is to create sharp slice-selective excitation using sinc-like excitation along k_z, with some control of modulating the in-plane (x-y) excitation profile to counter-act the in-plane B_1^+ inhomogeneity, via using amplitude and phase modulation of the different sinc "k_z spokes" that are place at various k_x-k_y locations, to create an excitation pattern that is a spatial inverse of the inhomogeneity. This trajectory choice is motivated by the need for relatively sharp slice profiles (i.e. large extent in kz) and relatively slowly-varying in-plane mitigation patterns (i.e. smaller coverage in k_x-k_y).

1.2.2 Parallel Transmission Theory

As previously mentioned, the technical limitation of multi-dimensional, spatially selective excitation is in the rather long duration over which the RF and the gradient pulses need to be played out. Naturally, the pulse duration increases with the shape complexity of the volume of interest. RF and gradient pulses that obey practical amplitude and slew rate limitations (ultimately limited by physiological parameters, not hardware) and excite complex patterns are often too long for clinical application and are prone to system imperfection (12); and hence are not widely used. For example, slice-selective excitations that mitigate severe B_1^+ inhomogeneity via the use of spokes trajectory can be very long because of the large number of k_z spokes required on many k_x-k_y locations to sufficiently create an in-plane excitation pattern that counteract the severe inhomogeneity.

With the emergence of parallel transmission techniques, however, excitation pulses can be shortened, or equivalently, 'accelerated' relative to the single-channel implementations (8-11). This results in the possibility of realizing more complex excitation patterns with practical pulse durations, which can be used in e.g. spatial modulation of the B1+ excitation profile to mitigate RF field inhomogeneity at high-field (26-28), and in creating high resolution image of a particular target region e.g. of a

suspected tumor (by selectively exciting only the target area, the signal acquisition phase of MRI can be modified to provide higher resolution image.

In describing parallel transmission, first an intuitive example is given to build insight into the technique. Following this, a more formal mathematical formulation is provided to allow for RF and gradient pulses design. The final part of this section will touch briefly on the important issues related to parallel transmission's RF coil design, and how parallel transmission can help mitigate B_1^+ inhomogeneity.

An Intuitive Parallel Transmission Example

To explain parallel transmission, first the concept of B_1^+ sensitivity profile is described. The B_1^+ sensitivity profile refers to the spatial variation of the RF field produced when a current is applied to the coil. The profile will depend on shape and position of the coil. In the single-channel transmission case, the RF coil is designed such that its sensitivity profile is uniform across space. Generally this is achieved via the use of a "birdcage" coil which is design to produce uniform field using the "uniform birdcage mode".[1] (Note: the uniform birdcage mode's RF field is not homogenous at high B_0 field, hence the B_1^+ inhomogeneity problem).

In Parallel transmission, RF pulses on multiple independent RF coils are transmitted jointly to produce the desired excitation pattern. The B_1^+ sensitivity profiles of these RF coils are design to be spatially varying and different. The different in the sensitivity profile among the coils is the key to shortening the excitation duration. To illustrate this, a simple idealized example is given in Figure 7 and Figure 8, where two RF coils are used to reduce the duration of a 2D excitation. In this example, the target excitation pattern will be a circle at the center of x-y origin, and a 2D k-space trajectory, termed echo-planer (EP), will be used. As shown in Figure 7, excitation acceleration will be achieved by using a k-space trajectory with sparser sampling (2x) along k_x axis; resulting in a duration reduction of two for both gradient and RF pulses. In standard

[1] The uniform birdcage mode will be explained in detail in the background section titled Parallel Transmission's RF Coil Design and Mode Compression, see pp. 35-37.

single-channel design, due to under-sampling, this accelerated EP trajectory will result in excitation warp-around into the field of view[1] (aliasing) along the x-axis as shown in Figure 7. For parallel transmission, the variation in the sensitivity profiles among the RF coils is used to get around this problem. To demonstrate this, two transmission coils with idealized sensitivity profiles are used, where profile of coil 1 is uniform across the left half of the head and profile of coil 2 is uniform across the right, with no overlapping in area between (Figure 8). With careful design of excitation pattern for each of the coil, the desired excitation pattern can be achieved using the accelerated EP trajectory. This is shown in Figure 8. Note: the excitation produced by each coil is the product of the designed excitation pattern and the coil sensitivity, and the total excitation is the sum of the excitations produced by all the transmission coils.

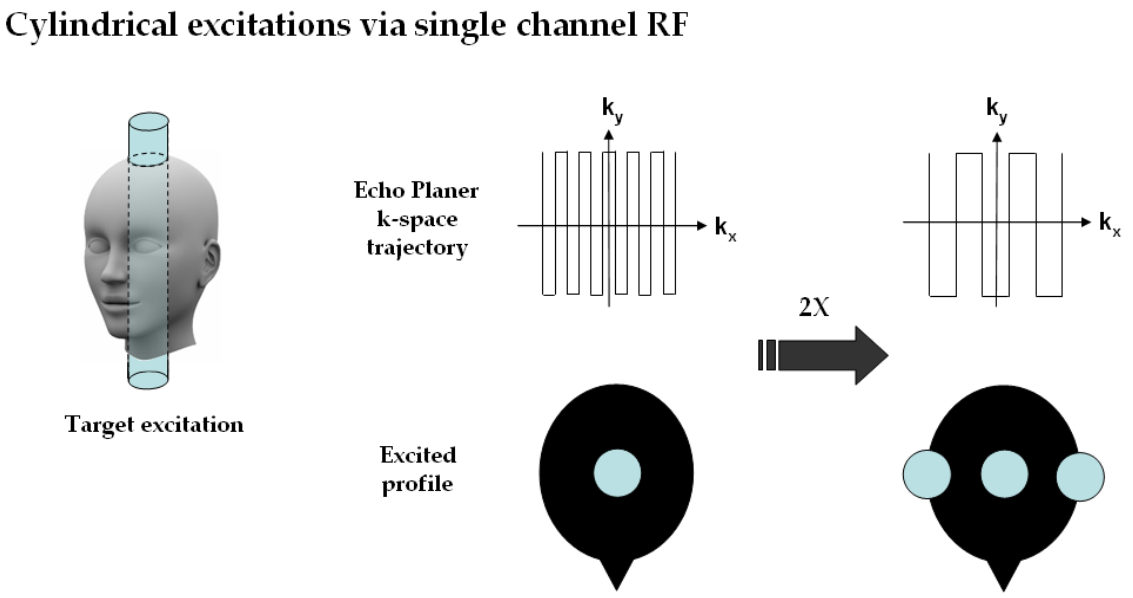

Figure 7: Cylindrical target excitation and the results of single-channel Echo Planer excitation with 2X acceleration leading to aliasing/wrap-around effect

[1] Field-of-view (FOV) is used to describing the image area that contains the object of interest.

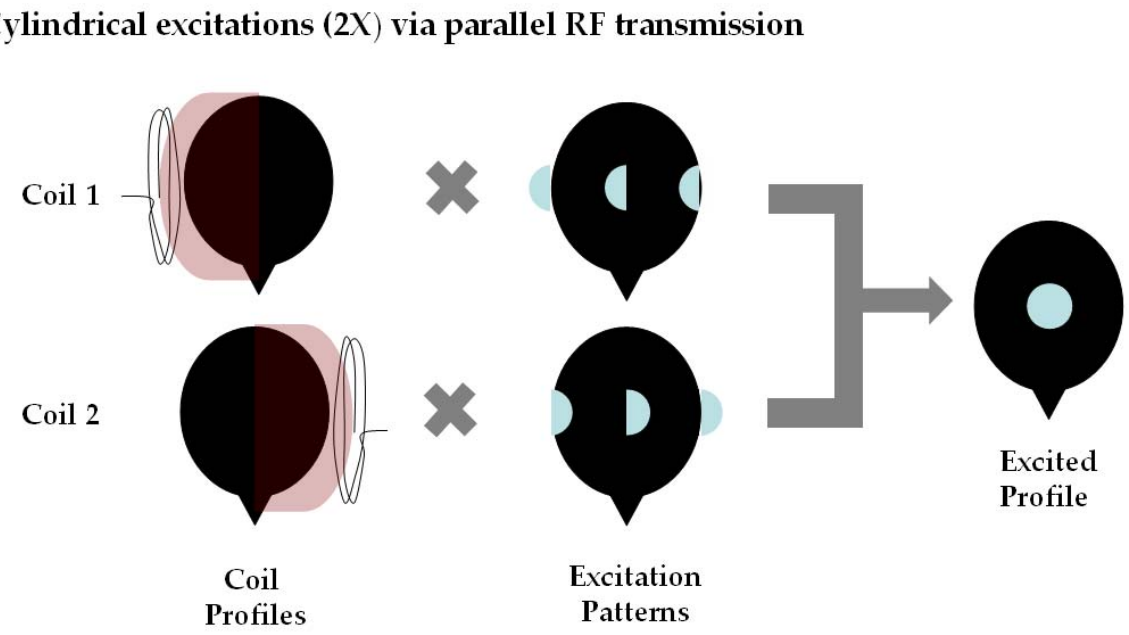

Figure 8: Cylindrical excitation (2X) via parallel transmission of two orthogonal RF coils resulting in no aliasing/wrap-around effect

This example gives an intuitive picture on how parallel transmission works. However, in reality the coil sensitivity profiles are not as well behaved, or as orthogonal, as the example assumes. They generally exhibit rapid spatial variation and are significantly overlapped. As a result the RF design process is more complex. The mathematical formulation below provides an outline of the actual design method used in parallel transmission.

Mathematical Formulation

Various methods have been proposed for parallel RF excitation design based on the small tip angle approximation presented earlier via Equation 2 and Equation 3. The use of this linear approximation greatly reduces computation and provides attractive intuition about design tradeoffs since the RF design problem is reduced to a linear, and in fact a Fourier system. In the method presented by Katscher et al. (8), the system of linear equations are solved in the excitation Fourier space, *k*-space. On the other hand, the scheme developed by Zhu (9) was formulated in the spatial domain with the

assumption of an echo-planar *k*-space trajectory. Another method proposed by Griswold et al. (10) draws on the "GRAPPA" technique (29) used in accelerating data acquisition with receive arrays, and is solved in the k-space domain. Finally, Grissom et al. (11) formulated the design as a direct discretization of the parallel small tip angle equation in space and time.

The small-tip-angle work in this thesis starts with Grissom's formulation as the baseline, where the parallel small-tip excitation approximation with *R* coils is written as

Equation 4

$$m_{xy}(\bar{r}) = i\gamma m_0 \sum_{c=1}^{C} S_c(\bar{r}) \int_0^T b_{1,c}(t) e^{i\bar{r}\cdot\bar{k}(t)} dt$$

This is a direct extension of Equation 2, where in this case the resulting magnetization is the sum of the magnetization produced from each of the coils. Furthermore, an extra term appears in this equation due to the coils' B_1^+ sensitivity profiles, $S_c(\bar{r})$. In the single coil case, the profile was assumed to be uniform in space, and hence its exclusion from Equation 2.

After discretization of space and time, this expression can be written as a matrix equation, $m = Ab$, where the *A*-matrix incorporates the B_1^+ coil profiles modulated by the Fourier kernel due to the k-space traversal, *m* is the target profile in space, and *b* contains the RF waveforms. With this formulation, the RF pulses can be designed by solving the following optimization problem by the conventional Least Squares (LS) algorithm:

Equation 5

$$b = \arg_b \min\{\|Ab - m\|_w^2 + R(b)\}$$

Here, the optimization is performed over the Region of Interest implied by a weighting, w, and $R(b)$ denotes a regularization term that may be use to control integrated and peak RF power. Generally the Tikhonov regularization ($R(b) = \beta b'b$) is used, and the minimization problem can be solved efficiently using conjugate-gradient (CG) methods.

Parallel Transmission's RF Coil Design and Mode Compression

One of the major requirements in parallel excitation is to have good orthogonality between RF coils transmission profiles to allow good acceleration performance. This is not easy to achieve due to the coupling effect between the RF coils. Generally, parallel transmission RF coil arrays are built around a cylindrical ring with a number of local coil elements placed adjacent to each other, with some means of decoupling them. Figure 9 shows some of the coil arrays that were used in this work. The loop array on the left (a) is decoupled via overlapping the coil elements, and the stripline arrays in (b) and (c) are decoupled via capacitive means (30,31).

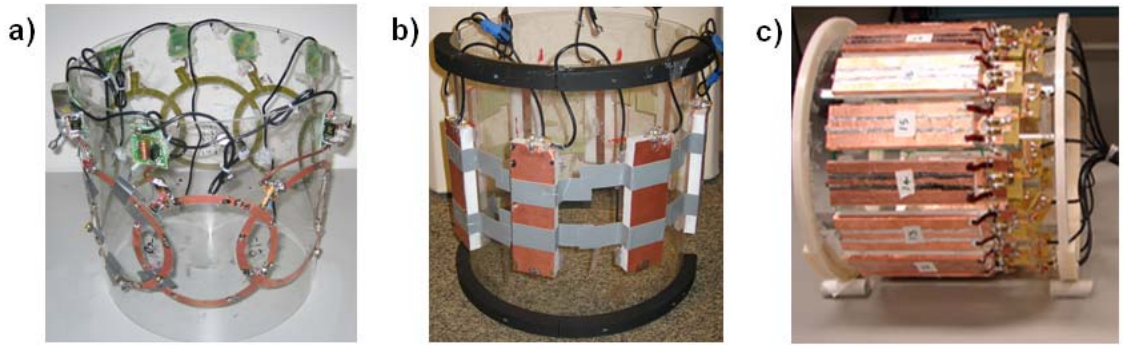

Figure 9: RF coil arrays employed in this work: (a) eight-channel loop coil array at 3T, (b) eight-channel stripline array at 7T, (c) sixteen-channel stripline array at 7T.

With more RF coil elements, higher transmission acceleration can be achieved. Nonetheless, as more elements are built into a coil array, the coil profiles of these elements become less orthogonal, resulting in a smaller achievable acceleration gain. Furthermore, for each additional transmission channel, an extra set of RF amplifier hardware is required. These hardware components are expensive and pose a practical limit on the number of transmission channels that can be used. To partially overcome this limitation, the idea of "mode compression" is employed, whereby orthogonal "modes" instead of the individual coil elements of the array are used for transmission to significantly reduce the number of transmission channels required (31). To understand this concept, first an explanation of a "mode" will be given, followed by an explanation on how it could be use to reduce the number of transmission channels.

The transmission profiles of the coil elements in an array can be thought of as a basis set which are not very orthogonal. Therefore, one should be able to apply a basis transformation to create an orthogonal basis set with a reduced number of bases. "Modes" of a coil array can be thought of as an orthogonal basis set. Many different types of modes exist. By constructing the coil array using the principle of *degenerate* birdcage coil design (31), the "birdcage" modes can be created from the array. To create each of these birdcage modes, RF transmission with the same amplitude but different phase are sent to the coil elements. For an N-channels array, the M^{th} mode is created by driving the coil elements C_1, C_2, C_3,…., C_N with the same amplitude but with a phase relationship of $0, M\frac{2\pi}{N}, M\frac{4\pi}{N}, ..., M(N-1)\frac{2\pi}{N}$. The profile of the first mode (M=1) generated by the *degenerated* birdcage coil is the same as the profile of the standard single channel birdcage coil that was previously described. In the standard birdcage coil, the coil elements are linked and are designed to have a mode-1 phase relationship when RF is transmitted into the single input channel of the coil. The profile produced by this mode is uniform[1] and is referred to as "uniform birdcage mode". The higher order modes have strong spatial variation and are not used in conventional imaging. For an N-channel coil, there are N possible birdcage modes; half of which do not provide significant excitation due to their counter-rotation property (31). Nonetheless, the N/2 remaining modes provide useful transmissions and have a high degree of orthogonality.

The mode compression idea is based on "butler matrix" hardware (31), which can generate the N/2 useful modes using N/2 instead of N sets of RF amplifier. Given the availability of N/2 RF amplifiers, the N/2 highly decoupled mode profiles generated by an N-channel array is much preferred over the profiles produced by an N/2-channel coil array driven directly though the RF amplifiers. When in use, the butler matrix hardware is placed between the coil and the RF amplifiers. Figure 10 shows a diagram of the butler matrix with N/2 inputs from the amplifiers and N outputs to the coil array's elements. The butler matrix splits the input power from the k^{th} amplifier and feeds it

[1] This is true at low B_0 field but is not valid at higher field

equally into each of the N output channels with appropriate phase shifts to generate the k^{th} birdcage mode of the array. In this work, an 8x16 butler matrix hardware (31) is used to drive the 16-channel stripline coil array shown in Figure 9c, on our 8-channel transmission system at 7T.

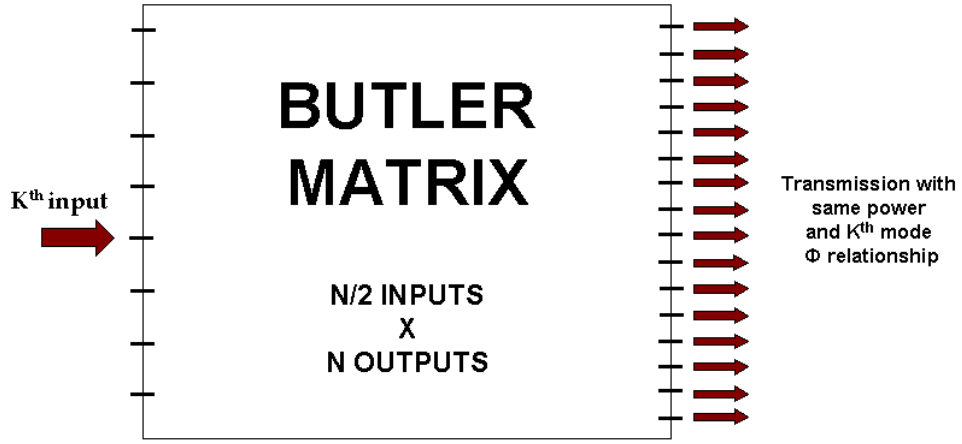

Figure 10: Diagram of the Butler matrix with N/2 inputs from the RF amplifiers and N outputs to the transmission coil elements. The power transmitted by the k^{th} amplifier is split into equal parts and feed to the output with appropriate phase shifts to generate the k^{th} birdcage mode.

As a side note, RF coil arrays are also widely employed for signal reception during the data acquisition phase of MRI. In the single channel reception case, signal received by the coil elements are usually designed to have a mode-1 phase relationship resulting in "uniform birdcage" reception. In multi-channel reception, parallel reception techniques (29,32,33), which were develop prior to parallel transmission, are used to accelerate data encoding. However, unlike parallel transmission, in parallel reception the receive hardware are relatively inexpensive (pre-amps instead of power amps), allowing for a large number of coil elements to be used, with a recently achieved coil array count of 128 (34,35).

B_1^+ mitigation via Parallel Transmission

As previously mentioned, the uniform birdcage RF field of a coil array is spatially inhomogeneous at high B_0 field. At high field strength, Larmor frequency

increases, causing a decrease in the RF field's wavelength. As the wavelength becomes comparable in size to the length of the object being scanned, destructive interference occurs between the RF fields of the various coil elements in the array. This destructive interference results in inhomogeneous RF field distribution which is relatively mild for head imaging at 3T but is very severe for body imaging at 3T (due to larger object's size) and head imaging at 7T (due to shorter wavelength).

Spatially tailored RF excitation can be used to mitigate transmit RF field inhomogeneity (B_1^+) by creating an excitation pattern which is the spatial inverse of the inhomogeneity. Figure 11 illustrates this for slice-selective excitation in the single channel RF setup. The inhomogeneous coil profile used in this example is taken from a head-size water phantom, imaged at 7T using the uniform birdcage mode of the 8-channel stripline array coil previously shown in Figure 9b). For slice-selective excitation along the z-axis, B_1^+ mitigation is required in the in-plane (x-y) direction. Figure 11a) shows a non-mitigated slice-selective excitation created by a standard sinc RF. With no in-plane excitation modulation, the excitation profile is very inhomogeneous. Figure 11b) shows the B_1^+ mitigated excitation created by using the k-space spoke trajectory described in section 1.2.1. As previously stated, the main intuition in designing k-space trajectories is in trying to come up with a fast trajectory path that will sufficiently cover the high energy region in k-space for the particular excitation. For B_1^+ mitigated slice-selective excitation, sharp selection, typically 1-cm or thinner, along the z-axis is required (i.e. large coverage in k_z is required), while at the same time a relatively slowly-varying in-plane mitigation patterns is needed across the object being scanned, which in this case is a water phantom with a 17-cm diameter (i.e. smaller coverage is required in k_x-k_y). Therefore, the required k-space coverage for this excitation is shaped like a rugby ball aligned along the z-axis. This rugby ball region can be cover in a time efficient manner via the use of the spoke trajectory shown in Figure 11b)

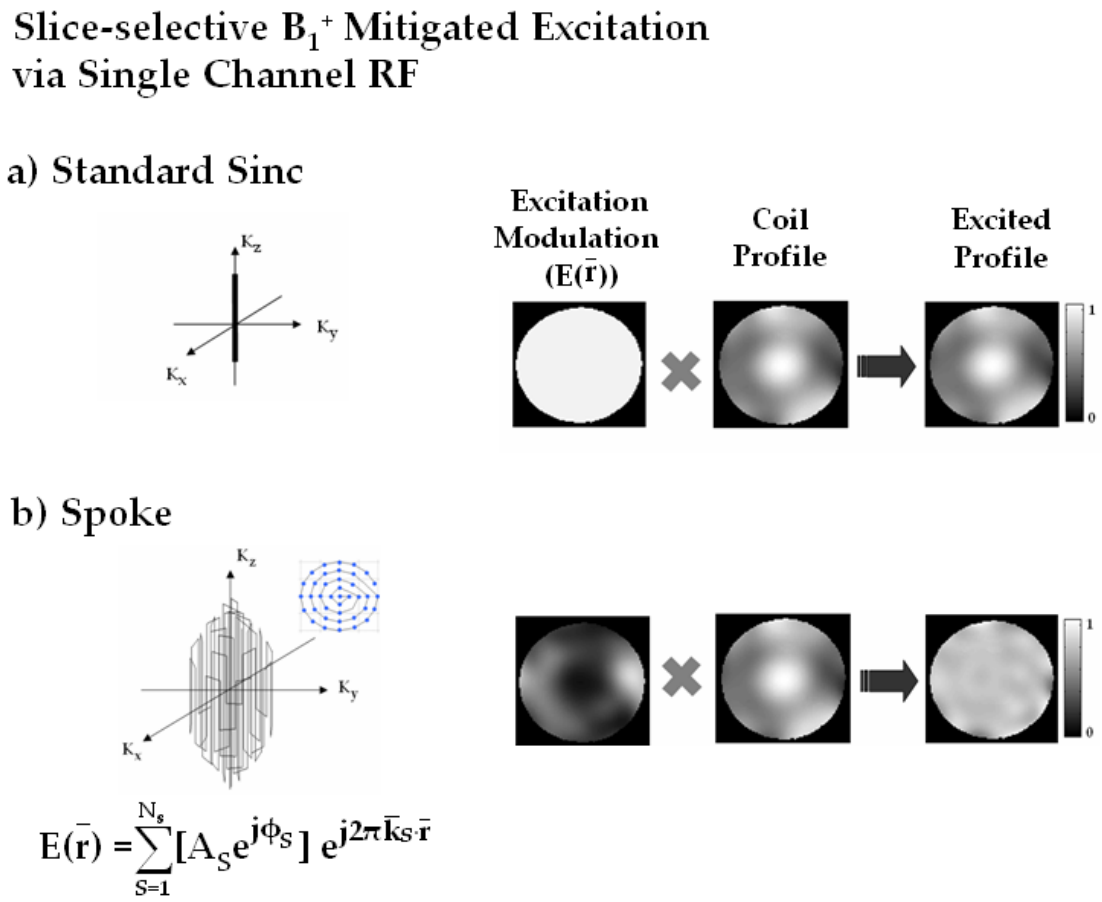

Figure 11: Slice-selective B1+ mitigated Excitation via single channel RF, **a)** Standard slice-selective sinc excitation with no in-plane modulation, resulting in large variation in the excited profile. b) Spoke excitation with sufficient in-plane modulation to correct for severe B1+ inhomogeneity.

With the spoke trajectory, slice-selection is achieved by depositing sinc-like RF along each k_z transversal or "k_z-spoke". For B_1^+ mitigation, the complex amplitude of these sinc-like RFs are tailored to provide the desired in-plane excitation modulation. According to Fourier theory, the in-plane modulation provided by a spoke at an in-plane location $\bar{k}_s$ with RF complex amplitude of $A_S e^{j\phi_S}$ is given by $[A_S e^{j\phi_S}]e^{j2\pi\bar{k}_S\cdot\bar{r}}$. Therefore, for an excitation trajectory with N_s spokes, the total in-plane modulation is

Equation 6

$$E(\bar{r}) = \sum_{S=1}^{N_S} [A_S e^{j\phi_S}] e^{j2\pi\bar{k}_S\cdot\bar{r}}$$

With this, the desired excitation modulation i.e. an inverse pattern of the inhomogeneity can be created by using a sufficiently large number of spokes and tailoring their complex amplitude accordingly. Figure 11b), shows the excitation modulation achieved via the use of 41 spokes. The modulation is sufficient in mitigating the in-plane B_1^+ inhomogeneity, resulting in a close to uniform excitation. However, because of the large number of spokes required, the duration of this excitation is too long for clinical use (~40 times longer than the standard sinc excitation).

Parallel excitation can be used to dramatically shorten the duration of the spoke excitation by reducing the required number of spokes. This is illustrated via an example in Figure 12, where the eight elements of the stripline array coil used previously, are now driven separately for parallel transmission. Previously, in the single channel case, the modulation provided by each spoke can be thought of as a basis that is used in forming the total mitigation modulation. In the example in Figure 11b) 41 spokes were required to provide adequate mitigation. Here, with parallel excitation, 8 spokes are used to provide 8 bases *per RF channel*, totaling up to 64 bases for the 8 RF channels setup[1]. With the use of these bases, a similar level of mitigation can be achieved[2] with a much shorter excitation duration compared to the single channel case. In addition, with the novel algorithm that will be presented in chapter 4, further reductions in the number of spokes can be achieved. Applying this algorithm to this example, superior mitigation performance can be achieved via the use of only 4 spokes.

[1] The bases in parallel transmission are formed by multiplying together the modulation provided by the spokes and the coil profiles. Since the coil profiles are already included as part of the bases, the bases are now used to form a uniform in-plane excitation profile rather than a mitigating modulation.

[2] More bases are required in parallel transmission (64 vs. 41), as the similarity between the coil profiles causes the bases in parallel transmission to be less orthogonal than the ones in the single channel transmission.

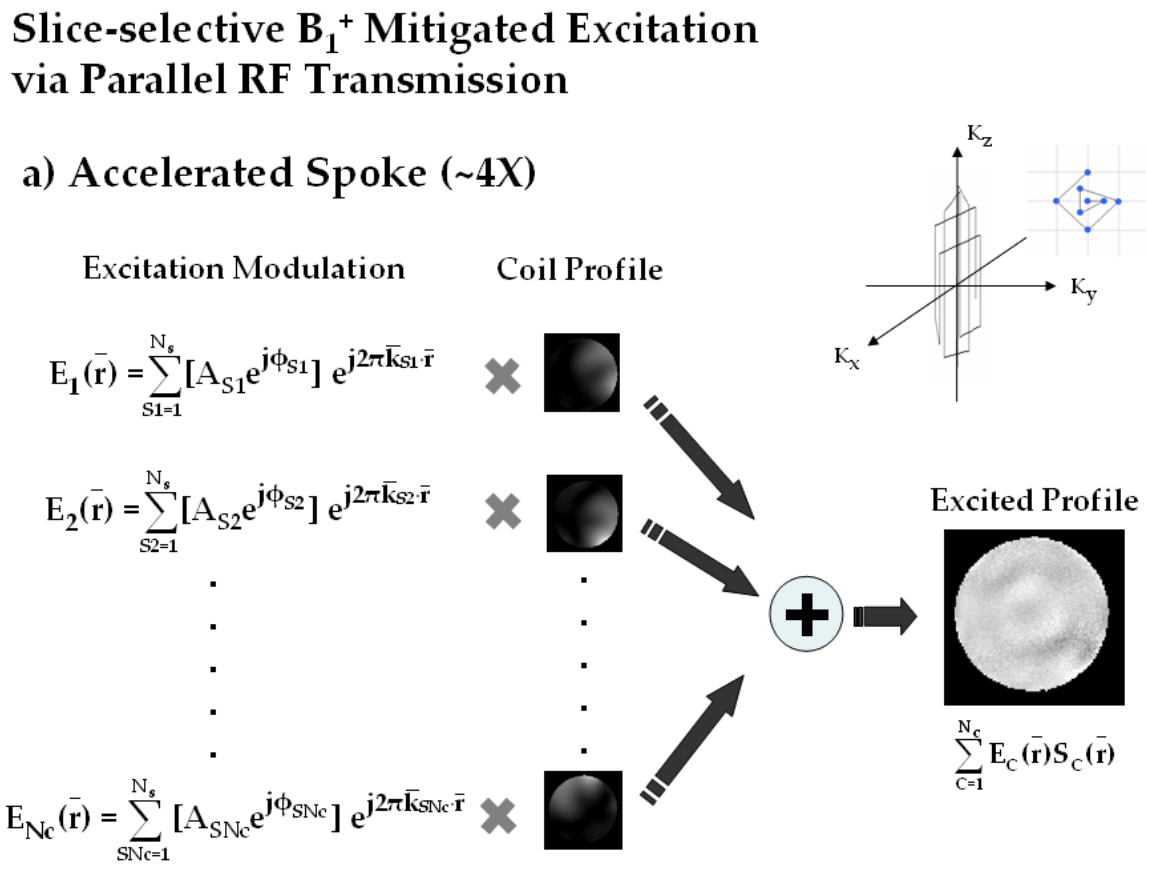

Figure 12: Acceleration of spoke trajectory via parallel excitation resulting in a significantly reduction in the number of required spokes, and hence excitation duration.

1.3 Imaging Schemes for Contrast Generation

In this section, elementary contrast generation mechanisms in MR are described and the imaging schemes that exploit these mechanisms are presented. Furthermore, to motivate the subsequence chapters, the harmful effect of B_1^+ inhomogeneity on these imaging schemes are discussed.

Contrast mechanisms

MRI offers excellent contrast between soft tissue structures and is often the preferred diagnostic imaging modality. This useful image contrast is achieved by using imaging sequences that accentuate the differences in MR physical parameters in different tissue

compartments. The physical parameters that are of importance are ρ, T_1, and T_2, where ρ represents the spin density which is proportional to the equilibrium sample magnetization (m_0), and T_1 and T_2 are the longitudinal-z and the transverse-xy relaxation time constants. These relaxation constants appear in the Bloch equation (Equation 1), and represent the relaxation of excited magnetization towards its equilibrium state along the positive z-axis. For example, when a 90° excitation is applied, the magnetization will exist solely in the transverse plane with no M_z component, and T_1 represents the rate at which M_z exponentially recovers, and T_2 represents the rate at which M_{xy} decays. T_1 and T_2 differ significantly between tissues, and are also altered in abnormal conditions such as in cancerous tissues.

Imaging Sequence

Careful design of imaging sequence parameters can accentuate structural differences between the relevant physical parameters of different tissues. Many types of sequences exist in MRI. Here, we will focus on the saturation-recovery sequence and its parameters (explanation adapted from (18)). For more information on other types of sequence please refer to (17,18).

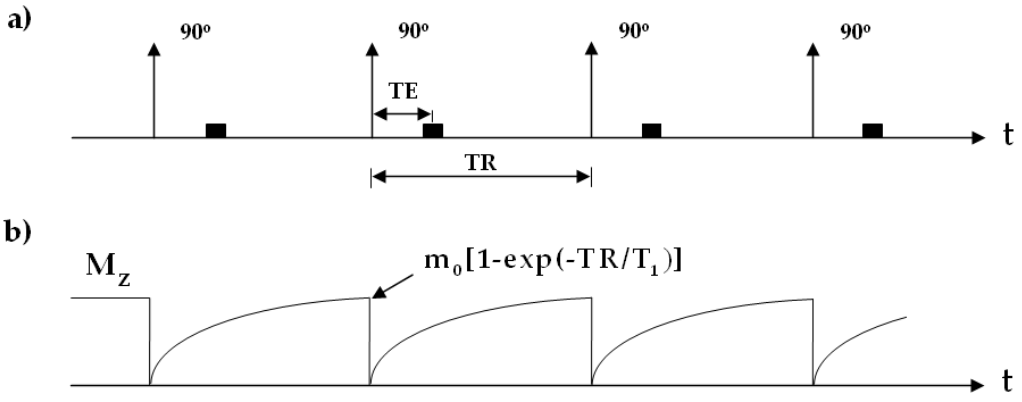

Figure 13: (a) Basic Saturation-Recovery Sequence: A string of 90° excitation pulses separated by repetition time TR, along with data acquisition (represented by the black blocks) after each excitation at the gradient echo time TE. (b) Time Course of Mz: Value of Mz prior to the 90° pulse determines the resultant signal generated. Figure adapted from (18).

The basic saturation recovery sequence is shown in Figure 13a, with a string of 90° excitation pulses separated by repetition time TR, and data acquisition (represented by the black blocks) after each excitations at the gradient echo time TE. As can be seen, the excitation and data acquisition are repeated together many times to acquire enough data to create an image. In the sequence, the 90° excitation rotates the M_z magnetization into the transverse (xy) plane, producing a signal dependent on the size of M_z prior to the excitation. After this excitation, M_z is allows to re-grows during the TR interval prior to the next excitation. The amount of M_z re-growth is governed by the Bloch equation (Equation 1) and is given by $m_0[1-e^{-TR/T_1}]$. The sequence's name "saturation recovery" stems from the *saturation* of the M_z component (to zero) by the 90° pulse, and the subsequently *recovery* of the M_z over the TR interval. Figure 13b illustrates the time course of M_z, where the value of M_z prior to the 90° pulse determines the signal strength during the data acquisition which in turn determines the image intensity, $I(\bar{r})$, which is given by

Equation 7

$$I(\bar{r}) = K\rho(\bar{r})[1-e^{-TR/T_1(\bar{r})}]e^{-TE/T_2^*(\bar{r})}$$

Here, K is a catch-all gain constant, $\rho \propto m_0$, and $e^{-TE/T_2^*(\bar{r})}$ represents the signal decay prior to data acquisition.

To achieve pure T_1 contrast in an image (T_1 weighted), the data acquisition is performed straight after the excitation (TE = 0), resulting in an image intensity of

Equation 8

$$I(\bar{r}) = K\rho(\bar{r})[1-e^{-TR/T_1(\bar{r})}]$$

TR is normally set to be approximately equal to T_1 to highlight T_1 differences.

For pure T_2 contrast, modification is required to the sequence. First, note the use of T_2^* instead of the T_2 in Equation 7. The decay of the transverse component of the magnetization, as represented by T_2, generally has only minor contributions to the

overall signal decay. The T_2^* encompassed this along with a much larger effect of intra-voxel dephasing described by Figure 14(a)-(c). Recall that the dipole moments contributing to M each rotate at a rate proportional to the magnetic field they experience (Larmor frequency). For in vivo application, the differences in susceptibility of various tissues in the body, such as in the air-tissue interface in the sinuses, can lead to variation in magnetic field experienced by the protons within a single volume element (voxel). Therefore, with time the phase coherence present immediately after the 90° pulse (Figure 14 (b)) will gradually be lost as the dipole moments rotate in the transverse plane at slightly different frequency (Figure 14(c)). This phase incoherent wills results in signal loss as the signal from the dipole moments are summed up across the voxel. To recover this signal loss, the spin echo technique (36) is used (Figure 14). At time τ after the 90° excitation, a pulse which rotates the magnetizations around the x-axis by 180° is applied, causing the phase dispersion to reverse (Figure 14(d)). Since the rotational frequency of the magnetizations are still the same, the phase dispersion produce during period τ after the application of the 180° pulse will perfectly cancels with that of the neglected phase dispersion (Figure 14 (e)). Therefore, phase coherence is achieved at $t = 2\tau$ after the 90° excitation. The modified saturation-recovery sequence with the spin echo is shown in Figure 15, where the expression for image intensity becomes

Equation 9

$$I(\bar{r}) = K\rho(\bar{r})[1-e^{-TR/T_1(\bar{r})}]e^{-TE/T_2(\bar{r})}$$

For T_2 weighted image, TR is set to be long to avoid T_1 contrast and TE is set to be approximately equal to T_2 to highlight T_2 differences.

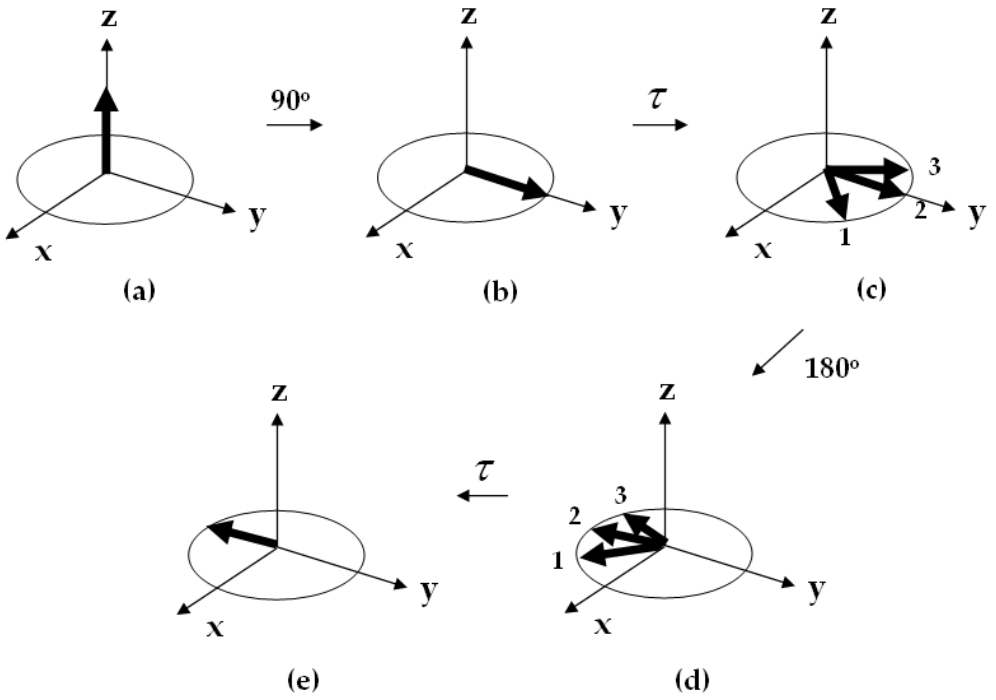

Figure 14: Spin Echo Generation: After the 90° excitation (a)-(b), due to local field variation the transverse magnetization of the dipole moments rotate at slightly different frequency resulting in phase dispersion (c). The phase dispersion is negated with a 180° pulse applied along the x-axis (d), causing the dipole moments to rephrase after time τ . Figure adapted from (18).

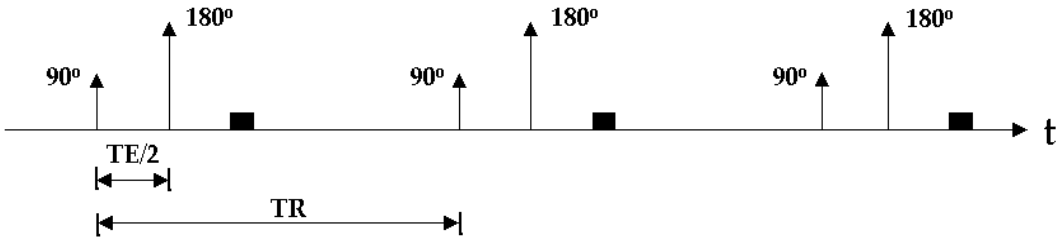

Figure 15: Saturation-Recovery Sequence with Spin Echoes. Figure adapted from (18).

General Excitation-Recovery

The general excitation-recovery sequence is a generalization of the saturation recovery sequence; with a general θ pulse replacing the 90° pulse in Figure 13. In the saturation recovery sequence, M_z is saturate to zero after each excitation and is allowed a period of t = TR to re-grow before the next excitation. Since the signal generated by the excitation

depends on both the flip angle of the excitation and the available M_z prior to excitation, the maximum signal will not always achieved via the use of the 90° pulse. In cases where short TR is used and signal recovery period is small, it is much more efficient to use a tip angle of much less than 90°. With a tip angle of less than 90°, M_z does not get reset to zero after each excitation and therefore steady-state condition does not occur immediately. In (18), expressions for the steady-state M_z is derived, resulting in the following image intensity expression (assuming TE~ 0)

Equation 10

$$I(\bar{r}) = K\rho(\bar{r})\frac{[1-e^{-TR/T_1(\bar{r})}]\sin\theta}{1-e^{-TR/T_1(\bar{r})}\cos\theta}$$

For a fixed TR & T_1, the tip angle that maximizes this expression is given by

Equation 11

$$\theta_E = \cos^{-1}(e^{-TR/T_1})$$

This optimum angle, θ_E ,is referred to as the Ernst angle.

Effect of B_1^+ inhomogeneity on Contrast

B_1^+ inhomogeneity at high B_0 field causes spatial variation in flip angle during excitation. For basic saturation-recovery sequence, the flip angle of 90° will not be achieved simultaneously at all spatial locations, and hence the image intensity will not be governed by Equation 8, but by Equation 10, with the flip angle, θ, now being a function of space. Based on Equation 10, the image's T_1 contrast, dI/dT_1, will exhibit a non-linear relationship with $\theta(\bar{r})$, resulting in significant *contrast* inhomogeneity (not simply intensity shading) in the image, which can not be removed via post processing. This image contrast inhomogeneity issue is even more prominent in the spin-echo based saturation-recovery sequence, where spatially varying flip angle exist in both the 90° and 180° pulses.

In this thesis, we propose the use of spatially tailored excitation pulses with parallel transmission to mitigate the flip angle variation and correct for this inhomogeneous contrast. The algorithms presented in Chapters 2 and 4 provide the design solution that is applicable in the small tip angle domain, and can be used in the general excitation-recovery sequence. The design in Chapter 6, provides extension to these designs and allows for selective excitation of certain brain metabolites, important in the detection of neuro-degenerative diseases. In Chapter 7, a design method is presented for the excitation in the large tip angle regime, leading to B_1^+ inhomogeneity mitigated 90° and 180° excitations, which can be used in the spin-echo based saturation-recovery sequence.

As a side note, the receive profile of the receiver coils are termed B_1^- and also exhibit spatial inhomogeneity at high B_0 field. However, this only causes variation in image intensity and SNR, but not contrast. Although the SNR loss is often very important, this variation is not as harmful and can indeed be removed via a point by point division of the image by the B_1^- profile. Still, this correction method results in spatially varying SNR.

Chapter 2

Parallel RF Transmission at 3 Tesla

In this chapter, the research findings at 3 Tesla are reported. The first part of this chapter covers the implementation of parallel transmission design on a prototype 8-channels RF system for an oil phantom. The second part of this chapter describes the work which provides what the author believes to be the first demonstration of parallel RF excitation for in vivo human application. In this work, it was shown that B_0 (main field) inhomogeneity observed in standard in vivo imaging can have a detrimental effect on parallel RF excitation and should be accounted for during the pulse design.

2.1 Phantom experiments

2.1.1 Introduction

Prior to the undertaking of this research, several authors have demonstrated the concept of parallel RF by exciting with a single coil at a time, and combining the received data with off-line post-processing to simulate parallel excitation (8,9,37-39). Furthermore, a 4-channel realization of parallel excitation was performed by Ullman et al (12) who demonstrated the feasibility of acceleration of parallel excitation by a factors of 2 and 2.67 using a 2D spiral k-space trajectory, with the design based on Grissom's formulation (40).

Here, we describe the design and implementation of parallel RF excitation on a 3T human MRI scanner with a dedicated 8-channel transmit array, using Grissom's

design formulation. Two types of excitation k-space trajectories were used for the design of the parallel RF pulses, a 2D spiral excitation with integer acceleration factors between 2 and 8, and a 3D spoke excitation. The 2D pulse excited a high-resolution spatial pattern in-plane, while the 3D trajectory produced high-quality slice selection with a uniform in-plane excitation in spite of the highly non-uniform individual spatial profiles of the coil array. This work provides a feasibility study of the usefulness of parallel excitation for correction of B_1^+ magnetic field inhomogeneity, and for reduction of excitation time in exciting specifically shaped volumes.

2.1.2 Methods

System Hardware and RF Coil Array

The 8-channel system was configured around a modified Siemens 3T Tim Trio scanner (Siemens Medical Solutions, Erlangen Germany) with gradient amplitude limit at 40 mT/m (for G_x, G_y) and 45 mT/m (for G_z), and slew rate limit at 200 T/m/s. Eight sets of the RF waveform and gradient generation hardware were configured in a master and slave setup. A single master channel synchronized the waveforms of each of the 7 slave transmit systems. Each of the RF transmit channels utilize an independent 8kW broadband solid-state power amplifier (Dressler, Germany).

For the RF coil array, eight circular, 15-cm diameter, detunable surface RF coil TR elements were tuned to the Larmor frequency at 3T with 8 distributed capacitors and placed on the outer surface of a 28-cm diameter acrylic tube. The coils were overlapped to null mutual inductance between nearest neighbors. All measurements were performed in a 17cm diameter low-dielectric oil phantom inside a cylindrical loading ring. The setup is illustrated in Figure 16.

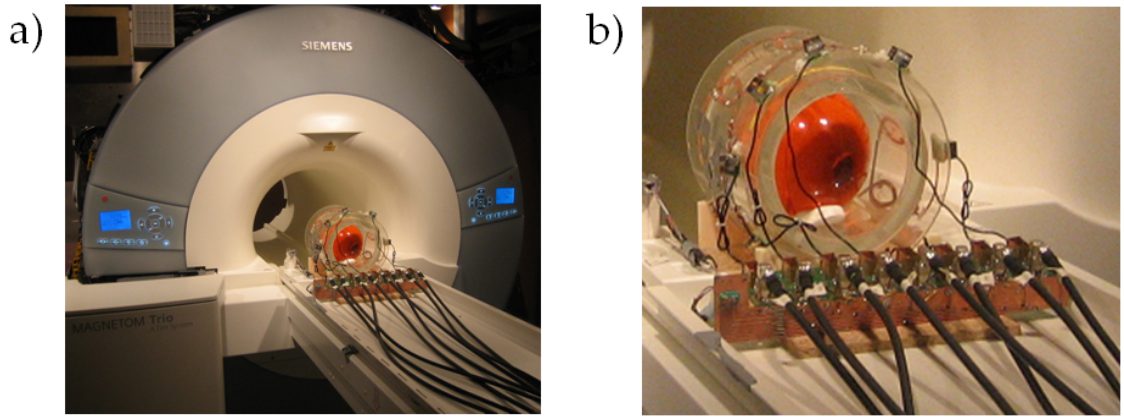

Figure 16: a) Siemens 3T parallel transmission scanner. b) Eight-channel coil array. Each coil has 17 cm diameter, and placed in an overlapping pattern on an acrylic cylinder with a 28 cm diameter. Centered in the coil is a 17-cm diameter oil-filled spherical phantom that was used for evaluation of the parallel RF excitation designs.

Parallel Excitation RF Design

Two types of gradient trajectories were used, a 2D excitation *k*-space sampling with spirals in (k_x,k_y) to excite a high-resolution spatial pattern of letters in the (x,y)-plane, and a set of "spokes" in k_z, regularly sampling the (k_x,k_y)-plane (22,27,28,41) to achieve sharp slice-selection in *z*, but with low-resolution control of the in-plane, (x,y), magnetization profile.

Spiral Trajectory A two-dimensional *k*-space trajectory was designed to sample excitation *k*-space for a high-resolution spatial pattern given by the MIT logo target profile presented in Chapter 1. The resolution for the design was set at 5 mm[1], field-of-view (FOV) at 18 cm[2], and undersampled spiral trajectories were calculated for accelerations of integer factors of 2 through 8 by successively increasing separation between the turns in the *k*-space trajectory. The design made use of routines made publicly available by Prof. B. Hargreaves (http://www-mrsrl.stanford.edu/~brian/mritools.html),

[1] From Fourier relationship, spatial resolution of the excitation is determined by the extend of the k-space trajectory ($res_{xy} = 1/(2k_{xy\max})$)

[2] The excitation FOV is determines by k-space sampling rate of the excitation k-space trajectory ($FOVxy = 1/\Delta_{kxy}$)

and operated with gradient amplitude of 35 mT/m and the slew rate of 150 T/m/s. The duration of the unaccelerated (1X) trajectory was 9.47ms, and for two-fold (2X) through 8X acceleration it was 4.76ms, 3.2ms, 2.42ms, 1.95ms, 1.64ms, 1.42ms, and 1.26ms (Figure 17).

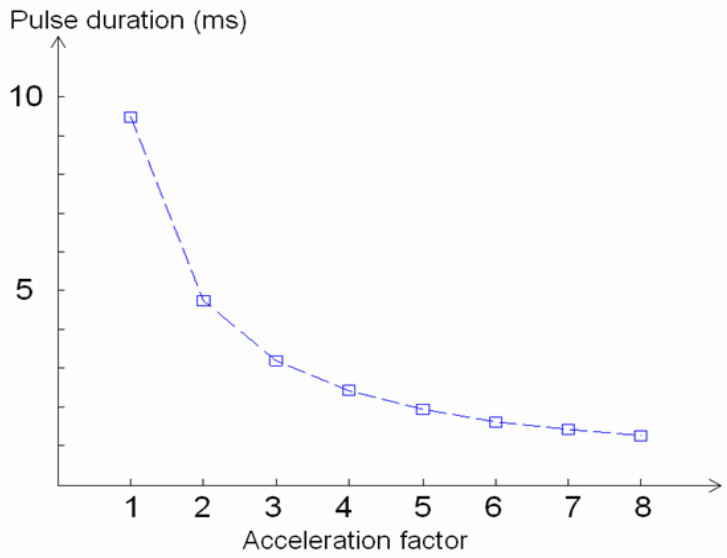

Figure 17: Duration of RF pulse design for the high-resolution in-plane excitation design as a function of acceleration factor.

Spokes Trajectory The slice-selective trajectory consisted of several spokes in k_z, separated in (k_x,k_y) with spacing that corresponds to a field of view (FOV) of 18 cm. Two versions of these trajectories were designed and tested, one with 4 spokes and the other with 7 (Figure 18), where the primary tradeoff is between more spokes allowing more control over in-plane modulation of the magnetization profile, but at the cost of increased pulse length and sensitivity to off-resonance effects. Slice thickness was 5 mm, and time-bandwidth-product equal to 4 for the center spoke in k_z. The same specifications for gradient amplitude and slew rate were used as for the spiral design. For the 4 spokes design, the pulse length was 3.42 ms. The extent in k_z of the non-DC spokes was half that of the center spoke, with the goal of minimum duration pulse while still achieving a flat target profile and sharp slice selection. The 7-spoke version was

designed to accommodate faster variation of the in-plane profile achieve sharper slice selection. It was 5.67 ms long with side spokes extent of 0.7 relative to the center one.

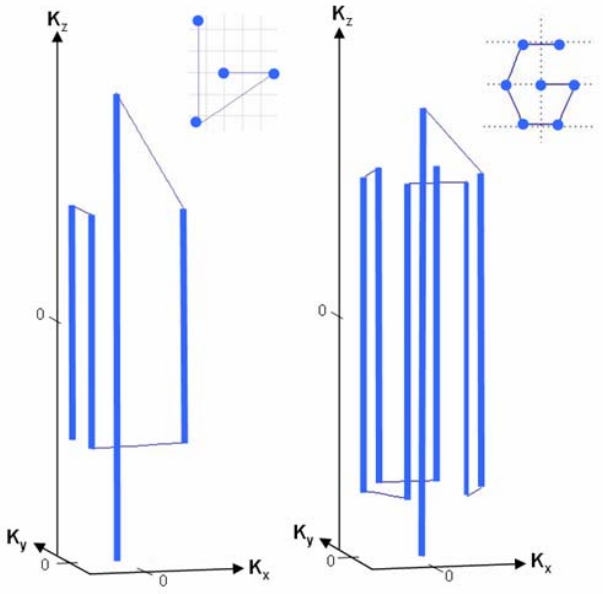

Figure 18: k-space trajectory for the 4 spokes design (left) and for the 7 spokes design (right)

Computation

The RF design method was based on singular value decomposition of the design matrix *A*, in the discretized version of Equation 4, $m = Ab$. With our set up of 8 transmission coils, the size of the *A*-matrix that needs to be decomposed in the solution of $m = Ab$, varies with acceleration factor, becoming larger with longer pulse lengths.

Matlab (Mathworks, MA, USA) was used for computation, which had a limit of maximum memory of 2 GB for each process. To restrict the size of the *A*-matrix and make the calculation feasible for all acceleration factors in the spiral design, a 4-mm spatial resolution of the B1 maps and of the target profile were used. Further, a 5-μs sampling of the desired RF waveform was employed, which is adequate to avoid angular-direction aliasing along the spiral *k*-space path. With these settings, the resulting *A*-matrix sizes were approximately 1500x15000 complex-valued floating point values for the 1X design, and 1500x2000 points for the 8X design. The decomposition calculation

took less than 15 minutes for 1X, and less than 2 minutes for 8X acceleration using a 3 GHz Pentium Linux workstation.

In designing the spokes trajectory, we made use of the property that the profiles of the coils do not differ much from each other along the z-direction, and therefore we did not expect to achieve any acceleration in this direction. Thus, to simplify the design, we restricted the RF pulse shape of all coils to a Hanning-windowed sinc in k_z, and consequently we only needed to calculate the amplitude and phase that modulated each of the sinc spokes. This procedure provided considerable reduction in the size of the *A*-matrix, and thus calculation time and memory requirements, enabling the use of a full-resolution B_1^+ map (2-mm in-plane) for this design. With these specifications, the resulting *A*-matrix sizes were approximately 3000x32 complex-valued floats for the 4-spoke version, and 1500x56 points for the 7-spoke design.

Simulation of Magnetization Profiles

Simulation of the resulting profiles was calculated by time discretization of the Bloch equation using spin-domain representation of Cayley-Klein parameters (42). In our procedure, the B_1^+ fields from all the coils were added before the Bloch equation calculation was performed. We note that although at low flip angle, where Equation 4 holds, this method of simulation should be equivalent to summing up the spatial magnetization profiles created by the RF waveforms from each coil, it is possible for the profiles created by some of the individual coils to reach the high flip domain while the desired profile is in the low flip domain. In this case the simulation based on summing up the profiles of the coils will be inaccurate.

The simulation also incorporated a simple B_0 off-resonance effect, i.e. the case where the main magnetic field value is slightly off because of tuning error or field drift over time, resulting in an offset in the Larmor frequency.

The agreement between the 2D spiral simulations and acquired data were quantified with a correlation coefficient, $R = Cov(sim, data)/(\sigma_{sim}\sigma_{data})$, where

Cov(sim,data) is the covariance between simulation and data, calculated on magnitude maps within the phantom boundary, and σ stands for standard deviation, calculated over the same spatial domain. For the 3D spokes excitation, the deviation of experimental data from the target profile was measured by maximum deviation, in percent, from the flat target value.

B_1^+ Shimming Simulation

To provide a comparison for the spoke trajectories with other B_1^+ inhomogeneity mitigation techniques, standard slice-selective and RF shimming[1] (43-45) excitations were simulated based on the measured coil maps. In the standard slice-selective excitation, identical slice-selective sinc RF pulses were used for transmission in all coils. In the RF shimming excitation, the same sinc RF pulses were employed, but with a modulation of the overall amplitude and phase of the pulse for each channel. The optimum amplitude and phase values were calculated based on the method used for the general spoke excitation, where the RF shimming was viewed as a single spoke at the origin of excitation *k*-space. With this method, the mean square error between the actual and the desired flat profile was minimized.

Imaging Parameters

B_1^+ Maps: Excitation B_1^+ profiles were obtained by applying a nonselective, low flip angle RF pulse to a single transmission channel at a time, and receiving through the uniform body coil, with repeated application for all eight channels. The subsequence reconstructed image obtained from each RF coil excitation represents the product of the transmit B_1^+ sensitivity profile of that particular coil and the receive B_1^- sensitivity profile of the body coil. Since the body coil's receive profile exhibits a spatial variation of <5%

[1] RF shimming is a technique that has been widely used in mitigating B_1^+ inhomogeneity. The technique relies on the ability to control the overall amplitude and phase of the RF pulse that is being applied to each of the coil elements in the array. Unlike parallel transmission, with this technique, only the overall amplitude and phase and not the shape of the RF pulse are allowed to vary from coil to coil. For slice-selective excitation, a sinc pulse with different amplitude and phase is applied to each coil.

across the oil phantom, the image provides a good approximation to the transmit B_1^+ profile of the RF coil. A standard 3D imaging sequence (gradient-recalled echo) was used to obtain this image, with the following imaging parameters: 128 x 128 x 64 pixels in x, y, z at 2 x 2 x 4 mm resolution (TR/TE/BW = 20 ms, 6 ms, 400 Hz/pixel)

The resulting B_1^+ maps were averaged down to 4-mm isotropic resolution for application in the 2D RF pulse design to reduce computation time and memory requirements.

Parallel Excitation: For each of the parallel excitation designs, the 8-channel array was driven with eight independent channels modulated in magnitude and phase by the calculated waveforms, and data received on the system body coil. The transmit voltage was set at a very low level (8V), to maintain flip angles to within the low flip angle assumption. The RF pulses were scaled so that their normalized maximum value was 1.0, and the excitation was then driven at a constant voltage on the scanner.

The imaging sequence used for B_1^+ mapping was again employed here to determine the resulting excitation profiles. For the 2D excitation pulse design, 18 image acquisitions were acquired and averaged for improved SNR since an extremely low transmits amplitude was used to insure that the low flip angle approximation was valid. Further, the four center slices have essentially no variation of signal in z, and were averaged together for the final result. The data for the 4-spokes excitation were averaged 24 times, while the 7-spokes data have four magnitude averages. For both spokes designs, the two center slices at full signal level were averaged in magnitude mode for the evaluation of the in-plane profile. The multiple averages were necessary to achieve sufficient SNR of the low flip angle excitations, and allowed reception with body RF system coil, which has low sensitivity but is spatially very uniform.

2.1.3 Results

B_1^+ maps

Figure 19 shows the magnitude and phase maps for the 8 transmit coils as measured by transmitting on each coil individually and receiving with the body coil. The magnitude profiles show some degree of coupling between neighboring coils, and also depict the strong magnitude decay of the profiles towards the center of the phantom.

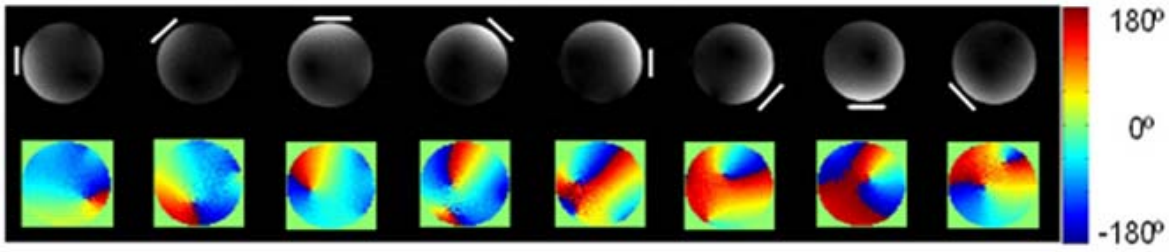

Figure 19: Magnitude (top) and Phase (bottom) of the Coil Profiles. Coil 1 is on the left, coil 2 is at 45º clockwise to coil 1, and so on for each of the 8 coils.

Spiral Trajectory

Figure 20a) shows the results of acquisitions and simulations for the 2D spiral trajectory for unaccelerated and 2-8 fold accelerated designs. For the region within the logo letters, the data display good agreement between experimental results (left) and simulations based on the acquired B_1^+ maps incorporating off-resonance effects (right), while the edges of the phantom are more visible in the acquired data than the simulation.

Figure 20b) shows correlation coefficients among acquired, simulation, and target profile as a function of acceleration factor for the 2D excitation. The black curve shows correlation as a function of acceleration factor between target and simulation, assuming zero off-resonance effects. This correlation is high (>.88) up to acceleration of 4X, and then lower for 5X-8X, but still above .79 for 8X. The red curve shows the target vs. simulation when off resonance effects are taken into account. In this case, the 1X and

2X designs are clearly sensitive to the off resonance as demonstrated by reduced correlation coefficient, but the 3X and 4X designs are more robust, thus the peak in the correlation for the red curve at a 4-fold acceleration.

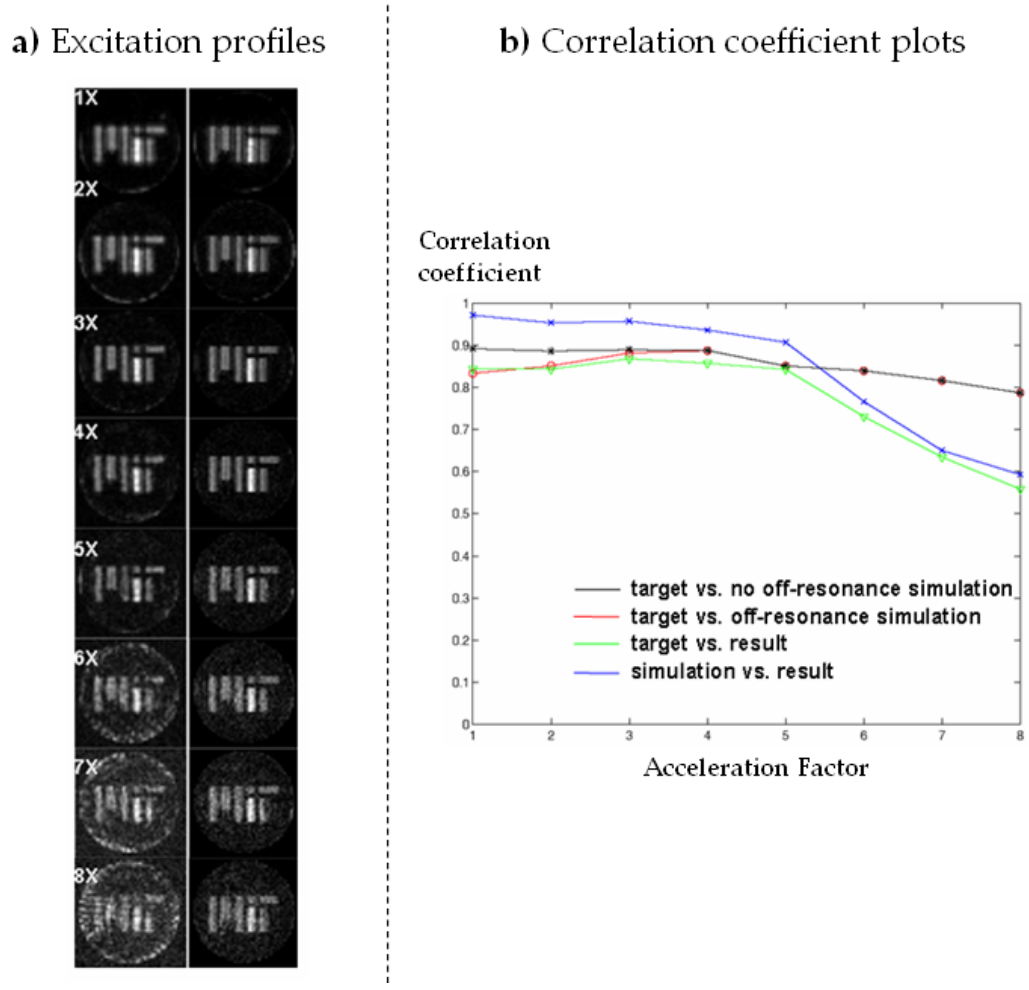

Figure 20: a) Magnitude of 2D excitation with 1X through 8X acceleration. Experimental data are shown on the left, and simulations on the right based on the measured B_1^+ maps. b) Plot of correlation coefficients among acquired, simulation, and target profile as a function of acceleration factor for the 2D excitation.

On the same figure, the green curve shows the correlation coefficient between target and results. This follows the target-vs.-simulation curve quite well up to 5X, but then this correlation decreases. Possible explanations are: *i*) at higher acceleration, more accurate cancellation is required to make up for the spatially aliased excitations from individual coils and a higher spatial resolution coil profile maps is needed to reproduce

the desired cancellation with better accuracy; or, *ii*) at higher acceleration, the SNR decreases Figure 20a). This is due to reduced overall flip angle in the accelerated excitations. The waveforms at high acceleration had higher peak power relative to average power and the waveforms were normalized in such a way that with fixed excitation voltage, the average power at the higher acceleration was smaller than for unaccelerated designs.

Finally, the blue curve shows the correlation coefficient between simulations and results. This correlation is higher than 0.9 up to 5X acceleration, but then decline at higher accelerations, approximately following the target-vs.-results curve.

Overall, the magnitude images demonstrate a very good match between predictions and simulations and similar concordance was found to exist for phase data as demonstrated in Figure 21. In this figure the measured phase (left) is compared to the simulated one (right), and the agreement is excellent in regions where the magnitude of the excitation exceeds the noise level (i.e. within the logo letters).

Figure 21: Phase of 2D excitation design for 4X acceleration, acquired data on the left, simulation on the right.

Figure 22 shows the experimental data demonstrating the effect of missing channels for 4X acceleration (left). Also shown in the figure are the simulated results of the profiles created by each coil (right). From these results, it is clear that all channels play a critical role to a successful constructive combination of signals and cancellation of aliasing artifacts.

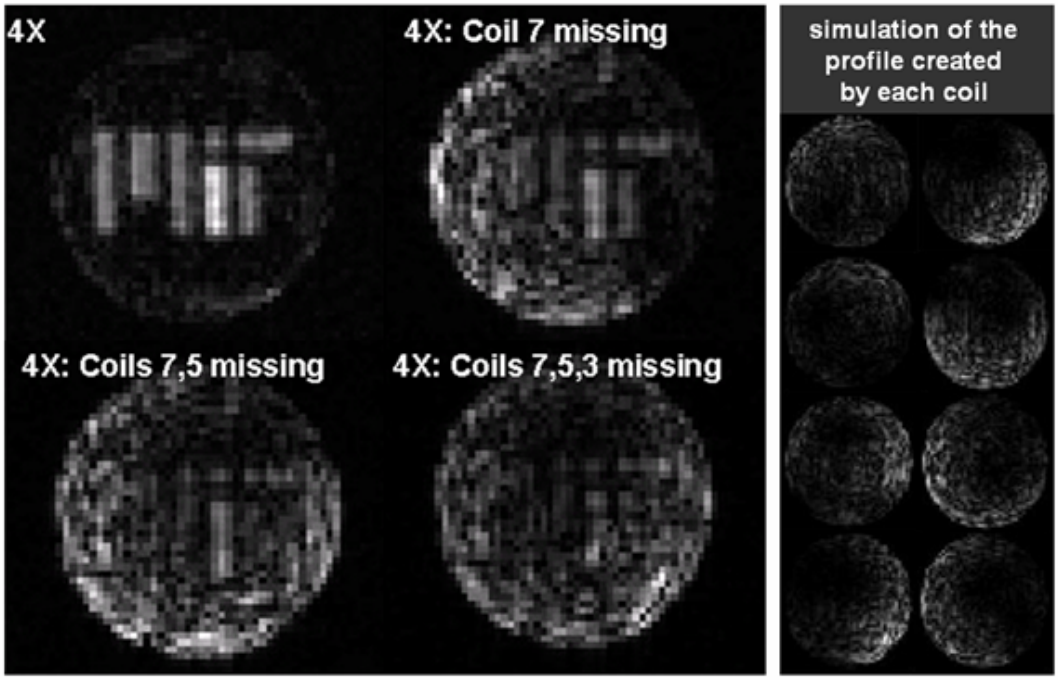

Figure 22: Experimental results, for the 2D excitation at 4X acceleration with missing channel(s) are shown on the left. Even with one channel missing severe artifacts are apparent. Also depict are the simulation of the profiles that would have been created by each coil in this experiment.

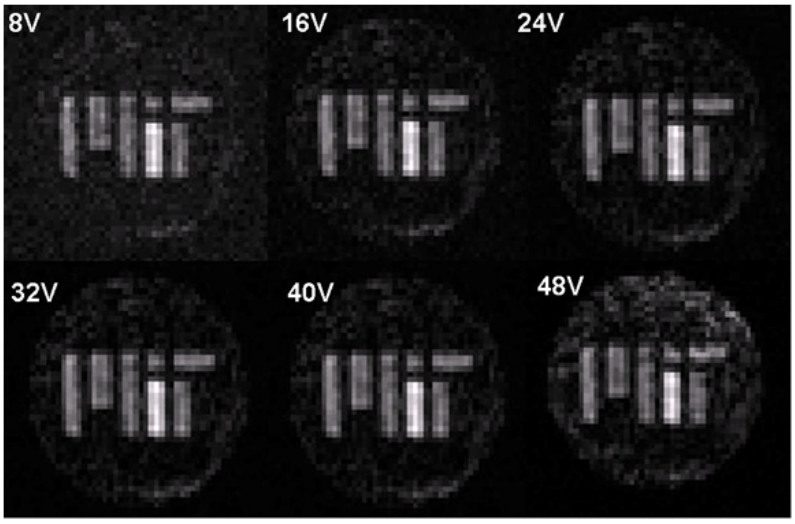

Figure 23: Increased excitation voltage for a 4X acceleration design with 2D excitation demonstrates the increased SNR with higher voltage, but at the same time, increased the cancellation artifacts in the background of the spherical phantom due to violation of the small tip angle approximation.

The effect of increased transmission voltage beyond the small-tip-angle domain is shown in Figure 23. The tradeoff of higher SNR with increased voltage vs. the increased level of cancellation artifacts in the background within the phantom is quite apparent.

Spoke Trajectory

Excitation with the 4-spoke 3D pulse, designed with a flat target profile and a 0.5 cm thick slice, along with a simulated profile based on the measured B1 field maps are shown in Figure 24 (left). Good slice selection is observed, while the in-plane profile shows a slight degradation compared to the simulation. To quantify the in-plane performance of this excitation, we note that 87% of the data deviate by less than 10% from the flat target profile, whereas 95% deviate by less than 20%. In the profiles along lines through the phantom (A-F), the largest deviation occurs in line E, with a deviation of ~34%.

Excitation with the 7-spoke design shown in Figure 24 (right) displays good agreement between measured and predicted profile except for the deviation near the 6-o'clock position. For instance, 85% of the data deviate by less than 10% from the target profile, whereas 93% deviate by less than 20%. In the line profiles, the resulting data are essentially flat except for line F near the bottom of the phantom, where the largest deviation is ~28%.

For comparison, standard slice-selective and RF shimming excitations were simulated based on the measured coil maps. The simulation results are shown in Figure 25, and reveal, as expected, a large in-plane inhomogeneity for the standard slice selection and a considerable improvement when RF shimming is applied. However, the residual B_1 inhomogeneity with the single-spoke RF shimming is still significant, as only 66% of the simulated profile fall within a 10% deviation from the target profile, and 81% deviate by less than 20%.

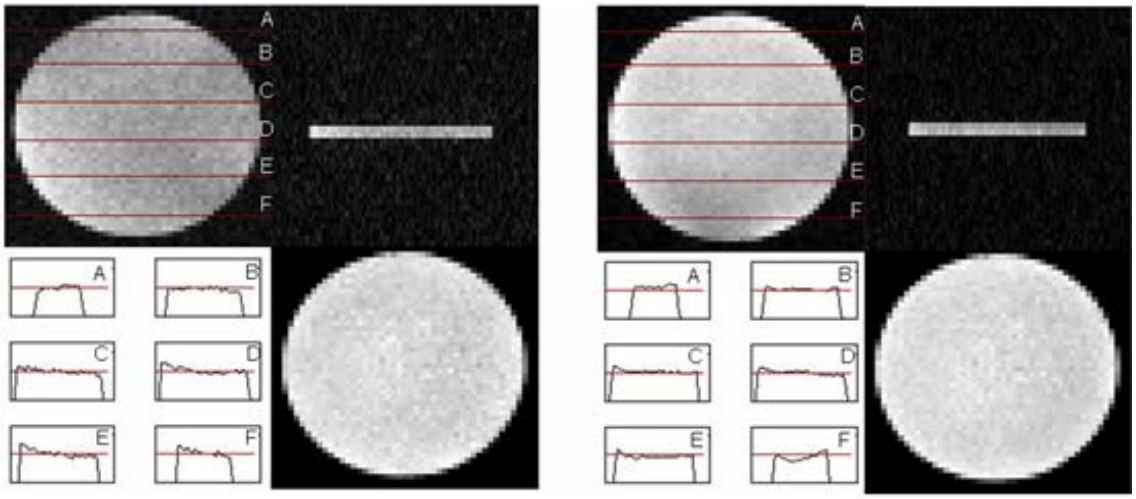

Figure 24: shows the results and simulation data for the 4 spokes (left) and the 7 spokes (right) designs. In each of the two sub-figures, the top left and right are the in-plane and slice selection profiles of results. The bottom left is the Y-slices in-plane profiles of result, and the bottom right is in-plane data from the simulation.

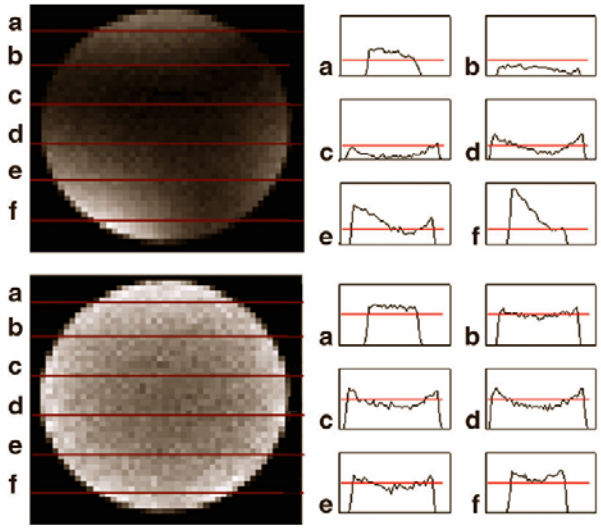

Figure 25: Simulation of standard slice-selective (top) and RF shimming (bottom) excitations. In each of the two subfigures the left panel displays the overall in-plane profile, and the right panel shows a series of in-plane profiles.

2.1.4 Discussion

This work demonstrates the feasibility of 8-channel parallel RF transmission on a clinical human MRI system configured for independent, simultaneous transmission of RF in the presence of time-varying gradients. The results show excellent agreement between measured data and prediction based on numerical Bloch-equation simulations, indicating that the k-space formalism for such RF design provides a good approximation in the low flip angle regime, and the coil transmit B1 phase and amplitude mapping techniques provide the necessary data for high-fidelity designs.

Spirals

In presentation of Figure 20a, it was pointed out that the edges of the phantom are more visible in the acquired data than the simulation, and this effect is more pronounced at higher acceleration factors. This incomplete cancellation of signal near the phantom edge in the acquired data is also the primary source of lower correlation factors at higher acceleration shown in Figure 20b for the target vs. result (green) and simulation vs. result (blue) curves. This is most likely due to the rapid spatial variation of the B_1^+ maps in the vicinity of the RF coils and the phantom edge, where the coil map acquisition has inadequate resolution to capture the excitation field change and truncation of the maps. Since higher acceleration factors require more cancellation of signal from different coils, this artifact is more pronounced at higher acceleration factors. To minimize these cancellation artifacts, a computational method or a design that efficiently incorporate high-resolution B_1^+ maps for a large number of coils is needed so that higher acceleration factors can be accurately realized.

At low acceleration factors, B_0 off-resonance effects were found to be in the range of 30-45 Hz, and were likely due to frequency drift during acquisition of multiple-average datasets with long acquisition times. More spatial blurring is apparent in the 2D design with 1X and 2X designs than the 3X and 4X as expected because of the increased

B_0 sensitivity of the longer pulses at lower accelerations (e.g. 9.47 ms at 1X vs. 2.42 ms at 4X).

Ullman et al (12) reported several correlation factors with a 4-coil setup, including correlations for simulation vs. result, and target vs. result. Although the current design differs from that of (12) in RF, gradients, and experimental setup, the simulation vs. result and target vs. result correlations for acceleration of 2 and 2.67 in (12) are comparable to the correlation factors for acceleration of 2 and 3 in our study. It's expected that for a fixed acceleration factor, the correlation between target and result will improve with a larger number of coil; however, we note that low-resolution B_1^+ maps can reduce the achievable correlation as is the case for the current study.

Spokes

Although the spokes design achieves a nearly uniform in-plane magnetization profile, Figure 24 demonstrates some deviation from the simulations. For the 7 spokes case, the results shown were from an acquisition using TR=30 ms. It was observed that the deviation from the target profile was reduced at this longer TR (compared to the TR = 20 ms case), indicating that the non-uniformity artifact may be related to stimulated echo formation[1].

2.1.5 Conclusion

Spatially-selective, low flip angle parallel RF excitation was demonstrated to work well on commercially available 3T human-scanner hardware. With parallel RF excitation, selective multi-dimensional excitation with high resolution can be implemented with substantially reduced duration. For instance, without significant degradation in slice profile, the duration of a 5-mm resolution 2D excitation can be reduced from 9.47 ms to

[1] Stimulated Echo: Transverse magnetization from prior TRs can be recalled back to the current TR if its phase happens to be coherent with the current transverse magnetization at the data acquisition point. This is more likely to occur when short TR is employed and will cause artifact in the image.

1.95 ms through a five-fold acceleration, with the added benefit of reduced sensitivity to off-resonance effects

2.2 In Vivo Experiments

2.2.1 Introduction

The following work provides the first demonstration of parallel RF excitation in human in vivo scan. For in vivo application, the differences in susceptibility of various tissues in the body, such as in the air-tissue interface in the sinuses, can lead to large B_0 inhomogeneity in the imaging volume, causing detrimental effect to the excitation profile. A method for B_0 correction, based on extending the work in (11), was applied to effectively correct for this issue.

2.2.2 Theory & Method

B_0 inhomogeneity correction

To incorporate B_0 spatial non-uniformity into the excitation design, B_0 inhomogeneity map, $(\Delta B_0(\bar{r}))$, was collected and used in both the coils' B_1^+ sensitivity profiles estimation and in the RF design. To create B_0 inhomogeneity map, images at two different echo times (TE1/TE2=5/6 ms) were collected. The phase accrued between these two images (I_1&I_2) is due to the different spin frequencies at different spatial locations and is given by.

Equation 12

$$\Delta\phi(\bar{r}) = \angle\left\{I_1^*(\bar{r})I_2(\bar{r})\right\}$$

With an echo time difference of $\Delta TE = TE_2 - TE_1$, B_0 inhomogeneity map (in Hz) can be obtained via

Equation 13

$$\Delta B_0(\bar{r}) = \frac{\Delta\phi(\bar{r})}{2\pi\Delta TE}$$

B_1^+ map estimation: Similar to the previous section, the B_1^+ profiles estimate were obtained by applying a nonselective, low flip angle RF pulse to a single transmission channel at a time, and receiving through the uniform coil. However, for in vivo applications, large B_0 inhomogeneity $(\Delta B_0(\bar{r}))$ causes significant variation in dipole moments' rotational frequency, resulting in a phase estimation error of the B_1^+ profiles, $\Delta\phi = \gamma(\Delta B_0(\bar{r}))TE$. In this work, based on the B_0 map estimate, the phase of the B_1^+ profile is rewind to remove this error. In addition to this, the magnitude of the B_1^+ profile is fitted to a 3rd-order polynomials to remove the anatomy (from proton density (ρ) weighting) from the estimation. These additional steps in the B_1^+ estimation are illustrated in Figure 26, for one of the transmit coil.

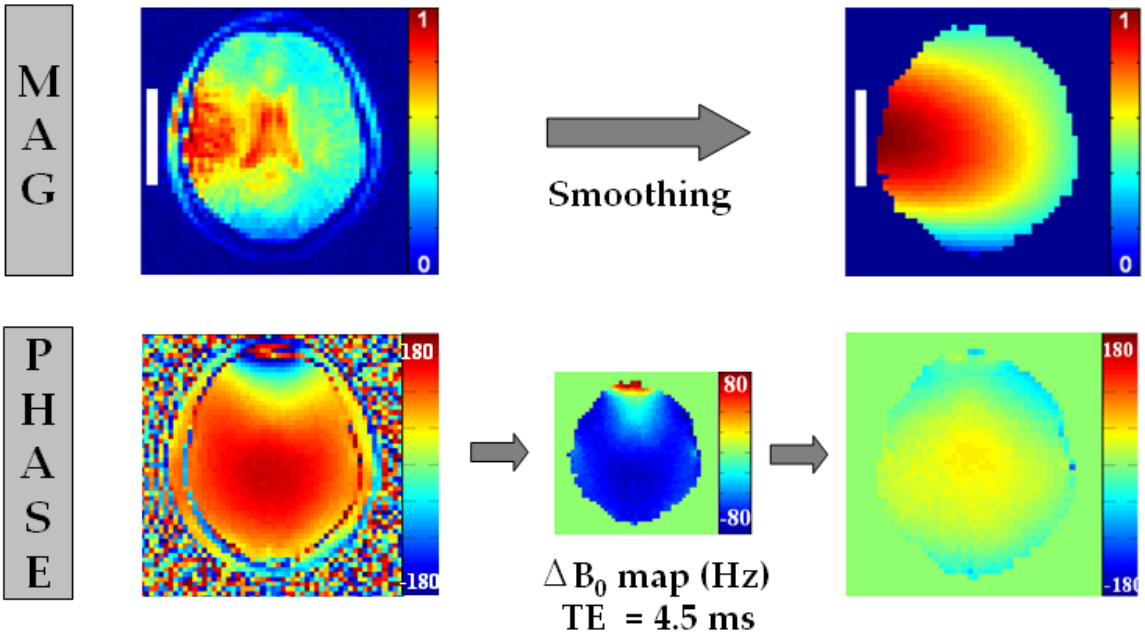

Figure 26: B1+ map estimation: 3-rd order polynomial is used to removed the anatomy and smooth the magnitude profile (Top), B0 map is used to rewind the phase of the phase profile (Bottom)

RF design: To account for B_0 inhomogeneity in the RF design, we followed the method outlined by Grissom et al. in (11), where an additional term, $e^{i\gamma\Delta B_0(\bar{r})(t-T)}$, is added to Equation 4 during the design process to give:

Equation 14

$$m_{xy}(\bar{r}) = i\gamma m_0 \sum_{c=1}^{C} S_c(\bar{r}) \int_0^T b_{1,c}(t) e^{i\gamma \Delta B_0(\bar{r})(t-T)} e^{i\bar{r}\cdot\bar{k}(t)} dt$$

With the addition of this extra term, the subsequence design steps follow as before.

Experimental Validation

Experiments were again conducted on the modified Siemens 3T Tim Trio scanner, equipped with an 8-channel Transmit (TX) Array. Two excitation coil array configurations were used: i) an 8-rung degenerate mode birdcage body coil (46) with a 12-channel matrix head array for uniform receive; and ii) an 8-rung degenerate mode birdcage head coil (30) with uniform-mode body coil for receive (Figure 27). For comparison, both spoke based slice-selective and spiral based 2D spatially selective excitations were created with and without B_0 inhomogeneity correction.

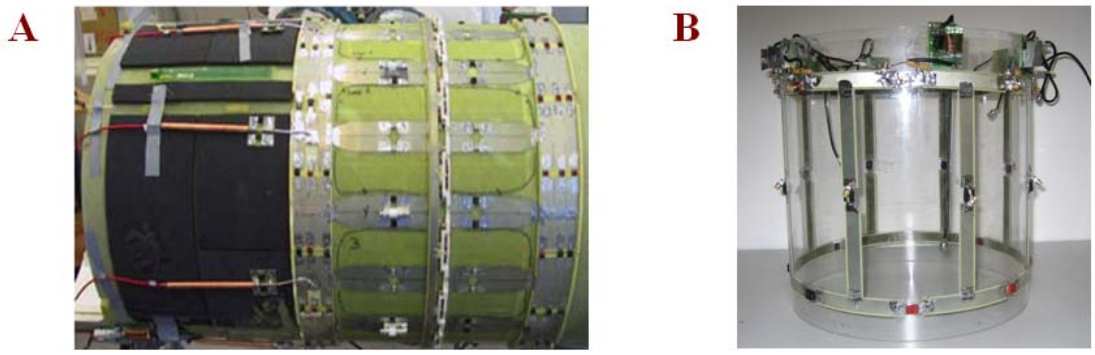

Figure 27: A) an 8-channel excitation body array system, B) an 8-channel excitation head array system.

2.2.3 Results

Body Coil Excitation: Figure 28A (top-left) shows the B_0 map collected, which exhibit strong B_0 variation in the frontal sinus area. For the body coil parallel excitation, uniform slice-selective excitation of 0.5 cm, was performed using a 4-spoke design, with RF pulse duration of 3.42ms. Figure 28A shows the result of the excitation without (top-right) and

with B_0 compensation (bottom-left). Also shown in the figure is the sharp slice-selective profile achieved with this method (bottom-right).

Head Coil Excitation: 2D spatially selective excitations with spiral k-space trajectory were performed using the 8-channel parallel head coil array. Figure 28B shows a 2X excitation of the "Tim Tx" logo without (left) and with (center) B_0 correction. The resolution used for the design is 5 mm and the pulse duration is 4.9 ms. Also shown is a half brain excitation at 4X acceleration without B_0 correction (right), with 5 mm design resolution, and pulse duration of 2.5 ms.

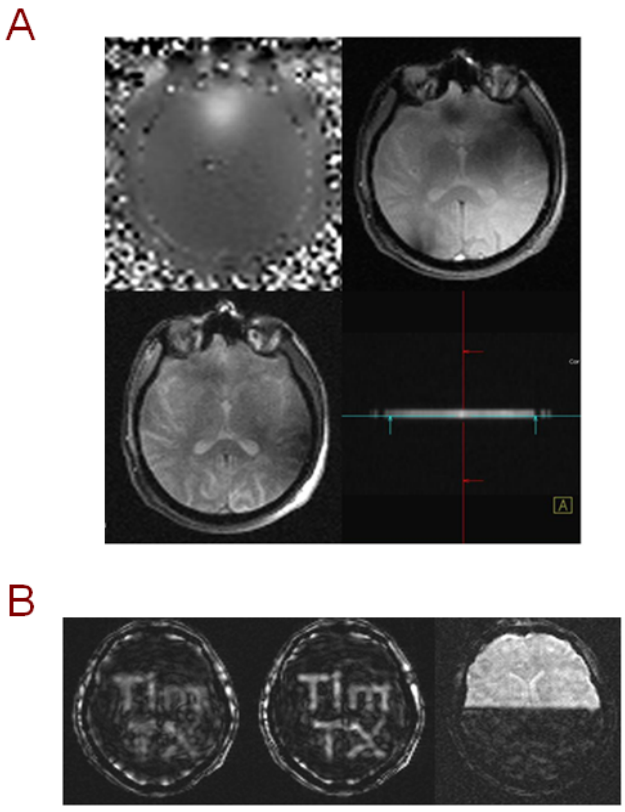

Figure 28: A) Body-array excitation: B_0 map (top-left) shows large inhomogeneity in the frontal sinus area, slice-selective excitation without (top-right) and with (bottom-left) B_0 correction. Slice profile is also shown (bottom-right). B) Head-array excitation: 2X acceleration "Tim Tx" Excitation without (right) and with (center) B_0 correction. 4X acceleration "half brain" excitation without B_0 correction (left).

2.2.4 Discussion and Conclusion

Both slice-selective and 2D spatially selective excitation were created. For the slice-selective excitation with no B_0 correction (Figure 28A), large in-plane non-uniformity in the excitation profile is observed frontally. Significant improvement is achieved when B_0 inhomogeneity is taken into account in the design. However, some residual non-uniformity can still be observed in the right part of the image, which may be due to imperfection in the B_1 map estimate. For the 2D spatially selective excitation (Figure 28B) the "Tim Tx" excitation shows reduced blurring artifact when B_0 correction is incorporated. Also, as expected(12), for the half brain excitation at 4-fold acceleration, the effect of B_0 is minimal because the RF duration is relatively short. Again, artifacts that remain after B_0 correction are likely to result from imperfection in the B_1^+ map estimate. In conclusion, this work provides a demonstration of the use of parallel RF excitation for human scans, where it has been shown that B_0 correction plays an important role in improving the excitation profile.

Chapter 3

Rapid Quantitative B1 mapping

3.1 Introduction

One of the main hurdles in bringing parallel transmission into clinical use is in finding a fast, robust, and reliable technique for acquisition of the RF coils' transmission profiles (B_1^+ maps), a crucial input to excitation pulse design. In chapter 2, B_1^+ maps were estimated to be images acquired by transmitting on each of the transmission coils and receiving with a "uniform" coil, in that case the 3T body coil. Using this estimate, B_1^+ maps can be acquired rapidly. However the acquired maps are qualitative and not quantitative B_1^+ maps, and hence can only be use to design RF pulses to create a general excitation pattern without the exact knowledge of actual flip angle. Furthermore, and more importantly, at high B_0 field strength the receive profiles (B_1^-) of reception coils are non-uniform and different from the excitation profile, and such a method cannot be employed.

Several quantitative B_1^+ mapping methods have been proposed, and are based on measurements at progressively increasing flip angles (47), stimulated echoes (48,49), or signal ratios (50-56). The simplest of these methods is the double-angle method (DAM) (50,52,54), which has been extensively employed. Recently, an extension to this method has been proposed by Cunningham et al (56), where a saturation pulse is used to speed up the acquisition of B_1^+ map data while minimizing T_1 effects. This improved method

was successfully demonstrated for in vivo imaging at 3T on single transmission channel systems.

For parallel transmission, where mapping of many transmit coils with large B_1^+ dynamic range are required, this *saturated* double-angle method (SDAM) can be time consuming even with the incorporation of the reset pulse, and could result in significant error (due to the mapping of large B_1^+ dynamic range). In this work, critical modifications were made to Cunningham et al's method to substantially reduce the acquisition time for mapping transmit array B_1^+ profiles while minimizing the estimation error.

3.2 Theory

This section provides a description of saturated double-angle method (SDAM) proposed by Cunningham et al (56), followed by an outline of alterations made to this method to reduce acquisition time and estimation error. The final part of this section will show examples of B_1^+ mapping obtained via the modified method.

3.2.1 Saturated Double-Angle method

First, we revisit the image intensity equation for general excitation-recovery sequence, given by Equation 7 in Chapter 1 (assuming a short TE). Modifying this equation to account for non-uniformity in transmission (TX) and reception (RX) profiles, and accounting for RF transmission voltage (V) gives

Equation 15

$$I(V,\bar{r}) = \rho(\bar{r})RX(\bar{r})\frac{[1-e^{-TR/T_1(\bar{r})}]\sin\theta(V,\bar{r})}{1-e^{-TR/T_1(\bar{r})}\cos\theta(V,\bar{r})}$$

Estimation of the flip-angle map, $\theta(V,\bar{r})$, can be obtained by collecting images at a set of transmission voltages (V) and fitting the resulting image intensities to Equation 15, voxel by voxel using standard nonlinear search algorithm

such as the Simplex algorithm in Matlab. From the flip-angle map, estimation of the transmission profile, ($TX(\bar{r})$), can be obtained by noting the following relationship between excitation flip-angle and transmission profile

Equation 16

$$\theta(V,\bar{r}) = \gamma \times TX(\bar{r}) \times V \int_0^T RF(t)dt$$

where *RF(t)* is the RF pulse[1] used for the excitation.

Nonetheless, due to T_1 dependence of Equation 15, this mapping technique is ill-conditioned and is very sensitive to noise, especially when short TR acquisitions are used. To get around this issue, long TR acquisition ($TR \geq 5T_1$) is used to remove T_1 dependent from Equation 15, resulting in

Equation 17

$$I(V,\bar{r}) \approx \rho(\bar{r})RX(\bar{r})\sin\theta(V,\bar{r})$$

Which allows for a much more robust transmission map estimation. In addition, with Equation 17, the estimation process can be shortened considerably by using the so-called double-angle method (DAM) (50,52,54). This method relies on the use of image signal ratio rather than image fitting technique; whereby ratio of images at two flip angles α and 2α is taken to give

Equation 18

$$\frac{I(2V,\bar{r})}{I(V,\bar{r})} = \frac{\sin 2\alpha(\bar{r})}{\sin\alpha(\bar{r})} = \frac{2\sin\alpha(\bar{r})\cos\alpha(\bar{r})}{\sin\alpha(\bar{r})} = 2\cos\alpha(\bar{r})$$

From which the flip-angle map (and the subsequence B_1^+ map) can be obtained via:

[1] Since one transmit channel (or mode) is mapped at a time, there is only a single RF pulse.

Equation 19

$$\alpha(\bar{r}) = \arccos\left(\left|\frac{I(2V,\bar{r})}{I(V,\bar{r})}\right|\right)$$

The DAM method has the advantage of requiring image acquisition at only two transmission voltages. Unfortunately, the requirement of a long TR still results in relatively long acquisition time. To overcome this, Cunningham et al. (56) proposed a modification to DAM to allow for short TR acquisitions; whereby after each data acquisition, a magnetization saturation pulse (M_z RESET pulse) is employed to destroy M_z (Figure 29).

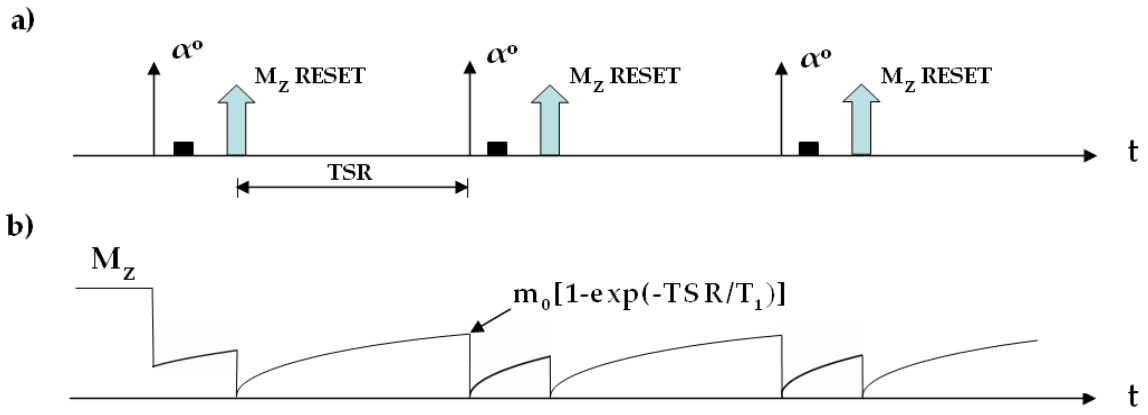

Figure 29: The RESET pulse sequence used in *Saturated* Double-Angle Method. Sequence diagram in (a) shows the saturation pulse (M_z RESET) being applied after each data acquisition to saturate Mz prior to the next excitation. The M_z time course of this sequence is shown in (b).[1]

A composite pulse train (57) or BIR4 pulses (58), can be used as the RESET pulse which completely saturate M_z for the range of B_1^+ values present in the transmission profile. From the M_z time course diagram in Figure 29(b), image intensity expression of the modified sequence can be derived as (assuming TE~ 0)

[1] Note: In the sequence, prior to the application of RESET pulse, gradient crushers are applied to destroy the coherence of transverse magnetization. This significantly reduces the undesirable feature of the RESET pulse in which transverse magnetization along M_x is rotated back into the longitudinal axis to produce M_z. To further reduce this undesirable feature, the time between the end of data acquisition and the application of RESET pulse can be increase to allow for T_2 decay.

Equation 20

$$I(V,\bar{r}) = \rho(\bar{r})RX(\bar{r})(1-e^{-TSR/T_1(\bar{r})})\sin\theta(V,\bar{r})$$

This expression is analogous to image intensity expression for saturation-recovery sequence given by equation 7 in Chapter 1, with repetition time TR being replaced by saturation recovery time TSR. Analogous to 90° pulse in saturation-recovery, the RESET pulse in this sequence completely saturate M_z. However, here the pulse is applied after data acquisition and must work in the presence of spatially varying B_1^+.

Using the image intensity expression in Equation 20, DAM can be used as before to obtain flip-angle map via Equation 19. Further, using this *saturated* double-angle method (SDAM), long TR acquisition is no longer necessary. However, very short TR impose an SNR penalty, as in such case saturation recovery time (TSR) allows only limited M_z recovery

For parallel transmission, B_1^+ mapping of many coils with large spatial B_1^+ dynamic range is required, causing problems for direct application of SDAM. With large B_1^+ dynamic range, the double-angle method suffers from 2π ambiguities in regions where α is too large, and is also sensitive to noise in regions where α is too small. To overcome this limitation, Kerr et al (59,60) proposed a method based on acquiring images with the RESET pulse sequence at n flip angles $\alpha, 2\alpha, 2^2\alpha, ..., 2^{n-1}\alpha$ and using an image intensity fitting technique instead of DAM to estimate the flip-angle map. In addition, the RESET pulse transmission is modified to account for large B_1^+ variation in the transmit profile. Generally, a RESET pulse can only perform well over a limited range of B_1^+ variations, and hence transmitting the pulse via a single coil element with large B_1^+ variation will not adequately saturate M_z in the entire imaging volume. The approach used in (60), is to transmit the RESET pulse in parallel, first with the odd then the even coil elements of the (loop) array. Full saturation is achieved as long as the mutual volume saturated by either RESET pulse covers the whole imaging volume.

(Note: In (47), the phased-transmit modes such as mode-1 birdcage still contains significant B_1^+ variation and the RESET pulse transmitted using one of these modes could not completely saturate the entire imaging volume).

With Kerr et al's method, measurements at several transmission voltages from each of the transmission coils is required to estimate the B_1^+ profile of all the coil elements in an array. This result in long data acquisition times, especially when many coil elements are present. Furthermore, the extensive use of RESET pulse in the acquisition sequence can lead to high Specific Absorption Rate (SAR, heating of tissues)[1], which is problematic for in vivo applications, and will by itself impose longer TR values and longer overall scan times.

In the following section, we provide an alternative method for B_1^+ estimation in parallel transmission, which only requires a small number of acquisitions and a limited utilization of the RESET pulse, thus yielding a mapping method with a relatively short acquisition time, robustness to large dynamic range of B_1^+ and B_1^-, and low SAR.

3.2.2 Rapid Quantitative B_1^+ Mapping via Receive profile estimation

Instead of directly performing quantitative B_1^+ mapping on each of the transmit coils, the proposed method utilizes a synthesized receive profile, i.e. the (density-weighted) B_1^- profile of the receive coil array. Once this receive profile is estimated, only a single low voltage measurement will be required from each of the transmission coils for the estimation of the individual B_1^+ transmission profiles. Therefore, the total data acquisition time in this method is much shorter than in previous techniques, especially for systems with large number of transmission coils. Furthermore, in this method, the RESET pulse will only be used for receive profile estimation, resulting in a much lower SAR.

[1] The Specific Absorption Rate is defined as the RF power absorbed per unit of mass of an object, and is measured in watts per kilogram (W/kg).The SAR describes the potential for heating of the patient's tissue due to the application of the RF excitation pulse.

Throughout the mapping process the synthesized reception profile from the same receiver coil combination is used. Reception through a coil with uniform receive profile is ideal since it provides good reception of signal from every spatial location in the FOV. Unfortunately, this is not possible at high B_0 field due to B_1^- inhomogeneity. However, for birdcage coils, uniform reception mode (mode-1) can still be used since the profile of this reception mode should not exhibit signal null spot and should provide adequate reception of signal from all spatial locations. For other types of coil array, receive signal from the coil elements should be combined such that the overall reception profile exhibit no null spot.

The estimation of density-weighted receive profile is performed in two steps. First estimation of mode-1 birdcage transmission profile of the coil array is performed. This estimated profile is then use along with the data from an extra acquisition to estimate the receive profile.

The mode-1 birdcage transmission profile is estimated via a similar technique to one proposed by Kerr et al. However, measurements at only a small number of transmission voltages are required (4-5 in this work) due to the relatively low B_1^+ variation in mode-1 transmission[1]. Here, standard nonlinear search algorithm (Simplex) in Matlab was found to be adequate in fitting the acquired image intensities to Equation 20 to obtain angle map estimate, $\theta_{\text{mode-1}}(V,\bar{r})$.

The second step in estimating the receive profile is to acquire an additional low-flip-angle image via mode-1 transmission at a known low voltage level (without the magnetization saturation pulse). At low-flip-angle, $\cos\theta \approx 1$, and the image intensity expression for this acquisition can be approximated as (starting from Equation 15)

[1] For most birdcage arrays at 7T, B_1^+ variation of mode-1 is around 3:1 (peak-to-trough). This variation is large for imaging but small compared to the variation observed in profiles of the individual coil elements. Also note that instead of the parallel technique used by Kerr et al. for Mz saturation, here the mode-1 birdcage is used for transmitting the RESET pulse since the 3:1 variation is small enough to allow the RESET pulse to create good saturation in the entire imaging volume.

Equation 21

$$I(V,\bar{r}) = \rho(\bar{r})RX(\bar{r})\frac{[1-e^{-TR/T_1(\bar{r})}]\sin\theta_{\textbf{mode-1}}(V,\bar{r})}{1-e^{-TR/T_1(\bar{r})}\cos\theta_{\textbf{mode-1}}(V,\bar{r})} \approx \rho(\bar{r})RX(\bar{r})\sin\theta_{\textbf{mode-1}}(V,\bar{r})$$

From this expression, an estimate of the density-weighted reception profile, $\rho(\bar{r})RX(\bar{r})$, can be calculated by dividing the acquired low-flip-angle image by $\sin\theta_{\text{mode-1}}(V,\bar{r})$, which can be obtained using the estimated mode-1 transmission profile. Since Equation 21 is approximately independent of TR, short TR and hence fast acquisition can be use to obtain the low-flip-angle image.

Once the density-weighted reception profile is estimated, the B_1^+ profile of individual transmit coil elements (or modes) can be obtained though a single low-flip-angle image acquisition of each coil element. According to Equation 21, the flip-angle profile of the transmit coil elements/mode, $\theta_{\textbf{indiv}}(V,\bar{r})$, can be obtain by dividing the low-flip-angle image, $I_{Indiv}(V,\bar{r})$, by density-weighted reception profile along with taking an inverse sine of the resulting image, pixel-by-pixel.

Equation 22

$$\theta_{\textbf{indiv}}(V,\bar{r}) = \sin^{-1}\left(\frac{I_{\textbf{indiv}}(V,\bar{r})}{\rho(\bar{r})RX(\bar{r})}\right)$$

From the flip-angle profiles, B_1^+ profiles can then be obtained via Equation 16.

As a side note, the use of mode-1 birdcage transmission is not required for the mapping of the receive profile. Transmission on any coil or mode can be used for this purpose. Nonetheless, by using a transmission mode with relatively low B_1^+ variation, such as mode-1, only a small number of measurements are required for the receive profile estimation.

A flowchart in Figure 30 summarizes the quantitative B_1^+ mapping procedure, where first estimation of the receive profile is performed (steps 1-5), followed by estimation of the B_1^+ maps for each individual transmit coil (or mode) (steps 6-7).

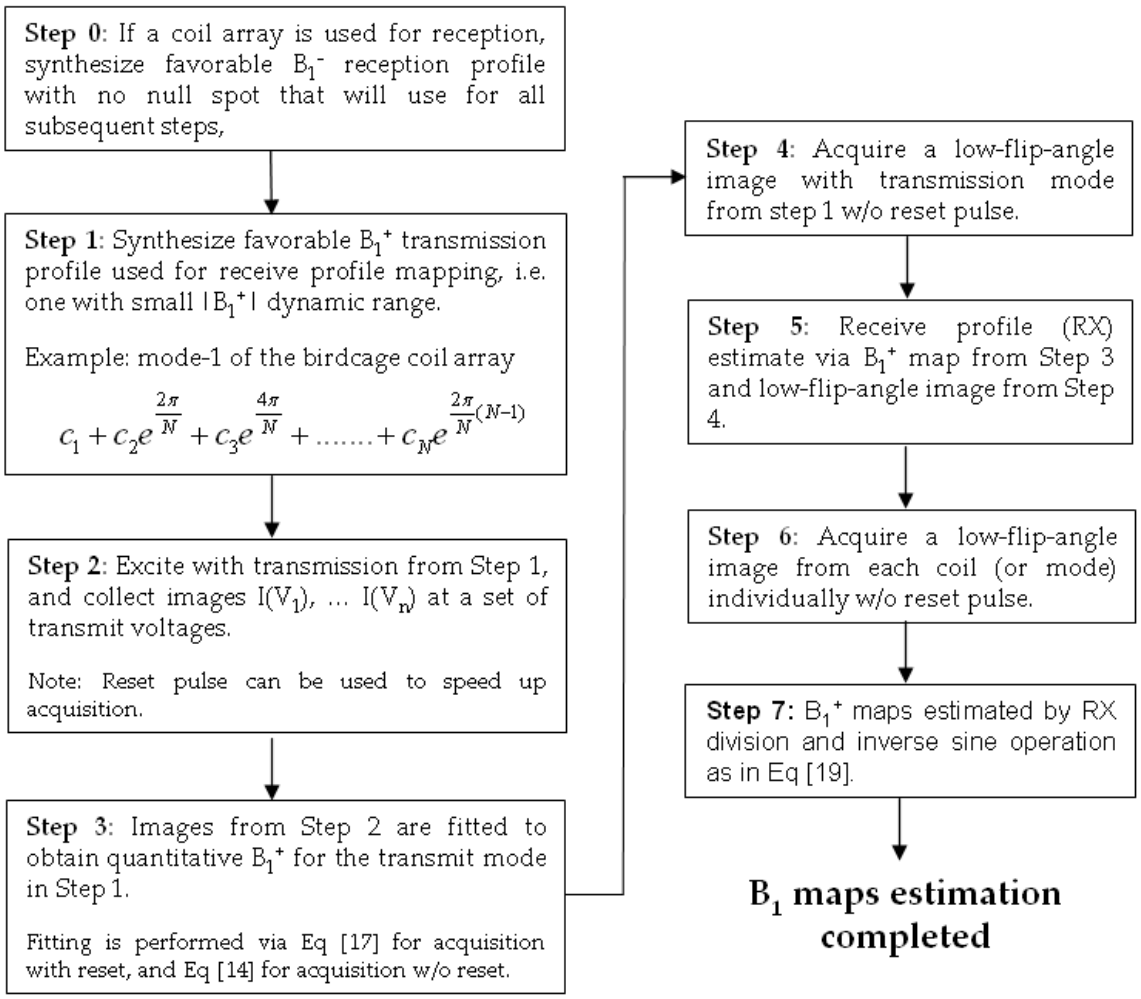

Figure 30: Flowchart outlining the rapid quantitative B1+ mapping technique, where first receive profile of the reception coil is estimated in step 1-5, after which B1+ maps of the transmit coils (or modes) can then be obtain via step 6-7.

3.2.3 Experimental B_1^+ mapping

The rapid quantitative B_1^+ mapping method presented in the previous section is used to estimate B_1^+ profiles of two birdcage coil arrays at 7T in a water phantom setup. The results of these mappings are shown in Figure 31 and Figure 32.

Figure 31, shows results for the first coil: an eight channels stripline coil array. The left panel (a) shows the image of the coil array and estimates of mode-1 transmit (TX), and receive (RX) profiles[1] along with the transmit-receive image (TX-RX). On the right (b), are the transmit magnitude (top) and phase (bottom) profile estimates of the individual excitation coils.

The second coil that was mapped is a sixteen-channel stripline coil array. In this case, transmit profiles of the eight useful birdcage modes of the coil array were estimated. In Figure 32 (a), images of the coil array and the butler matrix hardware used for mode generation are shown along with the estimates of mode-1 TX and RX profiles along with the TX-RX image. On the right of the figure (b) are the transmit magnitude (top) and phase (bottom) profile estimates of the individual excitation modes.

The coil profiles estimates present here were used in parallel transmission work in chapter 5, 6 and 7. In chapter 4, the two coil arrays presented here were also used. However, the experiments performed in these chapters occurred in parallel with development of the B1+ mapping technique, and as such an inferior slower variant of the method without the RESET pulse was used for the mapping.

[1] Note: at high B_0 field strength the magnitude of TX and RX profiles of a coil (or mode) is different, unlike the low-B_0-field case.

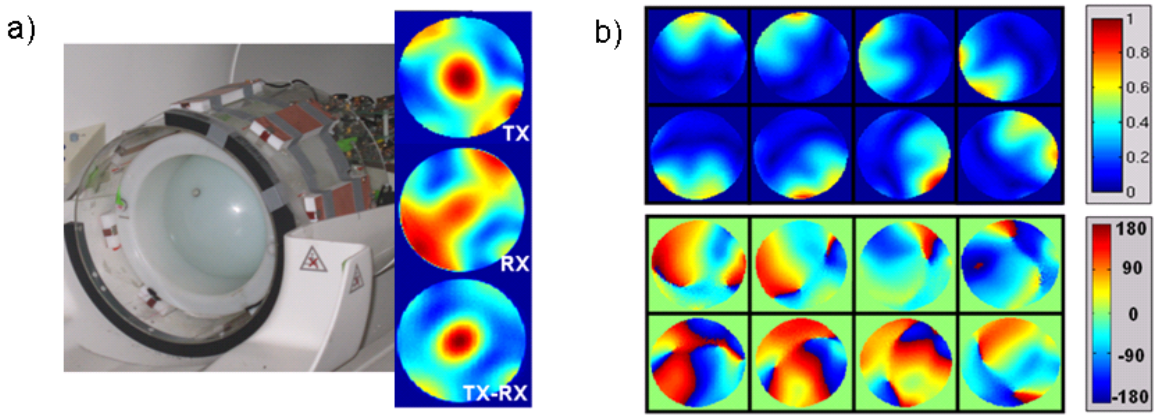

Figure 31: a) Eight-channel transmit/receive stripline coil array for 7T. The insert on the right panel of a) shows the estimated transmit (TX) and receive (RX) profiles and the transmit-receive image (TX-RX) of the CP mode of the array for a water-filled spherical phantom placed inside a loading ring. b) The upper panel shows estimated magnitude (intensity scale normalized to a maximum value of 1), and the lower panel shows phase (degrees) of the individual excitation coil profiles.

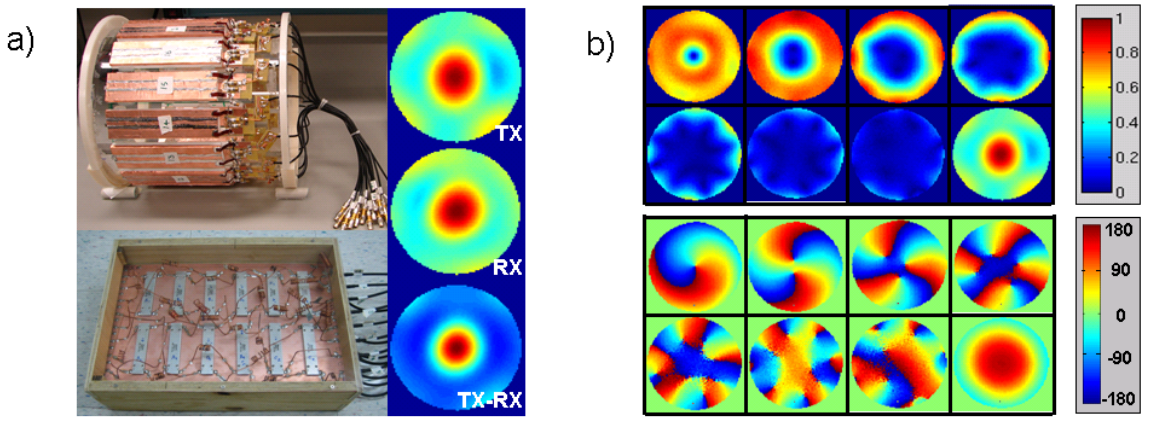

Figure 32: a) Sixteen-channel transmit/receive stripline coil array for 7T, and the butler matrix hardware that was used for the experiments in this work. The insert on the right panel of a) shows the estimated transmit (TX) and receive (RX) profiles and the transmit-received image (TX-RX) of the CP mode of the array for a water-filled spherical phantom. b) The upper panel shows the estimated magnitude profile (intensity scale normalized to a maximum value of 1), and the lower panel shows the phase profile (in degrees) of the eight orthogonal birdcage transmission modes used.

Chapter 4

Magnitude Least Square Optimization

4.1 Introduction

In this work, we propose an extension to the spatial domain parallel excitation pulse design method introduced by Grissom et al (11), where we apply magnitude least squares optimization to improve excitation magnitude profile and reduce the required RF power at a cost of increased phase variations in the excitation pattern. In many excitation applications, such as when magnitude images are recorded, low-order spatial phase variations do not impose a significant penalty. We therefore develop a method for pulse calculation with an adjustable regularization parameter de-emphasizing the excitation phase profile and study the potential benefits in magnitude profile fidelity and SAR which can accompany this relaxed constraint.

The idea of permitting phase variation in the excitation profile has previously been exploited in several applications, including the design of quadratic-phase RF pulses (61,62), RF shimming (43-45,63), and frequency-sweep pulses (64), with benefits such as improved magnitude transition bands for saturation pulses, homogeneity for RF shimming, and reduced RF peak power for frequency-sweep pulses. In this work, we propose a method that allows us take advantage of relaxed constraints on the phase profile for parallel excitation design. Our approach is based on a variant of a local optimization method used for solving general magnitude least square problems (65). We demonstrate the method using a 2D spiral excitation with R=4 fold acceleration over the

Nyquist sampling and a uniform in-plane slice-selective spoke excitation (13,23) on an 8-channel excitation system at 7T.

Recently, at the ISMRM'07 conference, Katscher el al. (66) demonstrated the significant improvement gained in RF shimming when a magnitude least square approach is used. Kerr et al. (67) also proposed an approach for magnitude least square optimization for the design of parallel RF excitation and demonstrate the method using a spiral trajectory. The approach in this work differs in that it takes into account of intra-voxel dephasing[1] and enables the designer to systematically trade off the allowed spatial phase variation for the improvement in magnitude profile and reduction in RF power. Furthermore, the work provides an extensive simulation and experimental study on the possible benefit of the algorithm on both spiral and spoke k-space trajectory excitations at high magnetic field strength.

4.2 Theory

Parallel excitations are often designed as a least-squares (LS) optimized approximation to a target magnitude and phase profile. In Grissom's formulation, the RF pulses can be designed by solving the following least-square optimization (as represented by Equation 5, in Chapter 1):

Equation 23

$$b = \arg_b \min\{\|Ab - m\|_w^2 + R(b)\}$$

where, m is the target transverse magnetization after excitation, and b contains the RF waveforms. The optimization is performed over the Region of Interest implied by a weighting, w, and $R(b)$ denotes a regularization term that may be use to control integrated and peak RF power. With Equation 23, RF waveforms are found that will reduce the deviations from the target profile in both the magnitude and phase.

[1] Significant phase variation across a voxel will cause signal loss when the signal is summed up across the voxel to create an image.

However, in many applications, such as conventional slice-selective excitation for structural imaging where only magnitude images are of interest, the primary metric of interest is the fidelity of the magnitude profile while the phase profile is relatively unimportant. In such cases, the following *magnitude* least square (MLS) optimization,

Equation 24

$$b = \arg_b \min\{\| \,|Ab| - m\,\|_w^2 + R(b)\}$$

may provide an improved magnitude profile, but at the cost of increased spatial phase variations. Here, m is specified as a real-valued vector. Unlike Equation 23, the MLS optimization, represented by Equation 24, is unfortunately not convex and generally cannot be solved with a guarantee of global optimality. Kassakian (65) recently proposed two different methods (in the context of audio signal processing) for solving this MLS problem, but without any regard to the resulting phase profile. With these methods, superior magnitude profile can be achieved when compared to the solution from Equation 23. For application of these methods in MRI RF excitation design, intra-voxel dephasing can become an important constraint that limits the degree of allowable spatial phase variation. Thus, we extend Kassakian's work on the so-called local-variable exchange solution, by imposing a mild constraint on the phase in the form of a smooth and slowly varying spatial phase profile.

We follow the notation of the local variable exchange method in (65). We start by rewriting Equation 24 as:

Equation 25

$$b = \arg_{b,z} \min\{\sum_{i \in W} |A_i b - m_i z_i|^2 + R(b)\}$$

$$s.t. |z_i| = 1$$

where z_i is an extra phase term and A_i is the i^{th} row of A. From Equation 25, for a fixed z, the minimization of b can be solved as in Equation 24. In turn, for a fixed b, the optimal

vector, z, contains values z_i with a modulus of 1 and phase equal to that of $A_i b$. By starting with a feasible pair, b and z, and then keeping one variable fixed and solving for the other, we can only improve the objective function. Since the objective function is non-negative, by alternating this procedure a local minimum will eventually be reached.

As previously mentioned, the solution from the variable exchange method provides no guarantee that the phase behavior of the resulting excitation profile will be slowly varying compared to the pixel length. The phase profile will strongly depend on the solution to z, which contains the specified desired phase. To impose a smooth phase variation, we place a restriction on the evolution of phase of z during the optimization loop, as shown schematically in Figure 33, which is a flow diagram summarizing the modified local-variable exchange optimization. For each iteration step, rather than using the optimal z according to the original algorithm, a phase-smoothed version of the optimal z was calculated and used in the optimization. This modification forces the phase of z to evolve smoothly. However, there are natural tradeoffs in the choice of degree of phase smoothing for z, such that too much smoothing places overly conservative constraints on the optimization, resulting in a solution with an unnecessarily high cost. To avoid over-constraining the problem, the effect of the smoothing parameter was evaluated. For our designs, we chose a Gaussian smoothing kernel and empirically found that a good compromise of phase smoothing could be obtained by applying a 5x5-pixel Gaussian low-pass filter with σ=2 pixels to smooth the phase profile variation to less than 8°/mm. This phase smoothing was only applied to non-zero-magnitude regions in the excitation target profile. As a final design step, after the completion of the optimization, a short 'rewinder' gradient was appended to the excitation pulse to remove any residual linear component of the spatial phase variation.

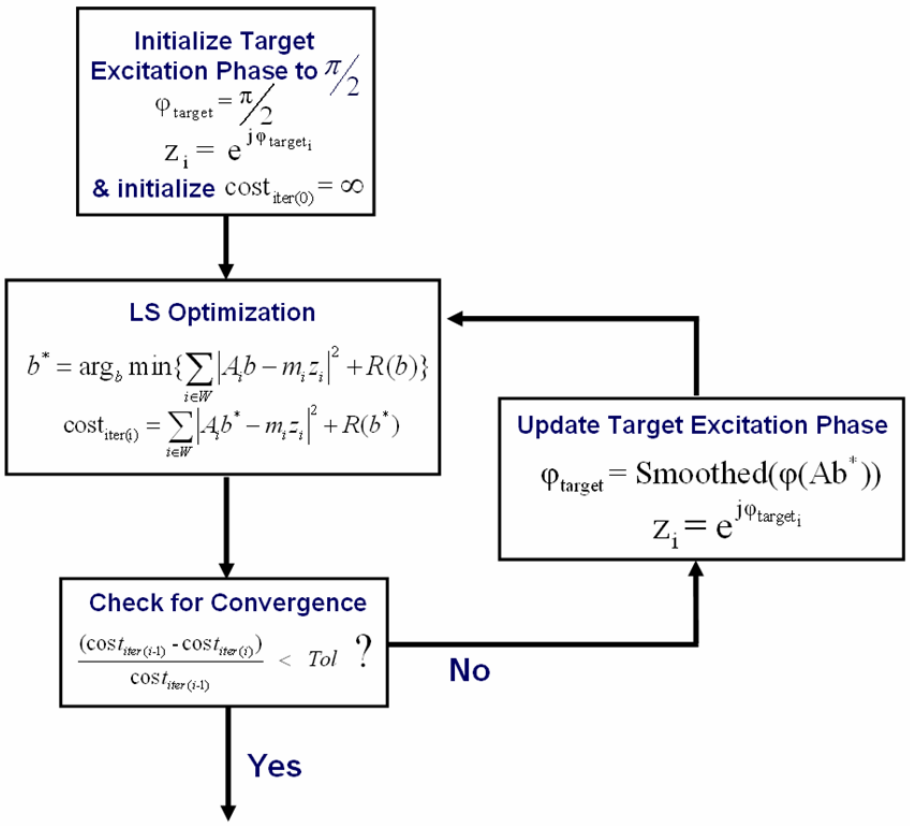

Figure 33: Flow diagram of the modified local-variable exchange method for Magnitude Least Square optimization. During the iterative optimization process, a smoothed version of the excitation phase from the previous iteration is used as the target excitation phase for the current iteration. The smoothing of the excitation phase profile is performed using a designer-specified Gaussian filter, enabling the designer to systematically trade off the allowed spatial phase variation for an improvement in the magnitude profile and reduction in RF power.

4.3 Methods

Simulation Study

To compare the performance of the conventional LS with the MLS optimization, RF pulses were designed using these two methods, each for two types of excitation k-space trajectories**:** 1) a two dimensional spiral excitation with a four-fold acceleration, design resolution of 2 mm, and a field-of-view of 18 cm. 2) a slice-selective 4-spoke excitation with sinc sub-pulses' time-bandwidth-product equal to 4. A square excitation target

profile was used for the spiral excitation and a uniform slice-selective excitation of 1 cm thickness target profile was used for the spoke. Maximum gradient amplitude of 25 mT/m and slew rate of 150 T/m/s were used for all designs.

Similar to (11), Tikhonov regularization ($R(b) = \beta \|b\|_2^2$) was used for both conventional LS and MLS optimizations. For both spiral and spoke excitations, the RF pulses were designed for a set of Tikhonov regularization parameter values (β) to illustrate the clear tradeoff between the reduction in excitation error and the increase requirement in RF power. Deviations from the target profile were assessed using root magnitude mean square error (RMMSE) defined here as

Equation 26

$$RMMSE = \sqrt{\| \, |Ab| - m \, \|_w^2}$$

To limit intra-voxel dephasing in the MLS optimization design, the smoothing parameter of the Gaussian filter in the optimization was adjusted such that the resulting phase profile variation is less than approximately 8°/mm (after rewinding). In addition, a short rewinder gradient appended to the RF pulse was use to remove residual linear component of the spatial phase variation. The area of the rewinder was calculated based on a linear fit to the Bloch equation simulated spatial phase profile.

System Hardware

For experimental verification of the method, the RF pulses were tested on a Siemens prototype 7T Magnetom scanner (Erlangen, Germany), equipped with an 8-channel transmit system, with maximum gradient amplitude of 40 mT/m and slew rate of 200 T/m/s. An 8-channel stripline coil array was used for transmit and receive (30). The RF array was built around a 28-cm diameter acrylic tube (Figure 34) and was driven through a transmit-receive switch at each of the 8 rungs. For parallel transmission, the individual coil elements are each driven directly by a RF amplifier. For signal reception,

the 8 receive channels from the same coil array are combined to create mode-1 birdcage reception. All measurements were performed in a 17-cm diameter doped water phantom, containing 1.25grams/liter of Nickel Sulfate and 5 grams/liter of Sodium Chloride. A cylindrical loading ring (filled with doped water containing Manganese Chloride to reduce its T_1 to less than 3ms), was used to reduce the amount of B_1 inhomogeneity observed in the spherical water phantom to a similar level observed in human in-vivo imaging. The bottom right of Figure 34, shows the transmit-received (TX-RX) birdcage image for in-vivo and for the water phantom with loading ring. The peak-to-trough signal ratio is ~9 and ~8.5 for in-vivo and water phantom respectively. Without the loading ring, the water phantom's peak-to-trough signal ratio would have been ~13 which is much higher than that observed in-vivo with this particular setup.

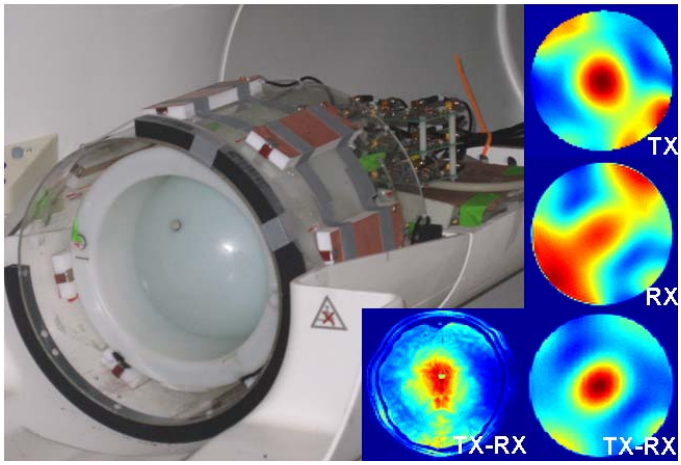

Figure 34: Eight-channel transmit/receive stripline coil array for 7T that was used for all experiments in this chapter. The insert on the right panel of a) shows the estimated transmit (TX) and receive (RX) profiles and the transmit-received image (TX-RX) of the birdcage mode of the array for a water-filled spherical phantom placed inside a loading ring. Also shown is an example of the transmit-received image (TX-RX) of the birdcage mode of the array for an axial brain section that demonstrates comparable inhomogeneity to the transmit-received image of the phantom.

Low-flip-angle Validation

In (11), it was shown that with low Tikhonov regularization parameter value (β), i.e. high RF power requirement, the excitation profile can be heavily degraded from the low flip angle approximation even at relatively low flip angle. For the current work, the applied excitation voltages were established to be well within the low-flip-angle regime, although without a full quantitative B_1 map to determine the exact excitation flip angle. For example, in the spiral-based pulse design, we made our calibration by exciting the design that required the highest power (the LS design with β = 0.3) with a sequence of increasing voltages and quantified the resulting profiles. For very low excitation voltages, the signal-to-noise ratio (SNR) is low, and at high excitation voltage, the low-flip-angle approximation fails. We chose the voltages for our experiments to be such that our data are acquired with ample SNR, but at the same time are low enough to not violate the low-flip-angle approximation. In our current setup, we found that this favorable operating range for the voltage extended from 30V to 100V for this design (β = 0.3).

The excitation patterns were imaged using a standard 3D imaging sequence (gradient-recalled echo) with matrix = 128x128x32, FOV = 256mm x 256mm x 160mm, voxel resolution = 2mm x 2mm x5mm, TR/TE/BW = 100ms, 6ms, 260pixel. The excitation profile was inferred by dividing the reconstructed image by the estimation of the birdcage receive profile. The RF excitation pulses were adjusted so that all the experimental results are of the same target flip angle.

To make a comparison between simulation and experimental results, the root magnitude mean square error (RMMSE) for the simulation data is calculated assuming a target transverse magnetization value of m_{xy} = 0.1. For the experimental results, the intensity is scaled so that the mean signal in the target excitation ROI matches that of the simulation, after which the RMMSE is then calculated

4.4 Results

Spiral Trajectory

The four-fold accelerated (4x) spiral excitation design yielded 3.51 ms long pulse, with an additional 70μs for the rewinder gradient in the MLS cases. Figure 35a) shows a comparison between the LS and MLS design for Tikhonov regularization parameter value of 1.5. Visually, the MLS magnitude profile shows improved target excitation and background noise suppression in areas outside the target square. For this particular β, the MLS optimization yields an improvement of 15.62% in RMMSE and 26% and 41% in integrated and peak RF power over the LS method. Figure 35b shows the plot of the normalized RMMSE vs. the normalized RF voltage norm across all eight channels ($\|b\|_2$) for four different settings of the Tikhonov regularization parameter (β). The dotted red and blue curves represent the simulation results for conventional LS and MLS, respectively. Similarly, the solid red and blue curves show the experimental tradeoff between mean square error and pulse energy at the different regularization parameters. The average drop in RMMSE over the four data points is 12% for simulation data and 10% for experimental data. The average integrated RF power drop is 5.7% and the peak RF power drop is 9.3%.

We note that the MLS computation time (3 GHz, 64-bit Xenon processor, Linux operating system), for the spiral-based designs ranged from 5-8 minutes for higher Tikhonov regularization parameter values, up to approximately 35 minutes for lower value ($\beta = 0.3$).

Figure 36 illustrates the tradeoff between an increase in spatial phase variation for lower magnitude mean squared error and reduced RF power with MLS optimization compared conventional LS designs. The magnitude (left) and phase (right) profiles of the square target excitation with $\beta = 1.5$, for LS and MLS optimization are shown in row a) and b) respectively. Similar to Figure 35a), the magnitude profile of the MLS design is

visually better than the LS design. In Figure 36c), the increased in spatial phase variation across the target excitation area for MLS design can clearly be observed. This observed phase variation is shown to be very similar to the predicted variation.

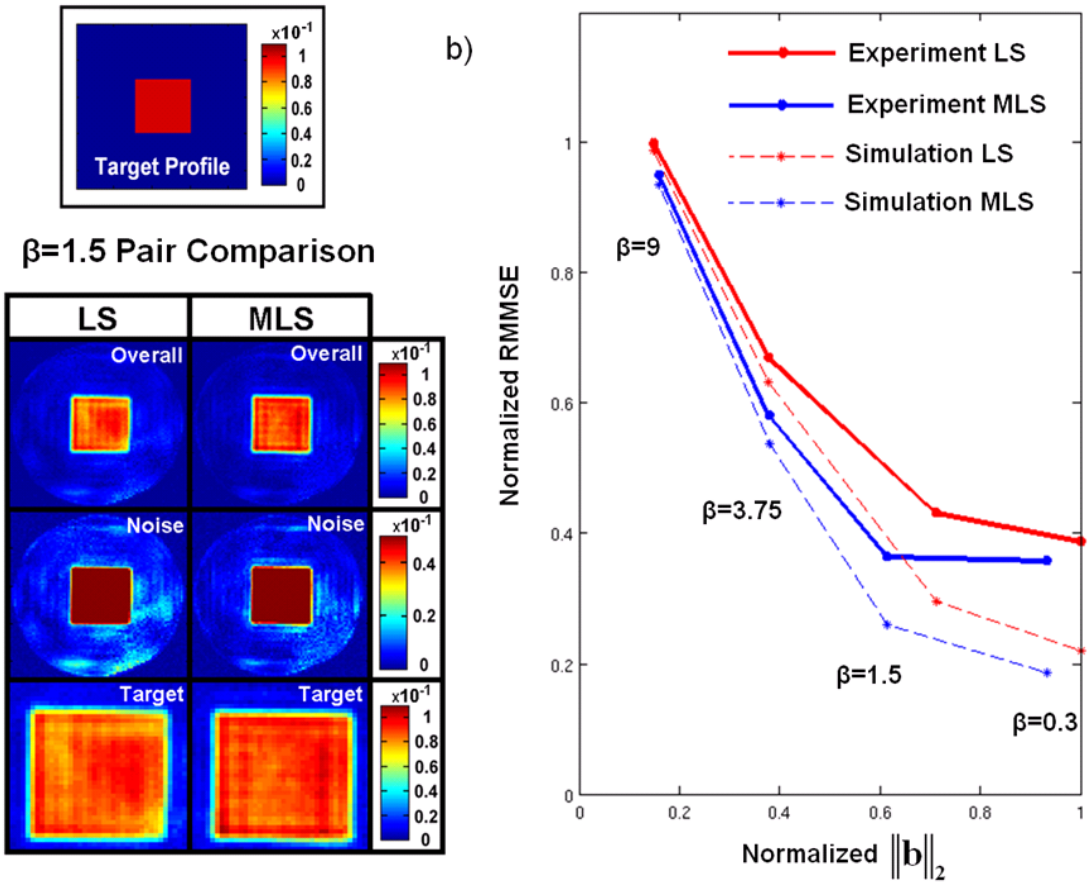

Figure 35: **a)** Experimental square-target excitation, imaged in a central axial section of a 3D-encoded readout. The figure illustrates the excitation magnitude profile improvement with the Magnitude Least Squares design when compared to the conventional Least Squares design for the Tikhonov regularization parameter value of 1.5. The top row compares the overall excitation. The window and level parameters for the second row are set to bring out the background noise, and the third row is windowed to best compare the intensity variation within the square target excitation. **b)** Plot of normalized RMMSE vs. RF voltage norm across all 8 channels ($\|b\|_2$), for four different settings of the Tikhonov regularization parameter (L-curve).

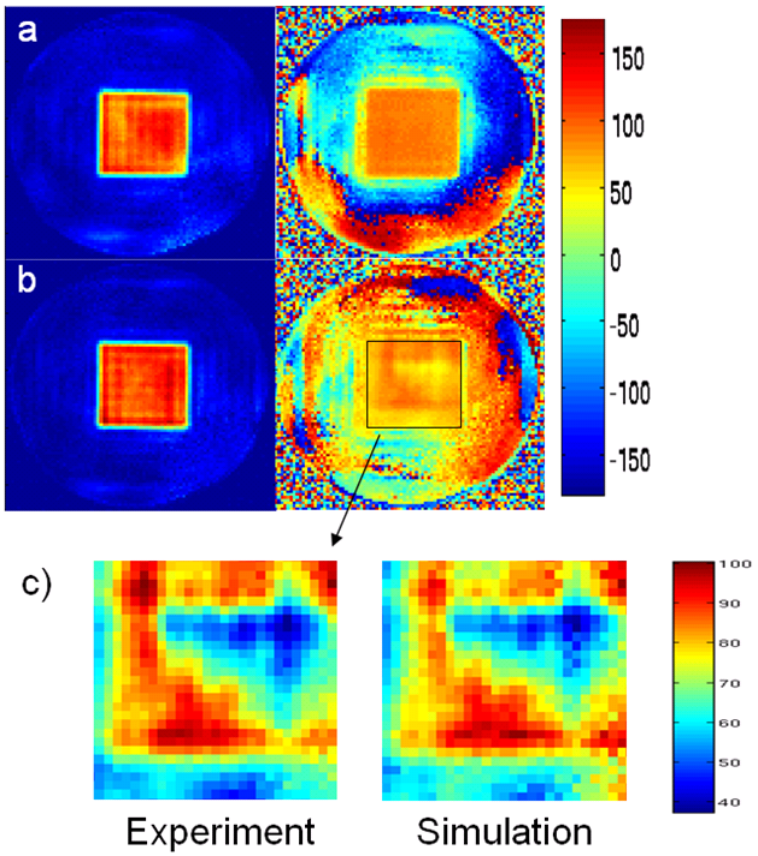

Figure 36: Experimental square-target excitation for a fixed value of Tikhonov regularization parameter ($\beta = 1.5$), magnitude (left) and phase (right) by, **a)** conventional least-squares optimization, and **b)** by magnitude least squares. Larger variation of spatial phase profile is observed for the magnitude least squares design as expected. Additionally, the MLS design yields better target excitation and background suppression within the phantom outside the target square. Panel **c)** shows a zoomed region of the phase profile from the MLS design, and shows the high degree of similarity between experimental (left) and simulation results (right).

Spoke Trajectory

The 4-spokes pulse design yielded 2.86 ms long pulses. Figure 37a)&b) shows a comparison between the best (lowest RMMSE) uniform in-plane slice-selective profiles achieved using the LS (a) and the MLS (b) design. The magnitude profile resulting from the MLS design is significantly more uniform with a reduction in RMMSE of 51% compared to the LS design (the simulation predicted a 66% reduction). To further quantify the performance, we note that with MLS design, 96.4 % of the data deviate by less than 10% from the flat target profile and 100% deviate by less than 20%, compare to 82% and 97% with the LS design. Figure 37c) shows the plot of the normalized RMMSE vs. the normalized RF voltage norm across all eight channels ($\|b\|_2$) for six different settings of the Tikhonov regularization parameter (β). The average drop in RMMSE over the six data points is 47% for simulation data and 34% for experimental data. The average integrated RF power drop is 49% and the peak RF power drop is 53%.

Since we only need to calculate the spokes coefficient during the RF design, the MLS computation time (3 GHz, 64-bit Xenon processor, Linux operating system), for the spoke-based designs is much less compare to the spiral-based design, with calculation time of less than 1 minutes for any of the Tikhonov regularization parameter values.

Similar to Figure 36, Figure 38 illustrates the tradeoff between an increase in spatial phase variation for lower magnitude mean squared error and reduced RF power with MLS optimization compared conventional LS designs for the spoke design. Again in row c), the observed phase closely resemble the simulation; with small and smoothly varying variation, resulting in negligible intra-voxel dephasing.

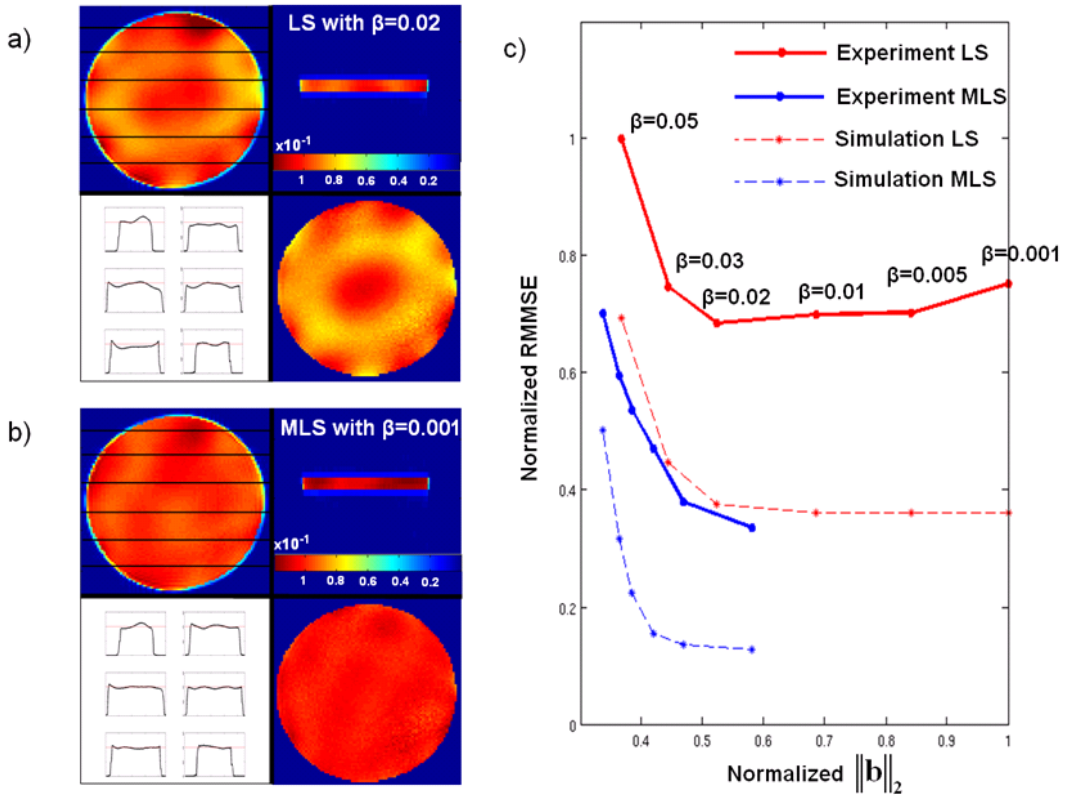

Figure 37**: a) & b)** Acquired data and simulation results for a 4-Spoke excitation by conventional least-squares (a), and magnitude least squares (b), for the Tikhonov regularization parameter pair that resulted in the lowest experimental RMMSE. In each panel, the top row shows the experimental in-plane and through-slice profiles, while the lower right image shows the predicted profile based on a Bloch-equation simulation of the RF waveforms. The bottom left figure in each panel shows several sections through the in-plane profile. **c)** L-curve plot of the normalized RMMSE vs. RF voltage norm across all 8 channels ($\|b\|_2$), for six different settings of the Tikhonov regularization parameter.

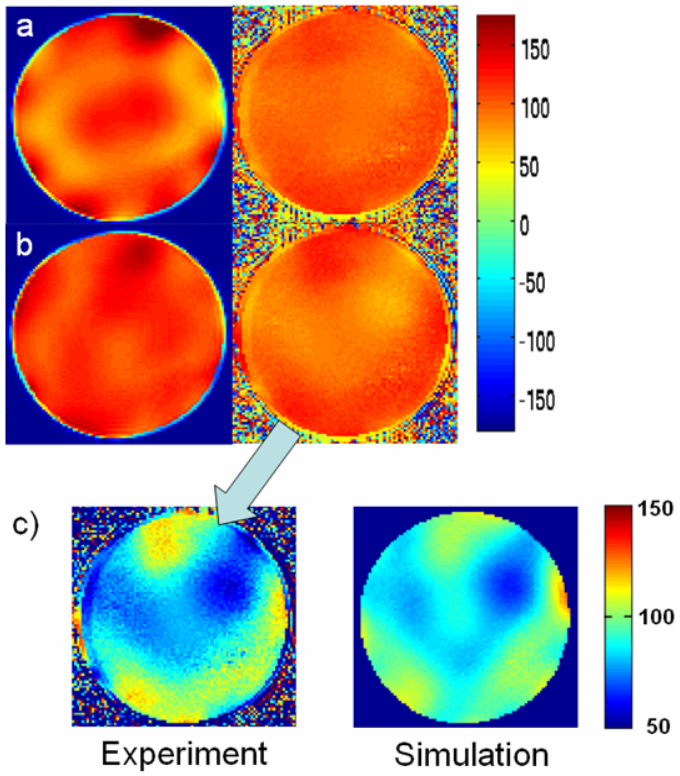

Figure 38: Experimental magnitude (left) and phase (right) results for a 4-Spokes excitation by conventional least-squares (a), and magnitude least squares (b), for the Tikhonov regularization parameter pair that resulted in the lowest experimental RMMSE. Larger variation of spatial phase profile is observed for the magnitude least squares design as expected. Additionally, the MLS design yields a much more uniform magnitude profile. Panel **c)** shows a zoomed phase scaling version of the phase profile from the MLS design, and shows the high degree of similarity between experimental (left) and simulation results (right).

4.5 Discussion

We have successfully developed, implemented, and demonstrated a design algorithm for multi-channel parallel excitation that minimizes the deviation in the magnitude of the transverse magnetization profile from its target and reduces the pulse power required. This improved performance is achieved at the cost of increased spatial phase variation, under the control of the designer, and resulted here in negligible intra-voxel dephasing. Experimental results at 7T matched well with the simulation; showing significantly improved performance compared to conventional least-squares design where the phase target is explicitly constrained.

For the 2D spiral design, the experimental RMMSE matched well with the predicted values from the simulated data for both LS and MLS methods (Figure 35b). However, at smaller Tikhonov regularization parameter values (β), the experimental RMMSE starts to deviate more from the prediction. We explain this phenomenon by observing that for low β values more cancellations among profiles are required to achieve a better excitation (as can be seen from the increased in the required RF power). This large amount of required cancellations can result in an amplification of noise in the excitation profile from e.g. noise in the B1 maps, causing a larger RMMSE than expected. This was observed for both the LS and MLS methods where the experimental excitation profiles at β = 0.3 contains more edge artifacts, when compare to the excitation profiles of higher β values.

For the spoke design, in Figure 37c) the experimental RMMSE follows a similar trend to that of the simulation results, although with higher error values. In our simulation studies, we found that the spoke design is much more susceptible to B_0 off-resonance and eddy current effects when compared to the spiral design. This vulnerability is likely to be part of the cause for the increased error. Our future work includes the exact quantification of the source of this error and possibly the design for a correction method.

Also in Figure 37c), an increase in error at lower Tikhonov regularization parameter value (β) can be observed in the LS experimental result. In the simulation result over the same β values range, a very small reduction in error for a much higher required RF power can be observed. This suggests that, at lower β values, a significantly larger amount of profile cancellation is required during the excitation. In the experiment, this causes large noise amplification which resulted in the increased error.

In comparing the spiral and the spoke excitations, the improvement gained from using the MLS design in the spoke case is much more prominent. This is to be expected, since the spokes trajectory, which is just a few delta points in k_x-k_y, allows for much less control of the in-plane excitation profile when compared to the spiral trajectory. Therefore, the gain from relaxing the in-plane excitation phase constrain for the spoke design should be much larger.

This work is a novel study of the possible benefits from relaxing the phase constraint in parallel excitation design. To relax the phase constraint, the design problem was mapped to an MLS optimization. Because of the non-convex nature of this optimization, currently no method solves the problem with a guaranteed global optimality of the solution. We chose to extend the local variable exchange method (65) to solve the problem because it allows us to impose the smoothly varying phase constraint. Other methods exist for solving MLS problems, including the relaxed semi-definite programming method (65). Future work includes an exploration of alternate means to solve the posed MLS problem for parallel RF excitation.

This work demonstrated the benefit of MLS optimization in parallel excitation. A water phantom with large B_1 profile variation, similar to that observed in human imaging at high field, was used in our experimental set up. Given the significant benefit achieved with the MLS optimization, particularly for the mitigation of the inhomogeneous B_1 profile though the use of the spoke trajectory excitation, we expect the MLS optimization to play an important role in parallel excitation design for human imaging at high field.

Chapter 5

In-vivo Parallel Excitation at 7 Tesla

5.1 Introduction

In this work, parallel excitations were performed on both head-shape water phantom and in vivo human studies at 7T. Slice-selective B_1^+ mitigated excitations were created and validated via a 16-element degenerate stripline array coil driven with a butler matrix to utilize the 8 most favorable birdcage modes. RF and gradient excitation waveforms were designed via MLS optimization, and a spokes' placement optimization algorithm. With this design method, optimized parallel excitation waveforms for human B_1^+ mitigation were only 67% longer than conventional single-channel sinc-based excitation. A comparison of B_1^+ mitigation performance by parallel transmission and currently available techniques is provided, demonstrating the superior performance achieved by parallel transmission.

5.2 Methods

Human subjects

Six healthy volunteers (20-35 years old, 4 males and 2 females) were recruited from the community to serve as subjects for this study. All protocols were approved by the local IRB review committee.

System Hardware

All experiments were run on Siemens 7T Magnetom scanner (Erlangen, Germany). The two primary RF hardware components related to this study were a 16-channel stripline transmit-receive (Tx/Rx) degenerate birdcage coil array (31) and a 8x16-channel butler matrix described in Chapter 3. The butler matrix was used to drive the 8 optimal birdcage transmit modes from the 16 channel coil, and serves to make the best use of the RF excitation system, which has only 8 RF power amplifiers. Signal was received through mode-1 birdcage on the 16 receive channels of the array.

A head-shaped water phantom filled with doped water containing 1.25 g/L of nickel sulfate and 5 g/L of sodium chloride (T_1~500 ms), was used for initial measurements and demonstration of B_1^+ mitigation. Figure39 a) shows the TX-RX mode-1 birdcage image of this water phantom. The peak-to-trough signal ratio in this image is very large, approximately 15. Also shown are the separate estimates of the TX and RX profiles, with the TX magnitude signal ratio of 6.8 from maximum to minimum within the slice. This variation is about twice the maximum range we observed for the human studies. Figure39 b) shows the relevant profiles for a human brain (subject 1).

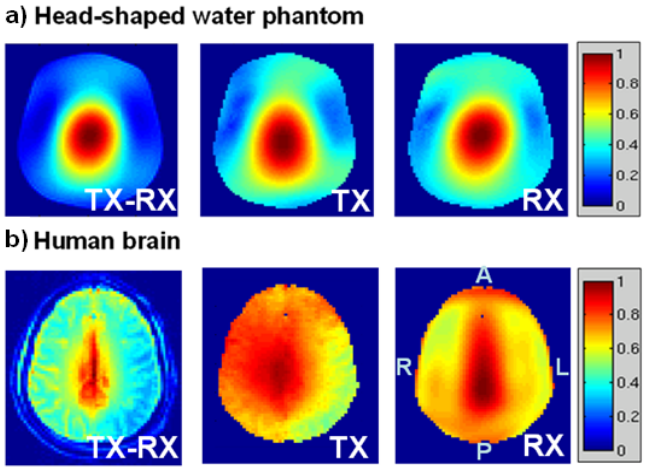

Figure 39: a) Profiles for combined TX-RX, along with estimates of the separate TX and RX of the mode-1 birdcage of the coil for a head shaped phantom, and b) human brain (subject 1).

Specific Absorption Rate Monitoring

The RF power was monitored in real time for each channel and utilized a 10 second and 6 minute average. For determining the SAR limit, a very conservative estimate was used. Based on the work by Collins et al (68) analyzing the worst case scenario for a similar 16-element stripline array, we utilized a local 10g SAR to average SAR ratio of 60. To assess this, Collins and colleagues determined the worst case ratio of local SAR to average SAR using Finite Difference Time Domain (FDTD) generated field maps in a human head model for a 16-element stripline coil. Given that the International Electrotechnical Commission (IEC) allows an average SAR of 3.2W/kg and local SAR of 10W/kg (a local to average ratio of 3.125, well below the estimated worst-case of 60) these results make it clear that local SAR is the limiting concern. Based on the worst-case local to average ratio of 60 and the IEC limit of 10W/kg for local SAR, we de-rated the allowable average SAR to 0.167W/kg. Using a 5 kg head mass, this gives an allowable average total power limit of 0.83W.

B_1^+ mapping

The B_1^+ mapping method presented in Chapter 3 was used. Examples of transmit profiles derived by this method for the head-shaped phantom and a human subject are shown in Figure 40. In all acquisitions for B_1^+ mapping, standard 2D imaging (gradient-recalled echo sequence) was used with 80x80 pixel grid in x,y at 2.5 x 2.5 mm^2 resolution over a 20-cm FOV in-plane (TE/BW = 5ms, 260 Hz/pixel).

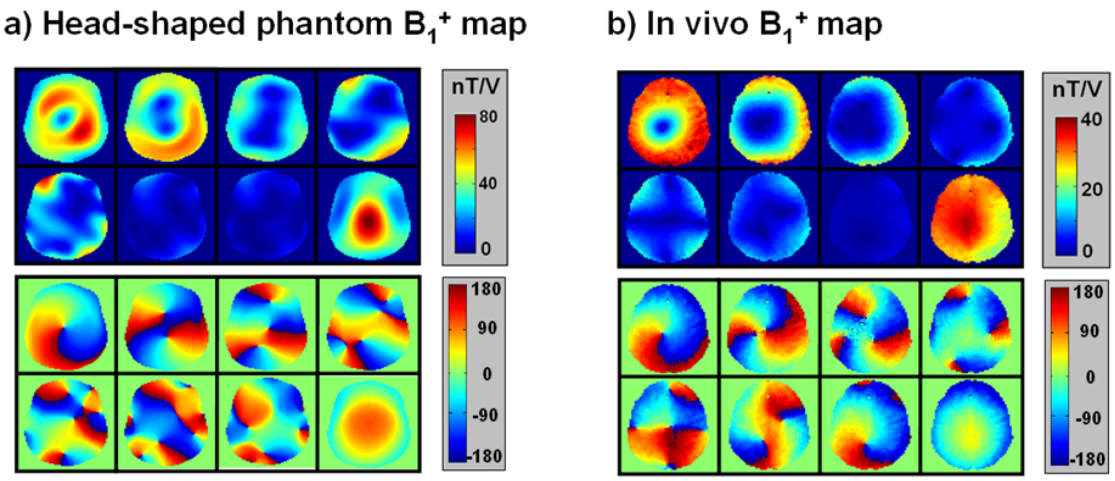

Figure 40: Magnitude (top) and phase (bottom) B_1^+ maps of the 8 optimal modes for a) the head-shaped phantom, and b) an axial section in human brain (subject 1).

RF Design

We based our RF design on the magnitude least squares (MLS) optimization method presented in the previous chapter along with the incorporation of B_0 inhomogeneity correction method from Chapter 2. Furthermore, the spoke placement in the k-space excitation trajectory was optimized to provide additional improvement to the excitation performance. For this optimization, the spokes were constrained to be symmetric around the origin in the (kx,ky) plane, and were optimized over a grid defined by 0º, 45º, 90º, and 135º angles, and different separation values ($\Delta k = 1/FOV$), with the FOV value ranging from 16 to 36 cm in incremental step of 2 cm. Examples of the optimized spoke-based k-space excitation trajectory for the phantom and the in vivo studies are shown in Figure 41.

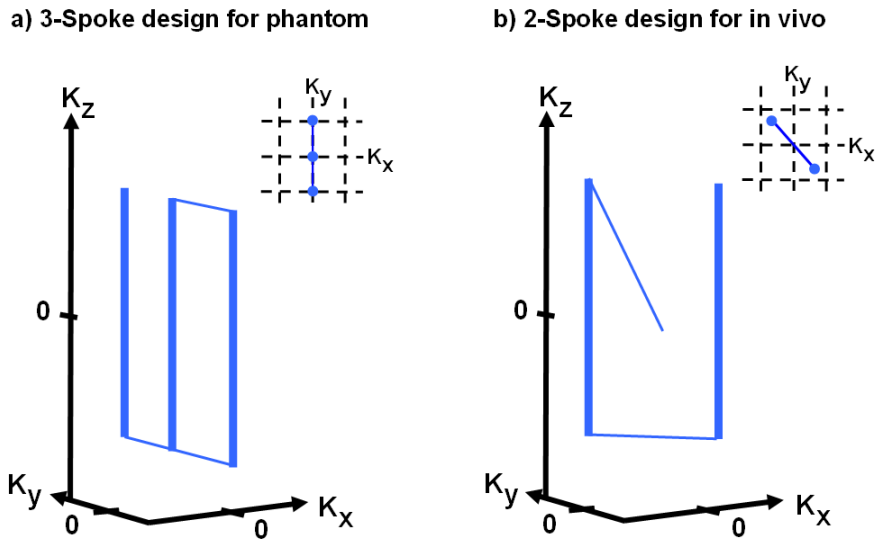

Figure 41: The optimized three (a) and two-spoke (b) k-space trajectories for the pulse design in the head-shaped phantom and human excitation experiment respectively. The optimized two-spoke placements in (k_x,k_y) for the in the in vivo experiments varied slightly from subject to subject, but in all cases were two-spoke designs.

In the RF design, a slice-selective spoke excitation with time-bandwidth-product equal to 4 was used for the sinc sub-pulses. For our initial phantom work where B_1^+ inhomogeneity was very severe, a three-spoke excitation trajectory was employed. Slice-selective specifications of 1-cm thickness, along with maximum gradient amplitude constrain of 20 mT/m, and slew rate constrain of 150 T/m/s were used. For the *in vivo* studies, a two-spoke excitation trajectory was used with a slice-selective specification of 0.5-cm thickness, maximum gradient amplitude constrain of 30 mT/m, and slew rate constrain of 150 T/m/s.

RF shimming design used for comparison in both the phantom and *in vivo* experiments was cast as a single-spoke RF design at the (k_x,k_y)-space origin with an MLS optimality criterion. The pulse duration quoted in this work includes the duration of the gradient rephaser applied after the excitation to properly return excitation trajectory to k-space origin. The predicted magnetization patterns were calculated using a Bloch equation simulation of the parallel RF excitation.

Experiments and Comparisons

For experimental verification, the spoke excitations were designed and tested on both a head-shaped phantom with severe B_1^+ inhomogeneity and on six human subjects with axial slice selection at six different superior/inferior (S/I) axial positions. In addition, for all experiments, excitation via mode-1 birdcage transmission and RF shimming were also acquired for comparison. For the head-shaped-phantom experiment, data were also collected to compare the performance of the conventional least-squares (LS) vs. the MLS design of the spoke-based RF pulses. The RF excitation pulses were adjusted so that for all the experiments the target flip angle was 5º.

The excitations were imaged with a standard 2D (gradient-recalled echo) sequence with matrix = 80x80, FOV = 20 x 20 cm^2, voxel resolution = 2.5 x 2.5mm^2, TR/TE/BW = 1s/5ms/260 Hz/pixel, where the combination of relatively long TR and low-flip-angle excitations resulted in proton-density weighted images. The flip-angle maps of the excitations were inferred from the proton-density images by dividing out the estimated density-weighted receive profile[1], $\widetilde{\rho}(x,y)\widetilde{RX}(x,y)$, and taking inverse sine.

Standard deviation and uniformity threshold levels were used for quantitative comparison between mode-1 birdcage, RF shimming and spoke excitation. For a fair comparison of the standard deviation, the excitation flip-angle profiles were all scaled to have a mean value of 1.0 before the standard deviation was calculated (i.e. normalized standard deviation). The uniformity threshold levels used in the comparisons, '<10% dev' and '<20% dev', are defined as the percentage of the excitation flip-angle profile that deviate less than +/- 10% and +/-20% from the mean flip-angle value. The pixel set used in these comparisons is defined by the mask used in the generation of the B_1^+ maps. For the water phantom, this mask is generated by applying intensity thresholding to the birdcage Tx-Rx image to exclude the region beyond the phantom edge as well as partial-volume pixels in the periphery of the phantom. For the *in vivo* cases, the mask is also

[1] As outlined in Chapter 3, an estimate of the density-weighted receive profile is obtained as a by product in the B_1^+ profile estimation.

generated using the birdcage Tx-Rx image. However, an additional refinement step of manual "skull stripping" was applied before the mask generation via intensity thresholding. Figure 40b&c show the birdcage Tx-Rx image without masking and the Tx and Rx profiles with masking for both phantom and *in vivo* cases.

To demonstrate slice selection fidelity of the spoke excitation, a 3D readout was also acquired in one of the *in vivo* study (TE/TR/flip = 5ms/100ms/5°, 26 slices, FOV = 20 x 20 x 2.6 cm^3, resolution = 2.5 x 2.5 x 1 mm^3).

5.3 Results

Head-shaped water phantom.

The head-shaped water phantom used for these experiments poses a very challenging B_1^+ mitigation task due to the severity of the transmit profile variation with a peak-to-valley magnitude variation of 6.8-to-1 in B_1^+ at an approximately central axial slice through the phantom. The conventional, sinc-based mode-1 birdcage excitation demonstrates the consequences of this severe B_1^+ inhomogeneity as a highly non-uniform in-plane flip-angle (Figure 42a), while RF shimming (single-spoke at DC) is able to partly mitigate the B_1^+ variation ((Figure 42b). We note that the mode selected by the RF shimming optimization looks like the 1st gradient mode (the first mode in Figure 40a), with some additional improvements by mixing in contributions from other modes. It is interesting to note that the mode-1 (the last mode in Figure 40a) in this case is more inhomogeneous than the 1st gradient mode as measured by the standard deviation of the magnitude across the FOX.

The partial mitigation of the RF shimming is dramatically improved by adding another two spokes to the excitation as is clear from Figure 42c. Visually, based on the images and line profiles, the B_1^+ mitigation of the spokes is excellent. Also quantitatively, based on the standard deviation across the FOX and the 10% and 20% deviation brackets, the three-spoke mitigation significantly outperforms RF shimming. The

tradeoff in pulse duration is from 1 ms for RF shimming to 2.4 ms for the 3-spoke design. The optimized placement of the spokes yielded a separation of 1/20 cm^{-1}, at an angle of 90° (i.e. along k_y), as shown in Figure 41a.

The same head-shaped phantom was used to compare the performance of three-spoke B_1^+ mitigation designed with conventional LS and MLS. The LS design strives to excite the FOX with a uniform phase and magnitude, while the MLS allows slowly-varying spatial phase of the excitation in order to improve on the magnitude profile uniformity. Clearly, as seen in Figure 43, this relaxation of the phase constraint by the MLS spoke design yields a very favorable tradeoff for the B_1^+ mitigation. Further, as seen in Figure 44, this excitation phase variation in the MLS pulse is negligible compared to the B_0 inhomogeneity-induced phase accrual at TE=5ms at 7T. The spatial excitation phase is very slowly varying, is far from introducing intra-voxel dephasing, and is much smaller than the accrued B_0 inhomogeneity-induced phase at the gradient-recalled echo time of 5 ms for this phantom. The displayed phase of the experimental result is calculated from the phase at TE=5ms by unwinding the effect due to B_0 inhomogeneity, $e^{-iB_0(x,y)\cdot TE_{eff}}$, where TE_{eff} is the time from center of excitation k-space to center of readout k-space.

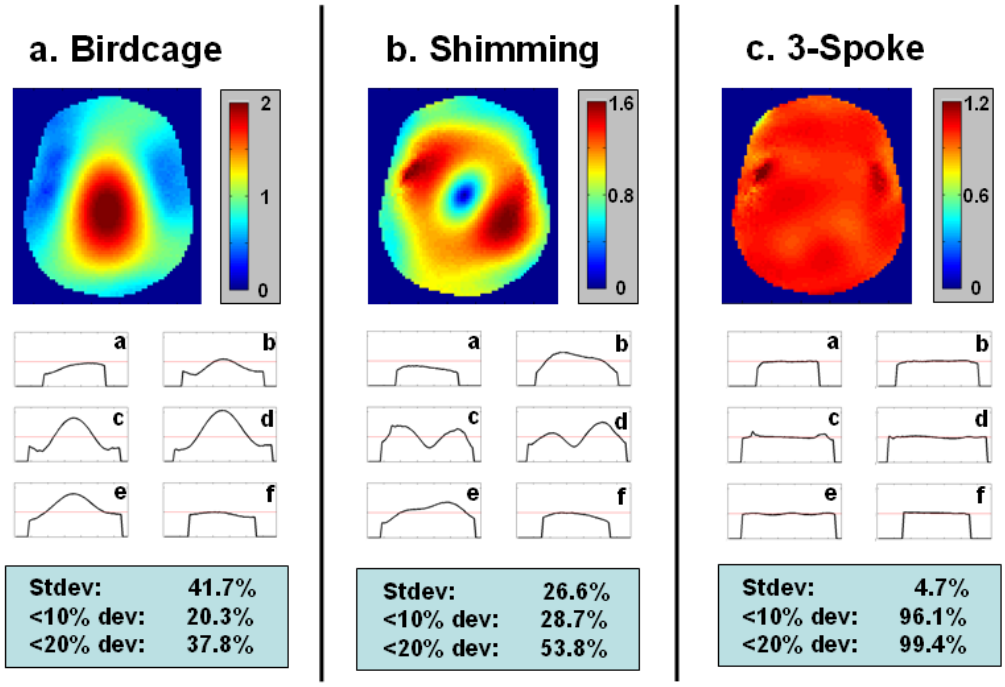

Figure 42: Head-shaped water phantom B_1^+ mitigation. Flip-angle maps and line profiles for: a) Birdcage mode with conventional 1-ms long sinc slice-selective excitation, demonstrating a 1:6.8 magnitude variation within the field-of-excitation (FOX); b) RF shimming, 1 ms-long pulse, demonstrating a substantial residual flip-angle inhomogeneity as measured by the residual standard deviation and threshold metrics; and, c) three-spoke MLS, slice-selective 2.4-ms long pulse, demonstrating excellent mitigation of the B_1^+ inhomogeneity.

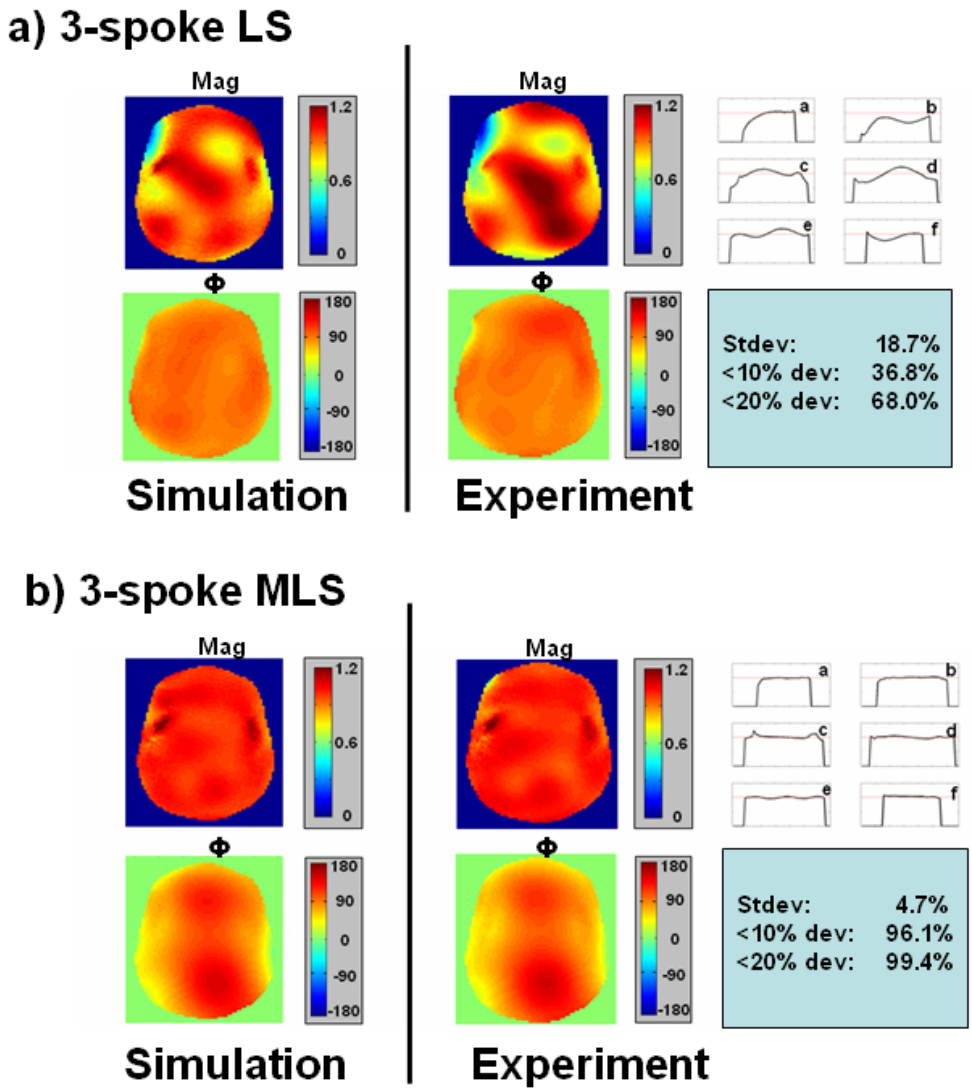

Figure 43: Comparison of B_1^+ mitigation by a) a least-squares, and b) a magnitude-least-squares 3-spoke RF design with the same k-space trajectory (2.4 ms) and pulse shape (sinc, time-bandwidth product=4) as demonstrated on a head-shaped water phantom with substantial Tx inhomogeneity. On the left is a Bloch simulation of the magnitude and phase profiles, on the right are experimental results with line profiles through the magnitude image. Also shown, bottom right, is the excitation phase profile.

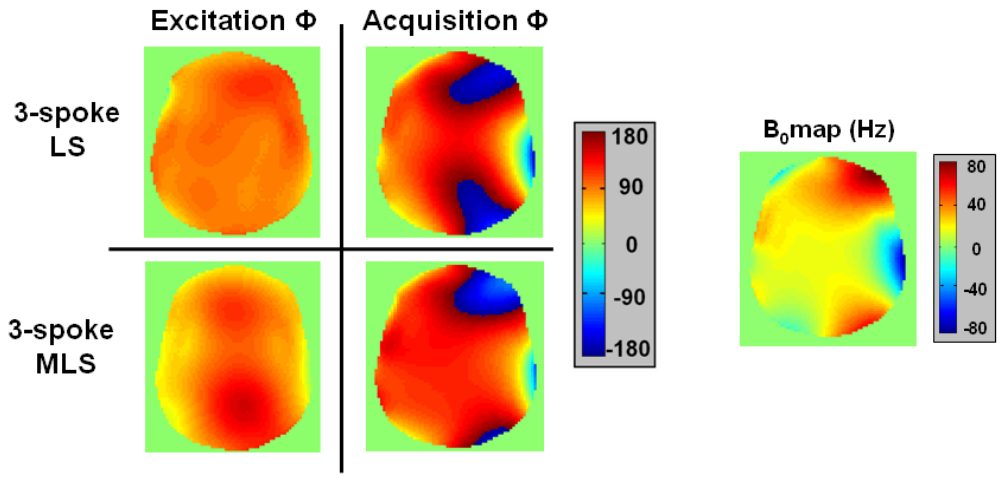

Figure 44: Comparison of phase due to the excitation only (left) and phase measured in a gradient echo at TE=5ms, which also includes the accrual of phase due to B_0 inhomogeneity (center). The $B_0(x,y)$ term is according to a separately estimated B_0 fieldmap (right). Clearly, the excitation phase variation resulting from the MLS design is very small compared to the accrued phase due to B_0 inhomogeneity at TE=5ms, and is slowly varying over the FOX, and thus does not introduce any intra-voxel dephasing.

B_1^+ mitigation in vivo.

Based on the successful mitigation of the significant B_1^+ inhomogeneity in the water phantom, we ran *in vivo* experiments on six human subjects to demonstrate flip-angle correction for brain imaging in the presence of inhomogeneous B_1^+ and B_0. Figure 45 and Figure 46 compare the excitation performance of mode-1 birdcage (top row), RF shimming (center row), and two-spoke excitation pulses (bottom row) for two of the six subjects. The results in Figure 45 are for subject 1 who exhibits an average amount of B_1^+ variation in the birdcage excitation, as measured by the standard deviation (σ), when compared to the other subjects. The results in Figure 46 are for subject 5 who exhibits the largest amount of B_1^+ variation in the birdcage excitation. In each figure, on the left of each row is the in-plane image of the excited slice after the removal of the received profile (which is estimated here as the 10th-order polynomial fit of the density-weighted receive profile). On the right of each row is the flip-angle map estimate, along with line profile plots. In both Figure 45 and Figure 46, RF shimming is more homogenous than the birdcage excitation, but still suffers from significant residual flip-angle inhomogeneity, whereas the two-spoke excitation provides excellent mitigation. It is noted that small amount of residual anatomy exists in the flip-angle map estimates, which most likely arises from small subject movement between the time of density-weighted receive profile estimation and the imaging of the mitigated excitation. Nonetheless, given the considerable improvement in the mitigation performance by the spoke excitation, this minor estimation artifact does not affect the overall conclusion that the two-spoke, slice-selective parallel RF excitation yields very effective flip-angle mitigation.

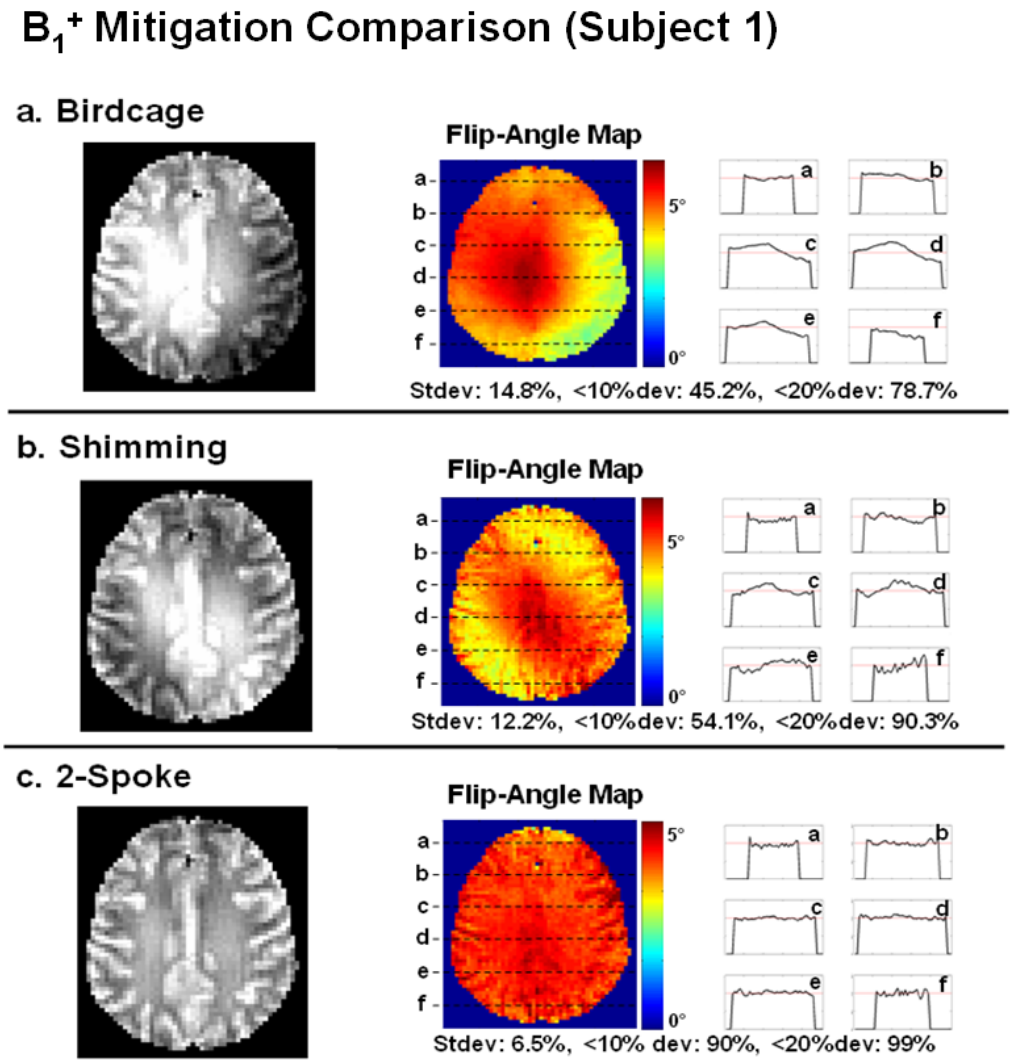

Figure 45: B_1^+ mitigation comparison for subject 1. The comparison includes slice selection based on mode-1 birdcage (top row), RF shimming (center row), and two-spoke (bottom row) excitation pulses. On the left of each row is the in-plane image of the excited slice after the removal of the receive profile. On the right is the flip-angle map estimate, along with the line profile plots.

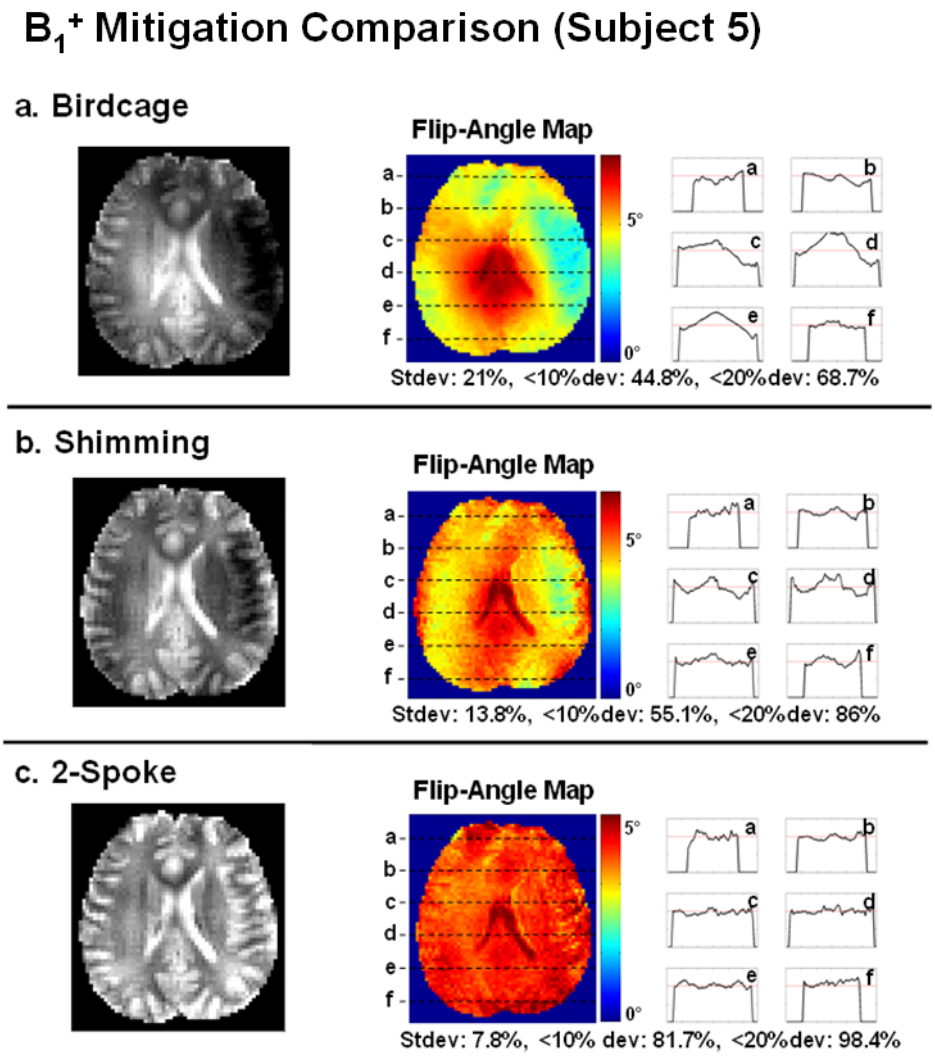

Figure 46: B_1^+ mitigation comparison for subject 5, who has the most severe B_1^+ variation (in the mode-1 birdcage excitation) out of all the six subjects.

Table 1 tabulates the standard deviation and pixel fractions for 10% and 20% deviation of the transmit profile for birdcage, RF shimming, and two-spoke excitation for all 6 subjects. The trend across the data is very clear. The birdcage excitation is by far the most inhomogeneous, the RF shimming provides some improvement, and the two-spoke excitation is the most homogenous and reliable excitation for slice-selective B_1^+ mitigation. The associated tradeoff in pulse duration is 2.29 ms for two-spoke excitation vs. 1.37 ms for birdcage and RF shimming excitation. Note that the increase in pulse duration of the two-spoke excitation over the birdcage and RF shimming excitation is 67% rather than 100%, since the two-spoke excitation utilizes a single gradient rephasing lobe identical to one used in the birdcage and RF shimming excitation.

For the *in vivo* parallel RF pulse design, the optimal spoke placement varies dramatically between subjects and does not seem to be intuitive. When compared to the default placement (assumed here to be at $\Delta k = 1/20$ cm^{-1}, along the k_x-axis), the optimal spoke placement provides significant improvement in excitation performance. Based on simulation results obtained for the six human subjects, the average reduction in excitation error (measured here as the standard deviation) is 10.5%, and the average reduction in RF pulse energy and peak power are 9% and 3.4% respectively.

Table 2 tabulates the total energy and peak power of RF pulses used for birdcage, RF shimming, and two-spoke excitation for all 6 subjects. To provide a fairer comparison, the longer pulse duration of the two-spoke excitation is accounted for. Namely, the RF energy and peak power calculation for the birdcage and RF shimming excitation are performed for an excitation that concatenate two consecutive, identical sinc RF excitations at half the RF amplitude of the actual single sinc RF pulse used in the experiments. This procedure reduces the RF energy of the birdcage and RF shimming by a factor of 2 and the peak power by a factor of 4, and yields a normalized comparison in terms of pulse duration. Based on this normalization, the RF pulse energy of the 2-spoke excitation is approximately double that of the birdcage excitation and is slightly lower

than that of the RF shimming. On the other hand, the peak-power values of all the three excitations are similar.

	σ(%)			<10%			<20%		
	BC	Shim	Spokes	BC	Shim	Spokes	BC	Shim	Spokes
Subject 1	14.8	12.2	6.5	45.2	54.1	90.1	78.7	90.3	99
Subject 2	12.4	11.4	6.6	54.8	60.9	91.3	88.9	93.1	98.8
Subject 3	19.8	17.5	9.3	39.1	38.6	77.7	66.8	84.5	96
Subject 4	15.1	12.9	7.3	52.2	59.4	87.1	80.6	88.5	98.2
Subject 5	21	13.8	7.8	44.8	55.1	81.7	68.7	86	98.4
Subject 6	16.9	11.7	8.1	42.3	63.4	83	76.4	91	96.9
Avg ± Stdev	16.7 ± 3.2	13.3 ± 2.3	7.6 ± 1.0	46.4 ± 6.0	55.3 ± 8.9	85.2 ± 5.3	76.7 ± 8.1	88.9 ± 3.2	97.9 ± 1.2

Table 1: Standard deviation and pixel fractions for 10% and 20% deviation of the flip-angle map of birdcage, RF Shimming, and two-spoke excitation for all six subjects.

	Total Energy (mJ)			**Peak Power (W)**		
	BC	**Shim**	**Spokes**	**BC**	**Shim**	**Spokes**
Subject 1	**7.68**	**13.8**	**13.3**	**30.2**	**25.9**	**30.4**
Subject 2	**7.35**	**12**	**10.4**	**28.8**	**26.3**	**23.9**
Subject 3	**10.8**	**29.7**	**18**	**42.3**	**39.6**	**38.7**
Subject 4	**7.79**	**17.4**	**16.2**	**30.4**	**25.9**	**24.5**
Subject 5	**10.7**	**24.8**	**21.8**	**42.1**	**47.4**	**32**
Subject 6	**8.65**	**14.7**	**15.8**	**33.6**	**30.8**	**46.1**
Avg ± Stdev	**8.83 ± 1.5**	**18.7 ± 7.0**	**15.9 ± 3.9**	**34.6 ± 6.1**	**32.7 ± 9.0**	**32.6 ± 8.6**

Table 2: Total RF energy and RF peak power for birdcage, RF Shimming, and two-spoke excitation pulses for all six subjects. The reported energy and power are for excitation pulses of normalized duration.

Figure 47 shows the slice profile performance of the two-spoke excitation on a human subject (subject 4). In Figure 47-a, the experimental slice profile is plotted as circles, along with the predicted profile by simulation which is shown as a solid line. Each data point along the profile represents the average in-plane intensity at that particular z-location. Good agreement between experiment and prediction can be observed, with excellent slice selection behavior. In Figure 47-b are the in-plane images (after compensating for the effect of the receive profile) of 1-mm separation along z, over a 1-cm range around the 0.5 cm excited slice. Good slice selection and B_1^+ mitigation performance can be observed.

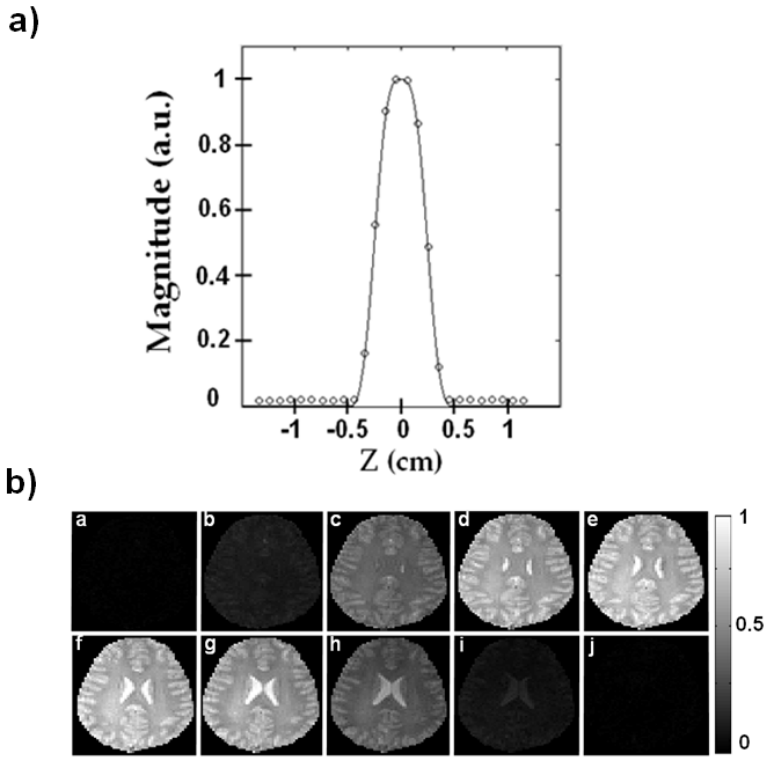

Figure 47: Two-spoke excitation for subject 4 with a 3D readout. a) Slice profile plot, where the solid line represents the predicted profile and the circles represent the experimental data. Each data point along the slice profile represents the average in-plane intensity at that particular z-location. b) In-plane images (a)-(j), at 1-mm separation along z, over a 1-cm range around the 0.5-cm excited slice.

5.4 Discussion

In this work we have successfully demonstrated mitigation of severe B_1^+ inhomogeneity at 7T, for a head-shaped water phantom and on six human subjects. The phantom result is interesting in that the B_1^+ inhomogeneity is more than twice as severe as we observed in any of the six subjects. Correspondingly, a three-spoke excitation was used for the phantom excitation, while a two-spoke design was adequate *in vivo*. The phantom finding suggests that at even higher fields, where the B_1^+ inhomogeneity *in vivo* becomes more pronounced than at 7T, spoke-based RF design is viable with a very high degree of flip-angle uniformity and short pulse duration.

A comparison of peak power and total energy of the RF pulses used for birdcage, RF shimming, and spoke excitation was provided in Table 2. This comparison points to similarities in peak-power and significant increases in pulse energy for RF shimming and spokes excitation when compared to conventional birdcage transmission. However, this work does not address a direct SAR comparison between the three methods. SAR calculation is a topic of an ongoing work, which will be keyed to clinical application of parallel transmission.

A limitation of the current transmit coil array, which is built around a cylindrical ring with local coil elements placed horizontally adjacent to each other, is that it is primarily fit for transversal acceleration and hence mitigation in the axial plane. Future work on coil development will address this point and extend the coil design to allow for longitudinal profile variation between the coil elements, and therefore longitudinal acceleration. We expect that the presented methodology for slice-selective excitation with B_1^+ mitigation will hold for sagittal, coronal and generally oblique scan planes beyond the currently presented axial demonstrations.

As part of the RF design method used in this work, a simple and fast k-space excitation trajectory optimization was employed to provide significant improvement in the excitation performance. Based on the performance of a Linux Intel® Xeon 3 GHz

server, in Matlab, this optimization process can be performed in ~50 seconds. We note that the optimization procedure can easily be made more sophisticated by evaluating the optimal spoke placement on a finer grid, but we suggest limiting the search to symmetric placement of spokes in (k_x,k_y) for these simple designs to maintain them within a regime compatible with the linear class of large tip angle pulses proposed by Pauly et al (69) and used for parallel transmit work by Xu et al (70). Such an approach would simplify the extension to larger flip angles.

5.5 Conclusion

Slice-selective RF waveforms that mitigate severe B_1^+ inhomogeneity at 7 Tesla were designed and demonstrated for parallel excitation in phantom and in six human subjects. This work demonstrates that slice-selective excitations with parallel RF systems offer the means to implement slice selection with spatially uniform flip-angle at high field strengths with only a small pulse-duration penalty.

Chapter 6

Spectral-Spatial Parallel Excitation

6.1 Introduction

Previous works on parallel excitation method have been limited to the design of water-only (i.e. single frequency) excitation profiles, resulting in RF pulses with a narrow bandwidth characteristic. This narrow-band property was apparent in Chapter 2, where it was shown that B_0 inhomogeneity, i.e. variation in spin frequency, in standard in-vivo imaging condition at 3T can have a detrimental effect on the excitation profile if B_0 field map information was not incorporated into the RF design.

The narrow-band nature of spatially tailored excitation pulses complicates their use in applications where excitation over a spectral band is required. An example is in Chemical shift imaging (CSI) which is an imaging technique that is used to obtain quantification of brain metabolites, important in diagnosis of neuro-degenerative diseases. CSI relies on signal generation from metabolites which similar to water contain hydrogen nuclei with a magnetic dipole moment. However, due to differences in chemical environment, these dipole moments exhibit spin frequencies that are slightly different than one observed in water. Therefore to generate signal by exciting these dipole moments, the RF pulse must performance well not only at a single frequency but over a spectral band.

Chemical shift imaging benefits from high B_0 field strength through higher SNR, larger frequency spread between metabolites allowing for easier separation of

metabolites' signals, and weaker spin coupling. However, the detrimental effects of B_1^+ inhomogeneities at high-field pose significant problems, and in order to realize the benefits of high-field to CSI, broadband RF excitations that mitigate B_1^+ inhomogeneity and achieve uniform flip angle over both the spatial field of view and a specified spectral bandwidth are necessary. This additional bandwidth constraint over conventional imaging presents a substantial challenge for current parallel RF design methods which, to date, have not explicitly incorporated this constraint into the design problem.

This work outlines a design method for a general parallel spectral-spatial excitation that achieves a target-error minimization simultaneously over a bandwidth of frequencies and a specified spatial-domain. The method is based on extending the spatial domain formulation with Magnitude Least Squares (MLS) optimization presented in Chapter 4. In demonstrating the capability of this new technique, a uniform wideband slice-selective excitation was designed using the spoke-based trajectories to mitigate the extensive B_1^+ inhomogeneity present in a head-sized water phantom at 7T over a 600 Hz spectral bandwidth. The performance of the resulting 1.76-ms duration, 5-cm thick slab-selective excitation RF pulse was validated using an 8-channel transmit array system on a 7T human MRI scanner.

6.2 Theory

The spectral-spatial excitation design is a direct extension of the spatial-domain approach with MLS optimization presented in Chapter 4. To design for spatial excitation profile ($\boldsymbol{m}$) at a set of N different frequencies, we extend the set of equations and concatenate the $\boldsymbol{m}$ vector and the $\boldsymbol{A}$ matrix corresponding to the N design frequencies (1, 2, ….., N) to form:

Equation 27

$$\begin{bmatrix} \overline{m}_{Freq1} \\ \overline{m}_{Freq2} \\ \vdots \\ \overline{m}_{FreqN} \end{bmatrix} = \begin{bmatrix} [A_{Freq1}] \\ [A_{Freq2}] \\ \vdots \\ [A_{FreqN}] \end{bmatrix} \times \overline{b}$$

The concatenated equation can then be solved, as before, via MLS optimization.

The MLS optimization is crucial to the proposed spectral-spatial formulation. Generally the excitation profile at different frequencies will have different spatial phase and the design is generally ill-conditioned as an LS optimization with a fixed, uniform target phase.

For application such as spectroscopic imaging where the reconstructed data are often phased for the purpose of display or quantification, the information about the spatial phase offset due to the excitation is known and can be incorporated as *a priori* information.

For accurate spatial excitation in the presence of B_0 inhomogeniety, B_0 inhomogeneity correction (B_0 tracking) is also incorporated into the RF design by modifying the individual A_{Freq} matrix in Equation 27 to include a measured field map using the procedure presented in Chapter 3.

6.3 Method

System Hardware

The hardware setup here is the same as in Chapter5, with 16-channel stripline transmit-receive (Tx/Rx) coil array and 8x16 Butler matrix (31). All experiments were performed using a 17-cm diameter spherical water phantom.

RF Design

To demonstrate the capability of the proposed spectral-spatial design method, the technique was used with a 4-spoke trajectory to obtain parallel RF pulses that uniformly excite a 5-cm thick slab over a target bandwidth of 600 Hz. The sinc sub-pulses in the RF waveform have time-bandwidth-product of 4, and the gradient trajectory is designed for a maximum gradient amplitude and slew rate limited to 25 mT/m and 150 T/m/s, resulting in pulse duration of 1.76 ms. Flat magnitude target excitation profiles were specified at 3 spatial locations in z (0, ±1.75 cm), to account for the z-variation in the coil transmit profiles. A set of N=5 frequency points, at [-300 150 0 150 300] Hz, were used to create the 600 Hz excitation bandwidth for B_1^+ mitigation. The resulting k-space trajectory, gradient waveforms, and RF waveform for mode 1 are shown in Figure 48.

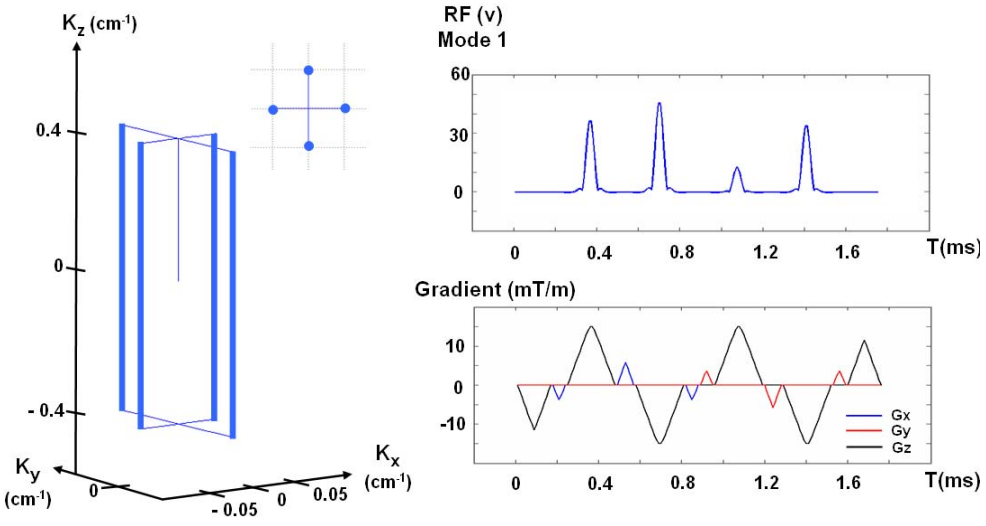

Figure 48: k-space trajectory for the 4-spokes excitation is shown on the left. On the right are the RF waveform for one of the eight transmission modes (mode 1), and the gradient waveforms that were used for the excitation.

B_1^+, B_1^-, and B_0 mapping

The B_1 mapping method presented in Chapter 3 was used. Due to a small but non-negligible B_1 profile variation in the z-direction over the target field-of-excitation (FOX), a set of in-plane B_1 maps were obtained at a set of positions along z. The B_1^+ profiles for

all of the 8 transmit modes were obtained at z = 0, ±1.75 cm, and were used in the RF design. The birdcage receive profiles (B_1^-) were obtained at z = 0, ±1, ±2 cm, and were used in the parallel excitation experiments to divide out the reconstructed images to obtain excitation profiles.

As in Chapter 2, B_0 maps were estimated using image acquisitions at TE1/TE2=5/6 ms. This estimation was performed at 3 slice locations (z = 0, ±1.75 cm), and the resulting maps were incorporated into the pulse design to improve the robustness of the desired excitation, thereby implementing B_0 tracking in the presence of unavoidable B_0 inhomogeneity.

Comparisons and Experiments

To illustrate the benefit of the spectral-spatial design, its excitation performance over a 1000 Hz bandwidth was compared with RF shimming and a standard 4-spoke MLS parallel excitation as in Chapter 4. The excitation profiles at a set of offset frequencies ranging from -500 to +500 Hz in steps of 100 Hz were simulated for all three designs. The uniformity of the excitations was quantified and compared using standard deviation (σ) of the pixels in the FOX. For a fair comparison, the same Tikhonov regularization parameter value (β) was used for all three designs, where it was empirically determined that the β value of 0.001 provides a good tradeoff between excitation error and RF power for all three designs.

For the RF shimming design, a multidimensional Powell optimization method (71) was used instead of the MLS optimization algorithm presented in Chapter 4. The MLS optimization algorithm naturally limits the resulting excitation phase to be smooth and slowly varying. However, apart from the uniform birdcage mode, the phase profile of all the other excitation modes of the coil exhibit rapid spatial phase variation (Figure 32b), and as a result the MLS optimization solution to RF shimming mainly employed the uniform birdcage mode, and contain very small contributions from the other modes. In trying to obtain the best-case performance of RF shimming that will be used to

compare with the other two design techniques, multidimensional Powell optimization method (71) was employed for the RF shimming design. The solution to this optimization method for RF shimming results in a more uniform magnitude excitation profile although it contains a much more rapidly varying phase.

For experimental validation, RF pulses for the spectral-spatial design were transmitted at a set of offset frequencies ranging from -500 to +500 Hz in steps of 100 Hz. The uniformity of the resulting excitation profiles was then compared to the ones obtained from simulation.

All the excitations were imaged with a standard 3D imaging sequence with the same imaging parameters as in Chapter 4. The excitation profiles were again inferred by dividing the reconstructed image by the estimated spin-density weighted birdcage receive profile. The RF excitation pulse amplitudes were adjusted so that all the experimental excitations were for the target flip angle of 5°.

6.4 Results

Figure 49 shows the in-plane excitation profiles at the center frequency (0 Hz) for RF shimming, a conventional water-only spoke design, and spectral-spatial spoke excitations. These three methods yielded B_1^+ deviations from the ideal uniform target (as measured by the standard deviation) of 14%, 2.84%, and 4.54 % respectively, while in contrast the standard birdcage mode resulted in a standard deviation of 23.5%. Even though RF shimming provided an improvement over the standard birdcage excitation, significant spatially-varying flip-angle inhomogeneity remained. Particularly noticeable is the low excitation region near the center of the FOX leading to a max/min excitation magnitude ratio of 36, compared to 3.29 in the standard birdcage, and 1.28 and 1.38 in the conventional and spectral-spatial spoke excitations. On the other hand, the conventional 4-spoke excitation mitigated essentially all of the B_1^+ inhomogeneity (for this on-resonance excitation), while the spectral-spatial version of the 4-spoke excitation

resulted in slightly less on-resonance uniformity than the narrow-band design, but significantly better mitigation than RF shimming alone.

Figure 50a) shows the standard deviation (σ) plots comparing the performance of the three excitation designs over a ±500 Hz frequency range. While RF shimming has the advantage of being essentially unaffected by off-resonant effects (dictated by the short duration (0.5ms) sinc-like pulse used), its σ value is high. The performance, as measured by the σ value, for the conventional 4-spoke excitation is excellent at the center frequency but deteriorates rapidly with off-resonance, for example, outside the ±200 Hz off-resonance range, the σ value obtained from this design becomes larger than one obtained from the RF Shimming design. On the other hand, the spectral-spatial pulse trades off a small amount of on-resonance homogeneity for a better uniformity over a much wider bandwidth. For this design, the σ value remains below 6% over the entire ±300 Hz design bandwidth.

Figure 50b) shows the standard deviation (σ) plots comparing simulation and experimental performances of the spectral-spatial spoke excitation over a ±500 Hz frequency range. In general, the experimental performance matches well with the predicted performance from simulation; with σ value from both cases following a similar trend across frequency, and with the experimentally determined σ at all frequencies being only slightly larger than one obtained from simulation.

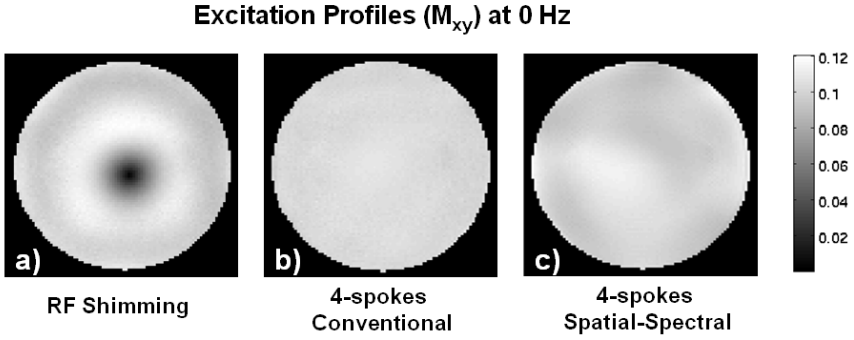

Figure 49: In-plane excitation profiles at center frequency for RF shimming, conventional spoke, and spectral-spatial spoke excitations respectively.

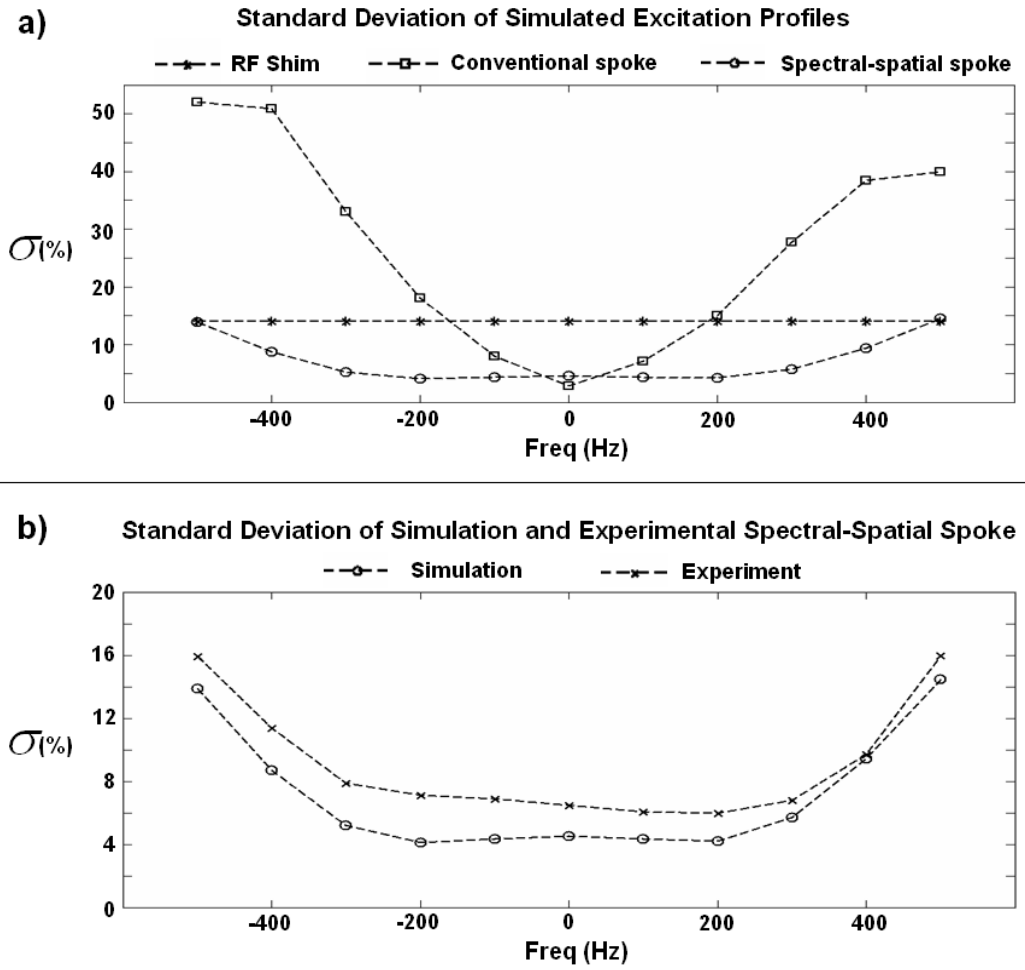

Figure 50: Standard deviation plots comparing **a)** the simulated performance of the three types of excitation designs, and **b)** the simulated and experimental performance of the spectral-spatial spoke excitation design over a ±500 Hz frequency range.

Figure 51, Figure 52, and Figure 53 summarize the excitation performance of the spectral-spatial pulse at 0, +300, and -300 Hz off-resonance frequencies. The figures show the through-slice and in-plane profiles at 3 different positions in *z*, along an image of the excited slab. In all cases, excellent slice selection and good in-plane uniformity were observed. In Figure 51 and Figure 53, a minor horizontal shift in the in-plane profiles (along the data readout direction) as a result of an off-resonance artifact during readout can be observed. As expected, this shift is symmetric with the profiles at +300 Hz shifted to the left and -300 Hz to the right.

Figure 54 shows the magnitude and phase profiles for the center slice of the excited slab at 0, ±200 Hz. The magnitude profile is uniform at all frequencies, while, as a result of MLS optimization, the phase profile varies both spatially and spectrally. The phase profile variation is smoothly varying and resulted in negligible intra-voxel dephasing.

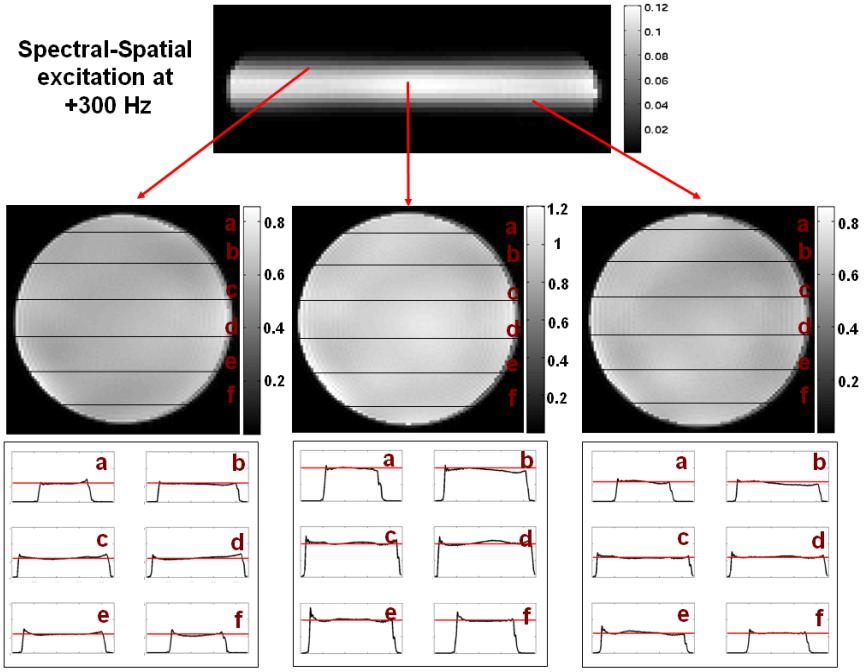

Figure 51: Excitation performance achieved by the spectral-spatial pulse at 300 Hz off-resonance with the through-slice profile (top), the in-plane profiles at 3 different though plane positions along the excited slab (center), and the corresponding 1-D profiles at several cuts through the in-plane profiles (bottom). Excellent slice selection and good in-plane profiles can be observed.

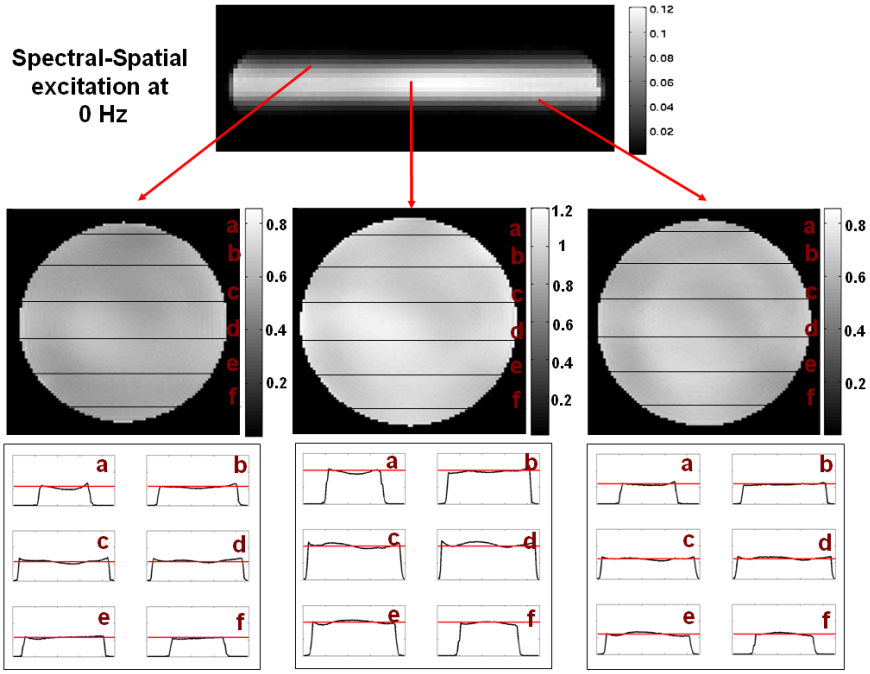

Figure 52: Summarizes the excitation performance achieved by the spectral-spatial pulse at 0 Hz off-resonance. Excellent slice selection and good in-plane profiles can be observed.

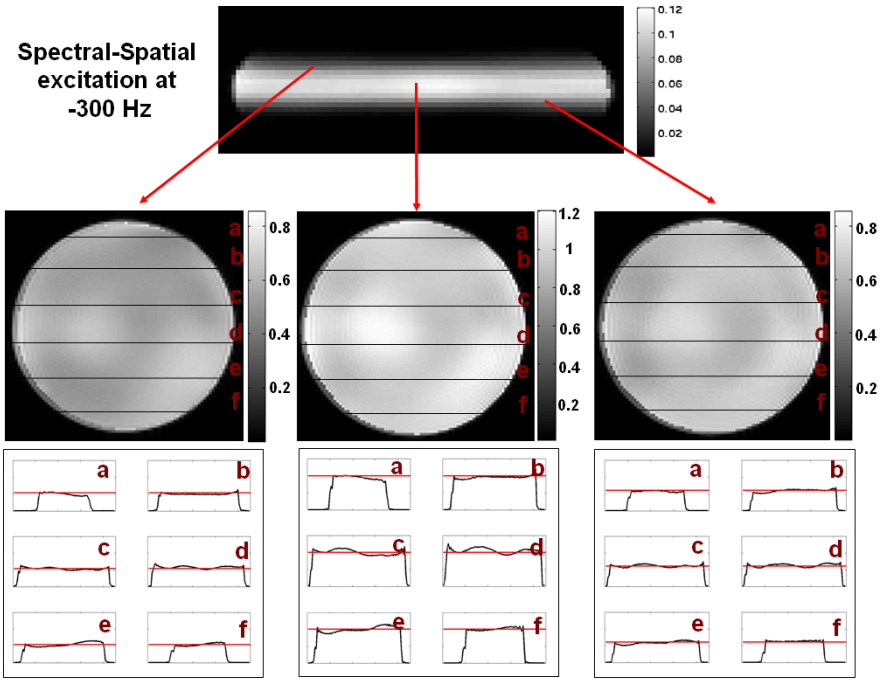

Figure 53: Summarizes the excitation performance achieved by the spectral-spatial pulse at -300 Hz off-resonance. Excellent slice selection and good in-plane profiles can be observed.

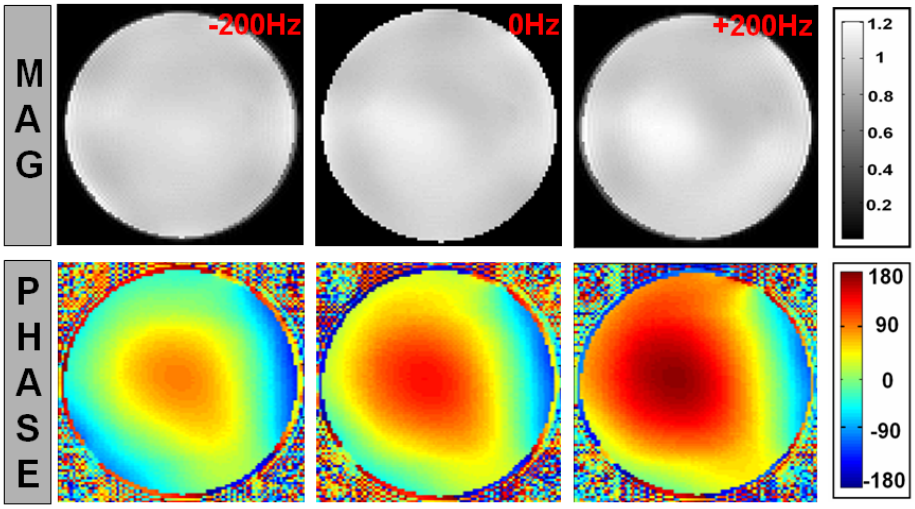

Figure 54: From left to right: the magnitude and phase profiles for the center slice of the excited slab at -200, 0, and +200 Hz respectively. The magnitude profile exhibits good uniformity at all three frequencies while, as expected from the MLS optimization, the phase profile varies smoothly both spatially and spectrally.

6.5 Discussion and Conclusions

In this work we generalized the spatial domain method for spectral-spatial parallel RF design and utilized this approach for the design of wideband uniform slab selection excitation pulses that mitigates large B_1^+ variation (peak-to-through ratio of > 3:1) over a 600 Hz bandwidth. A significant improvement in the spectral performance was achieved over the conventional parallel RF design, at the cost of only a minor reduction in excitation uniformity at the center frequency. Given this significant improvement in wideband excitation performance, we expect the design to play an important role in improving Chemical Shift Imaging at high field as well as other applications needing broad-band excitations, such as water-fat imaging.

In prior work described in Chapter 4, by using MLS optimization and allowing for spatial phase variation in the excitation profile, spoke-based slice-selective excitation performance was shown to improve significantly both in term of excitation uniformity and power requirements compared to parallel RF pulses designed with conventional LS. For the design of the spectral-spatial pulse, in addition to allowing for spatial phase variation, permitting spectral phase variation is crucial to achieve the desired magnitude performance target. In Figure 54, most of the spectral phase variation is from a bulk phase shift resulting from differences in spin frequency. Relaxing the target design phase both spectrally and spatially enables the incorporation of a natural spectral phase variation, avoiding designs that are ill-conditioned, and would result in very poor magnitude excitation.

With B_0 tracking, the 600 Hz excitation bandwidth achieved by the spectral-spatial spoke excitation would be sufficient in providing uniform excitation to many important metabolites in proton chemical shift imaging (CSI), with B_0 tracking to minimize adverse effects of spatially-varying main field inhomogeneity. In designing this excitation, no modification was made to the spoke gradient trajectory; therefore

excitation duration of the spectral-spatial pulse was the same as the one for conventional spoke excitation.

For other types of spectral-spatial excitation specifications where finer spectral control is required, e.g. narrow band or multi-band frequency selective excitation, longer gradient trajectory would be needed to capture higher frequency components required in such designs. One possible approach for this problem is to concatenate a set of several separate spoke excitations. This is analogous to the single-channel spectral-spatial excitation described in (72) which is based on the concatenation of sinc pulses. Future work includes design methods to determine optimal gradient trajectory for different types of parallel spectral-spatial excitations, and other types of excitations such as those based on spiral trajectories.

Chapter 7

High-Flip-Angle Parallel Excitation

7.1 Introduction

A major drawback of k-space based parallel transmission designs presented so far is their reliance on the small-tip-angle (STA) approximation, which causes them to perform poorly at large-flip-angles. Recently, several promising large-flip-angle design methods for parallel transmission have been proposed (70,73-77), with an experimental water phantom verification performed for a 2D spiral excitation using an 8 channel transmit system at 1.5T (70). Here, we describe a new large-flip-angle design method for spoke-based B_1^+ mitigated excitations. The method draws on our earlier large-flip-angle work in (16,76) and on the work by Xu et al in (70) to provide a much improved B_1^+ mitigation capability at large-flip-angle while utilizing relatively short duration RF waveforms. The method was demonstrated via large-flip-angle parallel excitation of 90° and 180° spin-echo slice-selective pulses on an 8 channel transmit array at 7T in the presence of B_1^+ inhomogeneity that matches the typical worst-case 3:1 range seen in human brain in vivo.

7.2 Theory

Parallel Transmission RF design overview

Our goal is to design slice-selective 90° and 180° spin-echo excitations which produce a spatially uniform within-slice flip angle distribution using a highly inhomogeneous multi-channel parallel transmission system designed for the head at 7T. We propose a two-stage design to achieve this goal: an initial (linear) approximation design, and a (nonlinear) Bloch-equation based iterative optimization design. In the initial approximation, the RF and gradient waveforms are designed based on the linear-class of large-tip-angle (LCLTA) method (69,70) with the incorporation of a magnitude least square optimization (MLS) criterion as presented in Chapter 4. This design method provides a fast algorithm to create large-flip-angle excitation that yields superior performance to the standard STA design. Nonetheless, the LCLTA design utilizes a linear approximation of the nonlinear Bloch equation, resulting in expected imperfections in the excitation profile when the pulses are driven to yield large flip angles. In the second part of the design, a Bloch-equation based iterative optimization (76) is used to achieve the ultimate performance by a refinement of the first-stage design. In this optimization, the solution from the initial approximation process is used as an initial guess for an iterative optimization process that loops through a numerical solution of the Bloch equation to provide improvement to the excitation profile. Substantial reduction in computation time during the 2nd design stage is achieved by the application of a local cost function evaluation combined with a spinor-domain based Bloch equation simulation (42).

Initial Approximation design

The initial approximation design step utilizes a LCLTA design for parallel transmission proposed Xu et al. (70), with an extension of MLS optimization. The LCLTA design

creates large-tip-angle parallel transmission pulses through concatenating a sequence of small-excitation pulses when certain k-space trajectories are used. Briefly, and following the notation in (70), the multi-dimensional excitation calculated for L coils using the LCLTA design is written as:

Equation 28

$$\theta(r) = \gamma \sum_{l=1}^{L} S_l^*(r) \int_0^T B_1^{(l)*}(t) e^{-ik(t)\cdot r} dt$$

where, S_l^* and $B_1^{(l)*}$ are the spatial transmit sensitivity profiles and the RF voltage waveforms for coils indexed by *l*, with * denoting complex conjugation, *r* is the spatial variable, $\theta(r)$ is the target flip angle about the x-axis after excitation, and *k(t)* is the excitation k-space trajectory, defined as $k(t) = -\gamma \int_t^T G(\tau) d\tau$, where γ is the gyromagnetic ratio, and G is the gradient, and T is the duration of the gradient waveform. After discretization in space and time, this expression can be written as a matrix equation, $\theta = Sb$, where the *S*-matrix incorporates (the conjugate of) the transmit sensitivity profiles modulated by the Fourier kernel due to the k-space traversal, θ is the target flip angle in space, and *b* contains (the conjugate of) the RF waveforms. With this formulation, the RF pulses can be designed by solving the following MLS optimization:

Equation 29

$$b = \arg_b \min\{ \| \, |Sb| - \theta \, \|_w^2 + \beta \|b\|_2^2 \}$$

Here, the optimization is performed over the region of interest (ROI) implied by a weighting, w, and $\beta \|b\|_2^2$ denotes the Tikhonov regularization term that is used to control the integrated RF power. The MLS optimization is represented by $|Sb|$ in Equation 29.

Inherently refocused spoke-based k-space trajectory similar to the ones described in (78) was used in this work to satisfy the "linear class" assumption for LCLTA design. In designing the spokes trajectory, we simplified the design by restricting the RF pulse shape of all coils to a Hanning-windowed sinc in k_z. Consequently we only needed to calculate the amplitude and phase modulation for each of the sinc spokes.

Bloch equation iterative optimization design

The aim of the iterative optimization is to improve on the excitation profile resulting from the initial linear approximation. The iterative optimization problem is stated as:

Equation 30

$$b = \arg_b \min\{\left\| \left|m_{actual}(b)\right| - m_{desired} \right\|_w^2 + \beta \|b\|_2^2\}$$
$$\text{s.t. } \|b\|_\infty < \text{ RF voltage limit}$$

where, m_{actual} is the actual transverse magnetization profile created by the RF pulses obtained via Bloch equation simulation, and $m_{desired}$ represents the desired transverse magnetization profile. Similar to the initial approximation design, an MLS condition is used to allow spatially-varying in-plane phase and improve the magnitude design. To simplify the calculation the optimization is again limited to the complex amplitude of the sinc spokes. Furthermore, in this design stage, as part of Equation 30, a hard limit on the maximum RF voltage is specified to accommodate hardware limits on maximum excitation amplitude.

Powell optimization (71) is chosen as the method for the iterative optimization of Equation 30. Similar to Conjugate-gradient methods, the Powell method is a direction-set method where line minimizations are performed successively along a set of directions (71). However, unlike the conjugate-gradient methods, the gradient or derivative of the cost function is not used in updating this set of directions during the optimization. Without the gradient information, more iterations may be required for the algorithm to converge. Nonetheless, in cases where gradient evaluation is expensive,

such as here, Powell optimization can be more efficient than conjugate-gradient search. In using Powell optimization to solve Equation 30, the initial bases at the start of the optimization are set to be either the real or imaginary part of the amplitude of the sinc spokes, and the line minimizations are performed along the bases in a bounded region that is within the maximum RF voltage constraint.

To speed up the design, the optimization is tailored to take advantage of the spin domain representation of the RF excitation (42). Cost function calculation via direct numerical evaluation of the Bloch equation in the spatial domain can be slow. As an alternative, spin domain formulation was used to provides a more compact rotational representation (2x2 matrices rather than 3x3), resulting in reduced computation. In addition, "partial" Bloch simulation method was introduced to further improve the computational efficiency. The spin domain formulation and the "partial" Bloch simulation are described below.

In (42), Pauly et al. provide a derivation for the spin domain Bloch simulation where the spin domain matrices, $Q_i(r)$, representing the rotation at different excitation time samples are multiplied together to obtain the total rotation, $Q(r)$, due to the applied RF and gradient waveforms. For n time points, the total rotation is represented as

Equation 31

$$Q(r) = Q_n(r)Q_{n-1}(r)\cdots Q_1(r).$$

The final magnetization is then calculated by applying the total rotation, $Q(r)$, to the initial magnetization vector. For parallel transmission, an additional step is required during simulation, whereby the contributions from the different RF transmission channels are added vectorially prior to the spin domain matrices calculation.

In deriving the "partial" Bloch simulation for Powell optimization, the spin domain representation is used to describe the spoke excitation. The total rotation in the

spoke excitation can be represented as the product of the spin domain matrices from the various spokes of the RF waveform.

Equation 32

$$Q(r) = (Q_n(r)Q_{n-1}(r)....)_{Spoke(N)} \times (Q_n(r)Q_{n-1}(r)....)_{Spoke(N-1)} ..... \times (Q_n(r)Q_{n-1}(r)....)_{Spoke(1)}$$

In Powell optimization, during a line minimization along a particular direction set, the complex amplitudes of only a limited subset of the spokes are allowed to change. Therefore, only the spin domain matrices associated with these spokes will be updated. This observation allows for an efficient calculation of the new total rotation during the line minimization, in which only the spin domain matrices of the modified spokes are recalculated. Once recalculated, these matrices are multiplied together with the matrices from the unchanged spokes to create the new total rotation. This "partial" Bloch simulation method substantially reduces the calculation time of the line minimization, especially in cases where a large number of spokes are present in the RF waveform.

Further reduction in computation time can be achieved via the appropriate selection of the spatial points to be included in the optimization. Since the time to perform the Bloch simulation scales linearly with the number of spatial points simulated, computation time for the optimization can be minimized by limiting the number of spatial points used in the cost function (Equation 30). Nonetheless, with highly inhomogeneous excitation coil profiles in a parallel transmission setup, a dense sample of simulated points are required to provide good control of the resulting in-plane and slice selection profile. Empirically, we found that in our eight transmission coil setup with a 17 cm FOV, using a grid of points spaced uniformly 0.8 cm apart in the transverse plane, in 3 equally spaced sections along z within the excited slice provides a good compromise between computation cost and acceptable convergence to the desired profile.

Variable-rate selective excitation (VERSE)

Variable-rate selective excitation (VERSE) (79) is a technique that has been widely used to effectively reduce SAR and limit peak RF voltage. VERSE takes previously designed RF and gradient waveforms and computes new set of waveforms that performs exactly the same selective excitation, but at significantly lower SAR and peak amplitude. At its most basic level, VERSE essentially slow down and stretch the excitation waveforms in region of high RF voltage. In (23), VERSE was used in a single channel spokes RF design. In (80,81), extensions of VERSE to multi-channel RF design were proposed for 2D spiral excitation. In this work, VERSE is employed for multi-channel spoke RF design to satisfy system peak RF voltage limitation of 130 V.

When VERSE is employed for parallel transmission it is important that the VERSEd RF waveforms from all the transmission coils are synchronous. To achieve this while avoiding unnecessary increase in pulse duration, each spoke of the RF waveform is VERSEd separately. For each spoke, the sinc pulse with the largest RF voltage is VERSEd to the system peak voltage limit. Subsequently, the other sinc pulses are then VERSEd such that their durations match with that of the first VERSEd sinc pulse.

B_0 inhomogeneity correction

B_0 inhomogeneity correction is incorporated into the RF design, both in the initial approximation design, and in the Bloch equation iterative optimization design. For the initial approximation design, a procedure similar to one presented in Chapter 2 is used. For the Bloch iterative optimization design, the B_0 inhomogeneity is accounted for by directly incorporating it into the Bloch equation simulation.

Additionally, when the VERSE algorithm is employed, an extra B_0 compensation step should be applied to the RF waveforms. In the presence of B_0 inhomogeneity, the effect of VERSE on the RF waveforms' off-resonance behavior can lead to significant excitation artifact. As an example, the excitation error of the 180° spin-echo RF waveforms used in this work increased by 184% after VERSEing (The excitation error

here is defined as the standard deviation value (σ) of the pixels in the field of excitation (FOX). The B_0 inhomogeneity present in this example has a smooth spatial variation and ranges from 20 to -80 Hz). To mitigate this VERSE-induced excitation artifact, the RF waveforms are re-optimized via the Bloch iterative optimization (post-VERSE). To ensure good convergence of this re-optimization, the RF waveforms should initially be VERSEd to a voltage level below that of the system limit (we used a margin of ~10% in this work). This will provide the re-optimization with a better working voltage range (up to the system voltage limit). With this re-optimization step, it was found that the excitation error can be reduced to the pre-VERSE level while still ensuring that the voltage limitations are satisfied.

7.3 Methods

System Hardware

Experiments were performed on the Siemens prototype 7T Magnetom scanner (Erlangen, Germany), using an 8-channel stripline coil array for transmit and receive as in Chapter 4. All measurements were performed in a 17-cm diameter water phantom.

RF Design

To demonstrate the capability of the proposed high-flip-angle design method, the technique was used to obtain parallel RF waveforms for 1-cm thick slice-selective 90° and 180° spin-echo excitation sequences that mitigate for B_1^+ inhomogeneity at 7T. In the spin-echo sequence, to create a sharp slice selection, 90° excitation with a 2-cm slice thickness, followed by a spin-echo pulse with a 1-cm slice thickness was used to ensure full excitation of the ±0.5 cm slice prior to the application of the 180° spin-echo excitation. Due to the design improvement from the MLS criteria, RF waveforms containing only 3 spokes were adequate for both the 90° and 180° excitations to achieve slice selection with excellent B_1^+ mitigation. Sinc sub-pulses with time-bandwidth-

product of 4 were used, and the gradient trajectories were designed for maximum gradient amplitude and slew rate limits of 15 mT/m and 150 T/m/s, resulting in pre-VERSE pulse durations of 3.31 and 2.06 ms for 1-cm and 2-cm thick excitations respectively. The post-VERSE pulse durations for the 1-cm thick 90° and 180° excitations were 4.4 and 5.6 ms while the duration for the 2-cm thick 90º excitation was 3.26 ms. The maximum voltage level used for VERSEing was 120 V, whereas the system voltage limit used for the RF waveforms re-optimization was 130 V.

For each RF pulse design, the appropriate Tikhonov regularization parameter value (β) that provides a good tradeoff between excitation error and RF power was empirically determined via the L-curve plot (82).

Experiments and Quantification

For high-flip-angle excitations both the spatial uniformity and the flip angle of the excitation pulses were quantified. The uniformity of the excitation profiles was quantified by the fraction of pixels in the FOX that are within ±10% and ±20% ranges around the mean in-slice signal value, as well as by the normalized standard deviation, σ, of the pixels in the FOX. In quantifying the flip-angle, different methods were used for the 90° and the 180° spin-echo excitations.

For the 90° excitation, the RF waveforms were transmitted at a series of RF voltage levels, and the average in-plane excitation intensity at each level was recorded and compared against ones predicted by simulation. The simulated intensities used for the comparison were obtained by first performing the Bloch simulation on the RF waveforms at a series of voltages to acquire the flip-angle distribution, $\theta(x, y, V)$. This distribution is then use to calculate the image intensity (inside the FOX) via the following equation (from Equation 15 in Chapter 3),

Equation 33

$$I(x,y,V) \propto \frac{[1-e^{-TR/T_1(x,y)}]\sin\theta(x,y,V)}{1-e^{-TR/T_1(x,y)}\cos\theta(x,y,V)}$$

The image intensity inside the FOX is then averaged to create the average excitation intensities used for the comparison.

To validate the 180° pulse in the spin-echo sequence, we measured the performance of the phase reversal effect of the pulse. For this task, data acquired with two spin-echo sequences were compared where the 90° excitation pulses differed in phase by 90°. The phase shift caused the excited transverse magnetization to be shift in phase by the same amount (i.e. 90°). With the proper application of the 180° pulse, this phase shift should reverse from 90° to -90°. Therefore, by comparing the excitation phase images produced by the two sequences, the efficiency of the phase reversal and echo effect of the 180° pulse can be determined. (The relative phase different between the two images should be -90°)

7.4 Results

90° Excitation

Figure 55 shows the excitation profiles from the 90° excitation, with the in-plane and the slice selection profiles on the left and the 1-D through-slice profiles (A-F) on the right. Excellent in-plane B_1^+ mitigation and slice selection can be observed. To quantify the performance of the excitation, we note that 96% of the in-slice pixels deviate by less than 10% from the flat magnitude target profile, whereas all in-slice pixels are contained within the 20% bracket. The normalized standard deviation of the in-slice pixels for this excitation is 5.1%.

Figure 56 shows the normalized average in-plane intensity as a function of peak RF excitation voltage for both simulation and experimental data. Good agreement between the two data sets can be observed, validating the expected flip-angle behavior of the 90° excitation pulse.

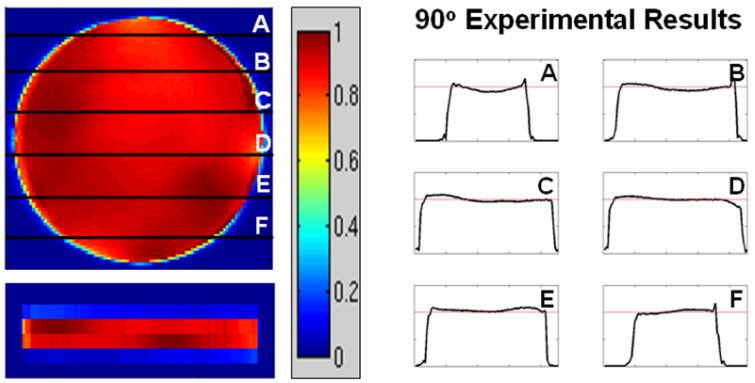

Figure 55: Excitation profiles from the 3-spoke 90° excitation, **Left:** the in-plane and the slice selection profiles, **Right:** the 1-D through-plane profiles along several cuts through the in-plane profile.

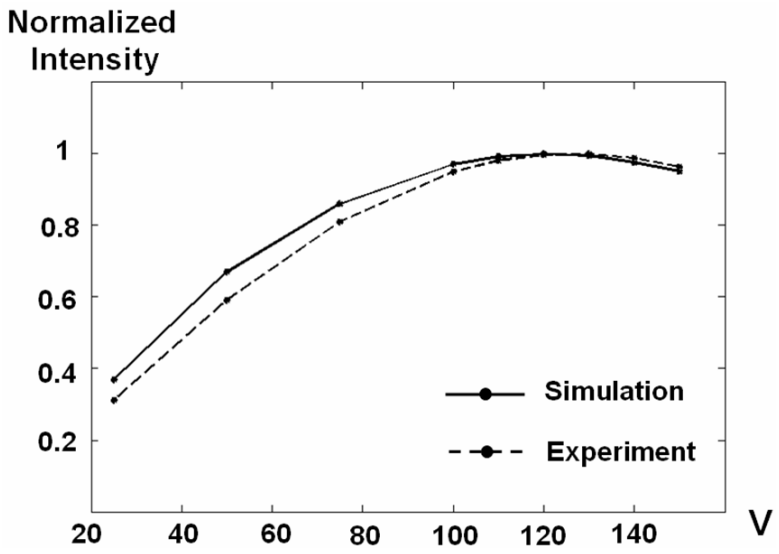

Figure 56: Simulation and experimental data plots of the normalized average in-plane intensity as a function of peak RF voltage for the 3-spokes 90° excitation. Good agreement between the simulation and experimental data can be observed.

Spin-Echo Excitation

Figure 57 shows the sequence diagram for the VERSEd spin echo sequence which consist of a 3-spoke 90° and a 3-spoke 180° spin-echo excitations (TE = 20 ms). Shown are the G_z gradient and RF waveform from one of the transmission coils (coil 1). Note, the effect of VERSE in stretching the center region of each RF sinc pulses to reduce the max RF voltage. Also shown are the crusher gradients surrounding the spin-echo RF, which are used to suppress parasitic excitation in the slice profile transition regions. Figure 58 shows the excitation profiles for this spin-echo sequence. Again, excellent in-plane B_1^+ mitigation and slice selection can be observed. To quantify the performance of this excitation, 92% of the in-slice pixels deviate by less than 10% from the flat target profile, whereas all pixels are contained within the 20% bracket. The standard deviation of the in-plane pixels for this excitation is 6.2%

Figure 59 provides a validation of the phase reversal effect of the 180° spin-echo excitation. The phase image obtained from the standard and the modified spin-echo sequences are shown on the top left and right respectively. The relative phase difference image is shown at the bottom of the figure. As expected, a relative phase difference of -90° can be observed throughout the image.

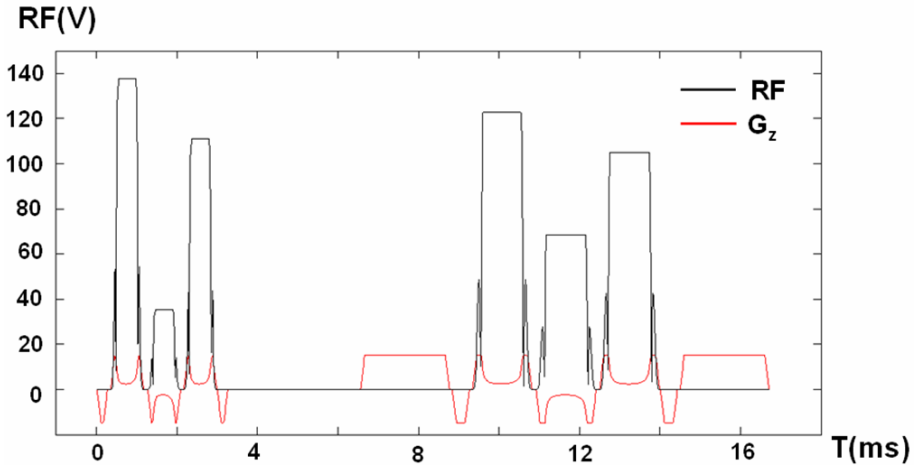

Figure 57: Z-gradient (G_z) and RF waveforms from one of the excitation coil (coil 1) for the VERSEd spin-echo sequence consisting of a 3-spoke 90° and180° spin-echo excitations (TE = 20 ms). Also shown are the G_z crusher gradients surrounding the spin-echo RF.

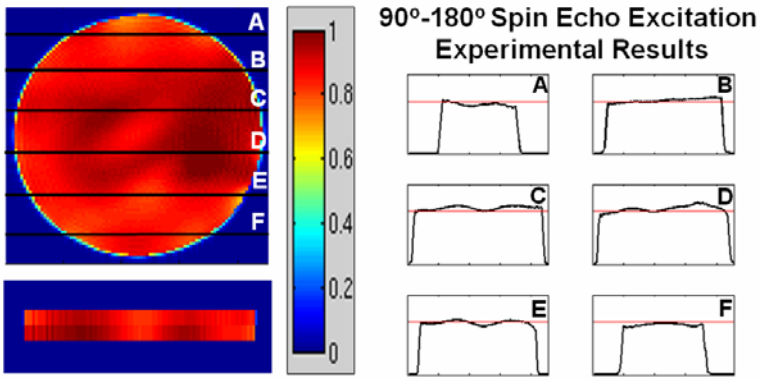

Figure 58: Spin-echo excitation profiles, **Left:** the in-plane and the slice selection profiles, **Right:** the 1-D though-plane profiles along several cuts through the in-plane profile.

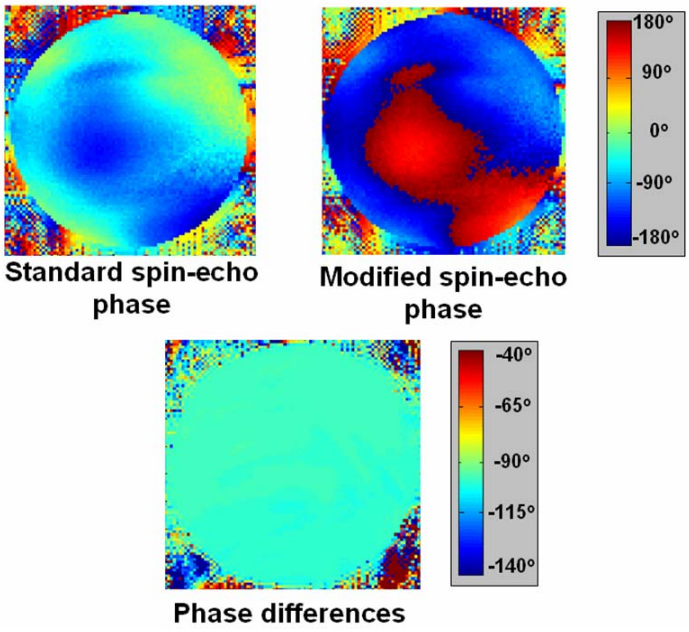

Figure 59: **Top:** the phase images obtained from the standard (left) and the modified (right) spin-echo sequences. **Bottom:** the relative phase difference image, with observed phase difference of -90° as predicted.

7.5 Discussion and Conclusions

In this work, we outlined a design method for slice-selective large-flip-angle parallel RF excitation. The method was used to design both 90° and spin-echo slice-selective excitations that mitigate severe B_1^+ inhomogeneity at a similar level to that observed in human in-vivo imaging at 7T. The RF excitations were experimentally tested via an eight channel parallel transmission system, with experimental results providing validation for both the B_1^+ inhomogeneity mitigation performance as well as the flip-angle accuracy of the excitations. Slice-selective excitations with parallel RF systems offer means to implement conventional high-flip excitation sequences without severe pulse-duration penalty, even at very high B_0 field strengths where large B_1^+ inhomogeneity is present.

Based on the performance of the Linux Intel® Xeon 3 GHz server used for the design of the RF pulses, in Matlab, the initial approximation design calculation time was in the range of 5-8 seconds and the Bloch iterative optimization calculation time was in the range of 100-150 seconds, resulting in an overall design time of around 4-5 minutes for each RF excitation (note: the Bloch iterative optimization has to be performed twice, pre and post VERSE).

It was observed that the Bloch iterative optimization was crucial for the 180° excitation design, but does not provide much benefit for the 90° excitation design. For the 90º excitation, the initial approximation design provides excellent excitation that performed well even after the application of VERSE. This is likely due to the fact that the 90° excitation requires a lower flip-angle and consequently the linear class assumption in the LCLTA design is better preserved. Furthermore, the 90° excitation requires relatively low peak RF voltage, and hence the increase in pulse duration due to VERSE is relatively small. With this observation, the 90° excitation can be rapidly created using only the initial approximation design.

Chapter 8

Summary and Recommendations

8.1 Summary

Higher magnetic field strength scanners offer the potential for improvement in image SNR and contrast in MRI. However, the presence of dramatic spatial variation in B_1^+ transmit field of the RF coils in these scanners causes very unfavorable spatial non-uniformity in the excitation across the region of interest, and greatly limits the application of many conventional imaging techniques. This thesis was motivated by the critical and pressing need to solve this issue, which is essential in bringing high-field MRI to clinical use. Parallel transmission, an emerging technique, was used to create RF excitation that mitigated dramatic B_1^+ inhomogeneity while satisfying the constraint of sufficiently short RF pulses for practical clinical applications. Novel algorithms were proposed that resulted in robust and rapid mapping of the excitation field, excellent excitation control, low RF power requirements, extension to non-linear large-flip-angle excitation, as well as a new algorithm for simultaneous spectral and spatial excitation. For testing and validation, these methods were implemented on a newly developed parallel transmission platform on both 3T and 7T MRI scanners with 8-channel transmission to demonstrate the ability of these methods for high-fidelity B_1^+ mitigation. Further, spatially-tailored RF pulses were demonstrated beyond conventional slice- or slab- selective excitation.

The main contributions of this work are summarized below:

- Initial validation, with design and implementation of parallel transmission on a prototype 8-channel RF system at 3T for both phantom and human subject studies, successfully demonstrating the capability of the technique in creating short RF excitation pulses for mitigating B_1^+ inhomogeneity, and for providing excitation of arbitrarily shaped volumes.
- Development of a Rapid Quantitative B_1 mapping technique which is essential for the implementation of Parallel Transmission at high-field.
- The invention, implementation, and phantom validation of Magnitude-least-squares (MLS) optimization technique for parallel RF transmission design; resulting in substantially improvement in excitation magnitude profile and reduction in required RF power when compared to conventional Least-square design technique.
- Implementation and demonstration of in vivo parallel transmission at 7T using MLS and k-space trajectory optimizations to create short excitation waveforms which mitigate severe B_1^+ inhomogeneity. In addition, accelerated spatially tailored RF pulses which excite a high resolution square target pattern were also presented.
- The invention of spectral-spatial excitation algorithm for parallel transmission, along with the application of the algorithm for design, implementation, and phantom demonstration of wideband uniform slab-selective excitation that mitigates large B_1^+ variation over a 600 Hz bandwidth at 7T.
- Design algorithm, implementation for efficient computation, and phantom demonstration at 7T of parallel transmit RF waveforms for large-tip-angle slice-selective excitation with B_1^+ mitigation.

The novel methods presented here will be essential to robust clinical applications in future high-field human imaging.

8.2 Recommendations

The list below provides several logical extensions to the work presented in this thesis.

- Application of B_1^+ mitigated RF pulses for imaging techniques that has so far been impractical or suboptimal at 7T due to B_1^+ inhomogeneity. With B_1^+ mitigated excitation, the benefit of high-field system for these techniques can be fully realized. Some candidate applications are Diffusion Tensor Imaging (83)[1] (DTI), and Chemical Shift Imaging (via wideband spectral-spatial excitation).
- Application of accelerated high resolution specific volume excitation in functional MRI (84)[2] (fMRI) to improve spatial and temporal resolution. Ideally, for best result, the spatially tailored excitation that excites a specific volume of interest should be applied in conjunction with an efficient reduced FOV parallel readout technique.
- Investigation of possible design methods for parallel spectral-spatial excitations that require finer spectral excitation control such as in narrow band or multi-band frequency selective excitation useful in fat and/or water suppression. To achieve finer spectral control, long RF and gradient waveforms are needed. One possible approach is to concatenate a set of several separate excitation waveforms. This is analogous to the single-channel spectral-spatial excitation described in (72), which is based on the concatenation of sinc excitation pulses. Future work includes the exploration of design methods that could determine optimal gradient trajectory for different types of parallel spectral-spatial excitations.

[1] DTI is a non-invasive in vivo method for determining the directionality and magnitude of water diffusion. It has many applications such as in estimation of damage to nerve fibers that connect the area of the brain affected by the stroke to brain regions that are distant from it, and can be used to determine the effectiveness of stroke prevention medications. It also enables the visualization of white matter fibers in the brain and can map subtle changes in the white matter associated with diseases such as multiple sclerosis and epilepsy.

[2] fMRI is a non-invasive in vivo method for characterizing neuronal function, which enable us to see areas of the brain that work together during a particular perception, cognition, memory, or action.

- Development of a more realistic SAR monitoring technique for in vivo parallel RF transmission. The in vivo experiments in this work employ a very conservative SAR monitoring system. The worst case scenario SAR estimates along with a safety factor of two in the allowed SAR level were used. This restricted the usage of high SAR excitation sequences. Comprehensive SAR simulation for parallel transmission is required in order to allow a more aggressive SAR monitoring, which will be the key to applying parallel transmission to demanding clinical applications.
- Investigation of SAR reduction algorithms in Parallel transmission. In this thesis, Tikhonov regularization and VERSE algorithm are used to control excitation RF power. SAR is related to RF power, but does not exhibit a direct relationship i.e. lower RF power excitation does not always guarantee lower SAR. Recently, algorithms incorporating SAR as a direct constraint or trade-off parameter in RF pulse design have been proposed (85,86). Future work includes adapting such algorithms into our pulse design methods.

Bibliography

1. Chang AE, Matory YL, Dwyer AJ, Hill SC, Girton ME, Steinberg SM, Knop RH, Frank JA, Hyams D, Doppman JL, et al. Magnetic resonance imaging versus computed tomography in the evaluation of soft tissue tumors of the extremities. Ann Surg 1987;205(4):340-348.
2. Sundgren PC, Philipp M, Maly PV. Spinal trauma. Neuroimaging Clin N Am 2007;17(1):73-85.
3. Scheidler J, Reiser MF. MRI of the female and male pelvis: current and future applications of contrast enhancement. Eur J Radiol 2000;34(3):220-228.
4. Young GS. Advanced MRI of adult brain tumors. Neurol Clin 2007;25(4):947-973, viii.
5. Bomsdorf H, Helzel T, Kunz D, Roschmann P, Tschendel O, Wieland J. Spectroscopy and imaging with a 4 tesla whole-body MR system. NMR Biomed 1988;1(3):151-158.
6. Vaughan JT, Garwood M, Collins CM, Liu W, DelaBarre L, Adriany G, Andersen P, Merkle H, Goebel R, Smith MB, Ugurbil K. 7T vs. 4T: RF power, homogeneity, and signal-to-noise comparison in head images. Magn Reson Med 2001;46(1):24-30.
7. Collins CM, Liu W, Schreiber W, Yang QX, Smith MB. Central brightening due to constructive interference with, without, and despite dielectric resonance. J Magn Reson Imaging 2005;21(2):192-196.
8. Katscher U, Bornert P, Leussler C, van den Brink JS. Transmit SENSE. Magn Reson Med 2003;49(1):144-150.
9. Zhu Y. Parallel excitation with an array of transmit coils. Magn Reson Med 2004;51(4):775-784.
10. Griswold M, Kannengiesser S, Muller M, Jakob P. Autocalibrated accelerated parallel excitation (transmit-GRAPPA). In: Proceedings of the 13th Annual Meeting of ISMRM. 2005; Miami Beach, FL, USA. p 2435.
11. Grissom W, Yip CY, Zhang Z, Stenger VA, Fessler JA, Noll DC. Spatial domain method for the design of RF pulses in multicoil parallel excitation. Magn Reson Med 2006;56(3):620-629.
12. Ullmann P, Junge S, Wick M, Seifert F, Ruhm W, Hennig J. Experimental analysis of parallel excitation using dedicated coil setups and simultaneous RF transmission on multiple channels. Magn Reson Med 2005;54(4):994-1001.
13. Setsompop K, Wald LL, Alagappan V, Gagoski B, Hebrank F, Fontius U, Schmitt F, Adalsteinsson E. Parallel RF transmission with eight channels at 3 Tesla. Magn Reson Med 2006;56(5):1163-1171.

14. Setsompop K, Wald LL, Gagoski B, Alagappan V, Hebrank F, Fontius U, Schmitt F, Adalsteinsson E. Parallel RF Excitation Design and Testing with an 8 Channel Array at 3T; . In: Proceedings of the 14th Annual Meeting of ISMRM, Seattle, Washington , USA, 2006, p 576.
15. Setsompop K, Zelinski AC, Alagappan V, Nistler J, Hebrank F, Fontius U, Schmitt F, Wald LL, Adalsteinsson E. In vivo Parallel RF Excitation with B0 correction. In: Proceedings of the 15th Annual Meeting of ISMRM, Berlin, Germany, 2007, p 671.
16. Setsompop K, Wald LL, Alagappan V, Gagoski BA, Adalsteinsson E. Magnitude Least Squares Optimization for Parallel RF Excitation Design Demonstrated at 7 Tesla with 8 Channels. Magn Reson Med 2008;59(4):908-915.
17. Abragam A. Principles of Nuclear Magnetism: Oxford Science Publications.
18. Nishimura DG. Principles of Magnetic Resonance Imaging, Standford University: Self Published; 1996.
19. Haacke EM, Brown RW, Thompson MR, Venkatesan R. Magnetic Resonance Imaging: Physical Principles and Sequence Design: Wiley-Liss; 1999.
20. Bloch F. Nuclear Induction. Phys Rev 1946;70:460-474.
21. Pauly J, Nishimura D, Macovski A. A k-space analysis of small-tip angle excitation. J Magn Reson 1989;81:43-56.
22. Setsompop K, Wald LL, Gagoski B, Alagappan V, Hebrank F, Fontius U, Schmitt F, Adalsteinsson E. 2D and 3D Parallel RF Pulse Design for Inhomogeneity Correction and Volume Localization. In: Proceedings of the 14th Annual Meeting of ISMRM, Seattle, Washington , USA, 2006, p 575.
23. Saekho S, Yip CY, Noll DC, Boada FE, Stenger VA. Fast-kz three-dimensional tailored radiofrequency pulse for reduced B1 inhomogeneity. Magn Reson Med 2006;55(4):719-724.
24. Ulloa JL, Irarrazaval P, Hajnal JV. Exploring 3D RF shimming for slice selective imaging. In: Proceedings of the 13th Annual Meeting of ISMRM, Miami Beach, Florida, USA, 2005 p 21.
25. Sung K, Cunningham CH, Nayak KS. Validation of B1+ Non-uniformity Correction in the Chest at 3T using TIP-COMP. In: Proceedings of the 14th Annual Meeting of ISMRM, Seattle, Washington, USA, 2006 p 597.
26. Stenger VA, Saekho S, Zhang Z, Yu S, Boada FE. B1 Inhomogeneity Reduction with Transmit SENSE. 2004; Zurich, Switzerland. p 94.
27. Saekho S, Boada FE, Noll DC, Stenger VA. Small tip angle three-dimensional tailored radiofrequency slab-select pulse for reduced B1 inhomogeneity at 3 T. Magn Reson Med 2005;53(2):479-484.
28. Ulloa J, P. I, Hajnal JV. Exploring 3D RF shimming for slice selective imaging. 2005; Miami Beach, Florida, USA. p 21.
29. Griswold MA, Jakob PM, Heidemann RM, Nittka M, Jellus V, Wang J, Kiefer B, Haase A. Generalized autocalibrating partially parallel acquisitions (GRAPPA). Magn Reson Med 2002;47(6):1202-1210.
30. Alagappan V, Adalsteinsson E, Setsompop K, Fontius U, Zelinski AC, Wiggins GC, Hebrank F, Schmitt F, Wald LL. Comparison of Three Transmit Arrays for Parallel Transmit. In: Proceedings of the 15th Annual Meeting of ISMRM, Berlin, Germany,2007, p 35.

31. Alagappan V, Nistler J, Adalsteinsson E, Setsompop K, Fontius U, Zelinski A, Vester M, Wiggins GC, Hebrank F, Renz W, Schmitt F, Wald LL. A Degenerate Mode Band-Pass Birdcage for Accelerated Parallel Excitation. Magn Reson Med 2007;57(6):1148-1158. .
32. Sodickson DK, Manning WJ. Simultaneous acquisition of spatial harmonics (SMASH): fast imaging with radiofrequency coil arrays. Magn Reson Med 1997;38(4):591-603.
33. Pruessmann KP, Weiger M, Scheidegger MB, Boesiger P. SENSE: sensitivity encoding for fast MRI. Magn Reson Med 1999;42(5):952-962.
34. Schmitt M, Potthast A, Sosnovik DE, Wiggins GC, Triantafyllou C, Wald LL. A 128 Channel Receive-Only Cardiac Coil for 3T. In: Proceedings of the 15th Annual Meeting of ISMRM, Berlin, Germany, 2007, p 245.
35. Hardy CJ, Giaquinto RO, Piel JE, Rohling KW, Marinelli L, Fiveland EW, Rossi CJ, Park KJ, Darrow RD, Watkins RD, Foo TK. 128-Channel Body MRI with a Flexible High-Density Receiver-Coil Array. In: Proceedings of the 15th Annual Meeting of ISMRM, Berlin, Germany, 2007, p 244.
36. Hahn EL. Spin Echos. Phys Rev 1950;80:580.
37. Zhu Y. Acceleration of focused excitation with a transmit coil array. 2002; Honolulu, Hawaii, USA. p 190.
38. Katscher U, Bornert P, Leussler C, van den Brink JS. Theory and experimental verification of Transmit SENSE. 2002; Hawaii. p 189.
39. Zhu Y, Watkins R, Giaquinto R, Hardy C, Kenwook G, Mathias S, Valent T, Denzin M, Hopkins J, Peterson W, Mock B. Parallel excitation on an eight transmit channel MRI system. 2005; Miami. p 14.
40. Grissom W, Yip C-Y, Noll DC. A new method for the design of RF pulses in Transmit SENSE. 2004; Zurich, Switzerland. p 95.
41. Saekho S, Yip C-Y, Noll DC, Boada FE, Stenger VA. A Fast-kz 3D Tailored RF Pulse for Reduced B1 Inhomogeneity. 2005; Miami Beach, Florida, USA. p 22.
42. Pauly J, Le Roux P, Nishimura D, Macovski A. Parameter relations for the Shinnar-Le Roux selective excitation pulse design algorithm. IEEE Transactions on Medical Imaging 1991;10(1):53-65.
43. Ibrahim TS, Lee R, Baertlein BA, Abduljalil AM, Zhu H, Robitaille PM. Effect of RF coil excitation on field inhomogeneity at ultra high fields: a field optimized TEM resonator. Magn Reson Imaging 2001;19(10):1339-1347.
44. Mao W, Smith MB, Collins CM. Exploring the limits of RF shimming for high-field MRI of the human head. Magn Reson Med 2006;56(4):918-922.
45. Vaughan T, DelaBarre L, Snyder C, Tian J, Akgun C, Shrivastava D, Liu W, Olson C, Adriany G, Strupp J, Andersen P, Gopinath A, van de Moortele PF, Garwood M, Ugurbil K. 9.4T human MRI: preliminary results. Magn Reson Med 2006;56(6):1274-1282.
46. Nistler J, Fontius U, Wald LL, Adalsteinsson E, Setsompop K, Alagappan V, Hebrank F, Schmitt F, Renz W. In: Proceedings of the 15th Annual Meeting of ISMRM, Berlin, Germany,2007, p. 35.
47. Hornak JP, Szumowski J. Magnetic field mapping. Magn Reson Med 1988;6:158–163.

48. Akoka S, Frankoni F, Seguin F, Pape AL. Radiofrequency map of an NMR coil by imaging. Magn Reson Imaging 1993;11:437–441.
49. Topp S, Adalsteinsson E, Spielman DM. Fast Multislice B1-Mapping. In: Proceedings of the 5th Annual Meeting of ISMRM, Vancouver BC, Canada, 1997 p 281.
50. Stollberger R, Wach P, McKinnon G, Justich E, Ebner F. Rf-field mapping in vivo. In: Proceedings of the 7th Annual Meeting of SMRM, SanFrancisco, CA, USA, 1988 p 106.
51. Maier JK, Glover GH; Method for mapping the rf transmit and receive field in an NMR system. U. S. Patent 5001428, 1991.
52. Insko EK, Bolinger L. B1 mapping. In: Proceedings of the 11th Annual Meeting of SMRM, Berlin, Germany, 1992 p 4302.
53. Insko EK, Bolinger L. Mapping of the radiofrequency field. J Magn Reson A 1993;103:82–85.
54. Stollberger R, Wach P. Imaging of the active B1 field in vivo. Magn Reson Med 1996;35:246–251.
55. Yarnykh VL, Yuan C. Actual flip angle imaging in the pulsed steady state. In: Proceedings of the 12th Annual Meeting of ISMRM, Kyoto, Japan, 2004 p 194.
56. Cunningham CH, Pauly JM, Krishna NS. Saturated Double-Angle Method for Rapid B1+ Mapping. Magn Reson Med 2006;55:1326-1333.
57. Levitt MH. Composite pulses. Progr NMR Spectrosc 1986(18):61–122.
58. Staewen RS, Johnson AJ, Ross BD, Parrish T, Merkle H, Garwood M. 3-D FLASH imaging using a single surface coil and a new adiabatic pulse, BIR-4. Invest Radiol 1990;25:559–567.
59. Kerr AB, Cunningham CH, Pauly JM, Giaquinto RO, Watkins RD, Zhu Y. Self-Calibrated Transmit SENSE. In: Proceedings of the 14th Annual Meeting of ISMRM, Seattle, Washington, USA, 2006 p 2561
60. Kerr AB, Cunningham CH, Pauly JM, Piel JE, Giaquinto RO, Watkins RD, Zhu Y. Accelerated B1 Mapping for Parallel Excitation. In: Proceedings of the 15th Annual Meeting of ISMRM, Berlin, Germany, 2007, p 80.
61. Le Roux P, Gilles RJ, McKinnon GC, Carlier PG. Optimized outer volume suppression for single-shot fast spin-echo cardiac imaging. J Magn Reson Imaging 1998;8(5):1022-1032.
62. Schricker AA, Pauly JM, Kurhanewicz J, Swanson MG, Vigneron DB. Dualband spectral-spatial RF pulses for prostate MR spectroscopic imaging. Magn Reson Med 2001;46(6):1079-1087.
63. Collins CM, Liu W, Swift BJ, Smith MB. Combination of optimized transmit arrays and some receive array reconstruction methods can yield homogeneous images at very high frequencies. Magn Reson Med 2005;54(6):1327-1332.
64. Park JY, DelaBarre L, Garwood M. Improved gradient-echo 3D magnetic resonance imaging using pseudo-echoes created by frequency-swept pulses. Magn Reson Med 2006;55(4):848-857.
65. Kassakian PW. Convex Approximation and Optimization with Applications in Magnitude Filter Design and Radiation Pattern Synthesis: University of California at Berkeley; 2006.

66. Katscher U, Vernickel P, Graesslin I, Boernert P. RF shimming using a mult-element transmit system in phantom and in vivo studies. In: Proceedings of the 15th Annual Meeting of ISMRM, Berlin, Germany, 2007, p 1693.
67. Kerr AB, Zhu Y, Pauly JM. Phase Constraint Relaxation in Parallel Excitation Pulse Design. In: Proceedings of the 15th Annual Meeting of ISMRM, Berlin, Germany, 2007, p 1694.
68. Collins CM, Wang Z, Smith MB. A Conservative Method for Ensuring Safety within Transmit Arrays. 2007; Berlin, Germany. p 15.
69. Pauly J, Nishimura D, Macovski A. A linear class of large-tip-angle selective excitation pulses. J Magn Reson 1989;82:571–587.
70. Xu D, King KF, Zhu Y, McKinnon GC, Liang ZP. A noniterative method to design large-tip-angle multidimensional spatially-selective radio frequency pulses for parallel transmission. Magn Reson Med 2007;58(2):326-334.
71. Press WH. Numerical recipe in C. 2nd ed. Cambridge: Cambridge University Press; 1992.
72. Meyer CH, Pauly JM, Macovski A, Nishimura DG. Simultaneous spatial and spectral selective excitation. Magn Reson Med 1990;15(2):287-304.
73. Ulloa JL, Callaghan M, Guarini M, Hajnal JV, Irarrazaval P. Calculation of B1 pulse for RF shimming at arbitrary flip angle using multiple transmitters. In: Proceedings of the 14th Annual Meeting of ISMRM, Seattle, Washington, USA, 2006 p 3016.
74. Grissom WA, Fessler JA, Noll DC. Time-Segmented Spin Domain Method for Fast Large-Tip-Angle RF pulse Design in Parallel Excitation. In: Proceedings of the 15th Annual Meeting of ISMRM, Berlin, Germany, 2007, p 676.
75. Grissom WA, Fessler JA, Noll DC. Additive-Angle Method for Fast Large-Tip-Angle RF Pulse Design in Parallel Excitation. In: Proceedings of the 15th Annual Meeting of ISMRM, Berlin, Germany, 2007, p 1689.
76. Setsompop K, Zelinski AC, Alagappan V, Hebrank F, Fontius U, Schmitt F, Wald LL, Adalsteinsson E. High flip angle slice selective Parallel RF Excitation on an 8-channel system at 3T. In: Proceedings of the 15th Annual Meeting of ISMRM, Berlin, Germany, 2007, p 677.
77. Xu D, King KF, Zhu Y, McKinnon G, Liang Z. Multidimensioinal Arbitrary-Flip-Angle Parallel Transmit Pulse Design Using an Optimal Control Approach. In: Proceedings of the 15th Annual Meeting of ISMRM, Berlin, Germany, 2007, p 1696.
78. Xu D, King KF, Zhu Y, McKinnon G, Liang Z. Reducing B1 Inhomogeneity Using Optimized Parallel Transmit Pulses. In: Proceedings of the 15th Annual Meeting of ISMRM, Berlin, Germany, 2007, p 1700.
79. Conolly SM, Nishimura DG, Macovski A, Glover GH. Variable-rate selective excitation. J Magn Reson 1988;78:440-458.
80. Wu X, Akgun C, Vaughan JT, Ugurbil K, van de Moortele PF. SAR Reduction in Transmit SENSE Using Adapted Excitation k-space Trajectories. In: Proceedings of the 15th Annual Meeting of ISMRM, Berlin, Germany, 2007, p 673.
81. Graesslin I, Biederer S, Schweser F, Zimmermann K-H, Katscher U, Börnert P. SAR Reduction for Parallel Transmission using VERSE and k-space Filtering. In:

Proceedings of the 15th Annual Meeting of ISMRM, Berlin, Germany, 2007, p 674.
82. Lin FH, Kwong KK, Belliveau JW, Wald LL. Parallel imaging reconstruction using automatic regularization. Magn Reson Med 2004;51(3):559-567.
83. Mori S. Introduction to Diffusion Tensor Imaging Elsevier Science; 2007.
84. Huettel SA, Song AW, McCarthy G. Functional Magnetic Resonance Imaging: Sinauer Associates; 2004.
85. Zelinski A, Goyal VK, Angelone LA, Bonmassar G, Wald LL, Adalsteinsson E. Designing RF pulses with optimal specific absorption rate (SAR) characteristics and exploring excitation fidelity, SAR, and pulse duration tradeoffs. In: Proceedings of the 15th Annual Meeting of ISMRM, Berlin, Germany, 2007, p 1699.
86. Brunner DO, Pruessmann KP. Enforcing strict constraints in multiple-channel RF pulse optimization. In: Proceedings of the 15th Annual Meeting of ISMRM, Berlin, Germany, 2007, p 1690.